



저작자표시-비영리-변경금지 2.0 대한민국

이용자는 아래의 조건을 따르는 경우에 한하여 자유롭게

- 이 저작물을 복제, 배포, 전송, 전시, 공연 및 방송할 수 있습니다.

다음과 같은 조건을 따라야 합니다:



저작자표시. 귀하는 원저작자를 표시하여야 합니다.



비영리. 귀하는 이 저작물을 영리 목적으로 이용할 수 없습니다.



변경금지. 귀하는 이 저작물을 개작, 변형 또는 가공할 수 없습니다.

- 귀하는, 이 저작물의 재이용이나 배포의 경우, 이 저작물에 적용된 이용허락조건을 명확하게 나타내어야 합니다.
- 저작권자로부터 별도의 허가를 받으면 이러한 조건들은 적용되지 않습니다.

저작권법에 따른 이용자의 권리는 위의 내용에 의하여 영향을 받지 않습니다.

이것은 [이용허락규약\(Legal Code\)](#)을 이해하기 쉽게 요약한 것입니다.

[Disclaimer](#)

공학박사학위논문

Development of novel metal-ceramic
composites via arc plasma-induced
accelerated reaction

아크플라즈마를 통해 촉진된 반응을 이용한
금속-세라믹 복합재료의 개발

2016년 8월

서울대학교 대학원

재료공학부

이 제 인

아크플라즈마를 통해 촉진된 반응을 이용한
금속-세라믹 복합재료의 개발

Development of novel metal-ceramic composites
via arc plasma-induced accelerated reaction

지도교수: 박 은 수

이 논문을 공학박사 학위논문으로 제출함

2016년 7월

서울대학교 대학원

재료공학부

이 제 인

이제인의 박사학위 논문을 인준함

2016년 7월

위 원 장	황 농 문	(인)
부 위 원 장	박 은 수	(인)
위 원	한 흥 남	(인)
위 원	김 도 향	(인)
위 원	서 진 유	(인)

ABSTRACT

Development of novel metal-ceramic composites via arc plasma-induced accelerated reaction

Je In Lee

Department of Materials Science and Engineering

The Graduate School

Seoul National University

New design or optimization for conventional processing of metal-ceramic composites has been intensively investigated since mechanical and thermal properties of the composites depend on the materials' processing history. With an appropriate combination of matrix and reinforcements, the liquid-state processing has been considered relatively cheap and simple route for the synthesis of metal-ceramic composites. However, the chemical reaction between reinforcements and molten alloys results in the interfacial reaction that degrades the properties of the composites. This has stimulated an interest for the development of in-situ processing routes where reinforcements are spontaneously synthesized during the process. However, the in-situ routes commonly require high temperature and long processing time due to the

thermodynamics and kinetics related to the reaction. Thus, it is necessary to optimize the condition of conventional process or develop novel processing routes for the metal-ceramic composites.

Here, arc plasma processing is introduced to develop a novel fabrication route for the in-situ synthesis of metal-ceramic composites. The high temperature processing is advantageous for the in-situ formation of reinforcing materials, the acceleration of the in-situ reaction and the strong interfacial bonding between the matrix and reinforcements. The aim of this study is to investigate the feasibility of developing novel metal-ceramic composites, the forming mechanism of the fabricated composites and the applicability of the resulting composites synthesized by arc plasma-induced accelerated reaction.

Arc plasma-induced volume nitridation of aluminum was observed during arc melting under argon and nitrogen mixed atmosphere. The nitridation process resulted from the instantaneous chemisorption of nitrogen, enhanced nitrogen diffusion and improved wetting of aluminum nitride (AlN) by arc plasma-induced reaction. The aluminum matrix was explosively nitrided, showing the in-situ formation of particulate composites with volume fraction of 40 vol.% which is the highest values among ever reported in-situ Al-AlN composites formed by using nitrogen gas as a reagent.

Arc plasma-induced liquid phase displacement reaction was carried out by arc melting aluminum with the ceramic powders as sacrificial materials. The

liquid aluminum simultaneously infiltrated and reacted with silicon nitride (Si_3N_4) powder preform, leaving in-situ formed AlN reinforced aluminum matrix composites. The displacement reaction between Al and Si_3N_4 led to the volumetric expansion of nitride phase, which enables us to fabricate aluminum matrix composites with high volume fraction of nitrides. The candidate alloy matrix using the arc plasma processing can be extended from pure metals to multi-component alloys like bulk metallic glasses (BMGs). Using Al-AlN particulate composites as a sacrificial reagent, the zirconium nitride (ZrN) reinforced BMG matrix composites were synthesized by arc melting. The in-situ formation of ZrN resulted in the improvement of mechanical properties, which is advantageous for the structural applications of BMGs.

The newly developed metal-ceramic composites above showed attractive thermal or mechanical properties due to the in-situ formation, uniform dispersion of reinforcements and the strong interfacial bonding. This indicates that the arc plasma processing can be promising routes for the synthesis of novel metal-ceramic composites in various gas-liquid-solid systems.

Keywords: composite, arc melting, in-situ process, nitridation, displacement reaction

Student Number: 2010-20624

Table of Contents

Abstract.....	i
Table of contents.....	iv
List of Tables.....	viii
List of Figures.....	ix

Chapter 1. Introduction

1.1. Metal-ceramic composites	1
1.2. Fabrication of metal-ceramic composites	8
1.2.1. Solid-state processing	8
1.2.1.1. Powder metallurgy	8
1.2.1.2. Diffusion bonding	9
1.2.1.3. Spark plasma sintering	12
1.2.1.4. Mechanical alloying	14
1.2.1.5. High pressure torsion	14
1.2.2. Liquid-state processing	17
1.2.2.1. Pressure infiltration	17
1.2.2.2. Stir casting	18
1.2.2.3. Centrifugal casting	20

1.2.3. In-situ processing	21
1.2.3.1. XD process	21
1.2.3.2. Lanxide process	23
1.2.3.3. Reactive melt penetration process	25
1.2.3.4. Gas bubbling method	27

Chapter 2. Experimental procedures

2.1. Sample preparation	29
2.1.1. Arc melting	29
2.1.2. Rapid quenching	31
2.1.2. Suction casting	31
2.1.3. Powder compaction	31
2.2. Structural characterization	32
2.2.1. X-ray diffraction	32
2.2.2. Preparation of metallographic specimens	32
2.2.3. Optical microscopy	32
2.2.4. Secondary electron microscopy	33
2.2.5. Transmission electron microscopy	33
2.3. Thermal analysis	34
2.3.1. Differential scanning calorimetry	34
2.3.1.1. Specific heat	34
2.3.1.2. Characteristic temperature of metallic glass	36
2.3.2. Thermo-mechanical analyzer	36
2.3.3. Laser flash analysis	38

2.4. Mechanical behavior	40
2.4.1. Uniaxial compression test	40
2.4.2. Three-point bending test	40

Chapter 3. In-situ synthesis of cold-rollable aluminum-aluminum nitride composites via arc plasma-induced accelerated volume nitridation

3.1. Introduction	42
3.2. Results and discussion	44
3.2.1. Microstructures	47
3.2.2. Thermal properties	51
3.2.3. Formation mechanism and kinetics of AlN in APAVN process	55
3.2.3.1. Evaluation of AlN formation mechanism in APAVN process	55
3.2.3.2. Comparison of AlN formation rate between APAVN process and gas bubbling method	62
3.2.3.3. Manipulation of thermal properties via APAVN process	65
3.3. Conclusions	67

Chapter 4. In-situ synthesis of aluminum matrix composites with high volume fraction of nitride ceramics by arc plasma-induced accelerated displacement reaction

4.1. Introduction	68
-------------------------	----

4.2. Results and discussion	72
4.2.1. Microstructures	74
4.2.2. Pressureless infiltration	79
4.2.3. Formation mechanism	81
4.2.4. Thermal properties	84
4.2.5. Mechanical properties	90
4.3. Conclusions	92

Chapter 5. In-situ synthesis of ZrN reinforced bulk metallic glass matrix composites by arc plasma-induced accelerated displacement reaction

5.1. Introduction	93
5.2. Results and discussion	97
5.2.1. Microstructures	99
5.2.2. Mechanical properties	107
5.3. Conclusions	111

Chapter 6. Conclusions

References	116
Abstract (In Korean)	121
Curriculum Vitae	124

LIST OF TABLES

- Table 1.1** Mechanical and thermal properties of pure aluminum, silicon carbide and commercially available metal matrix composites [5, 6].
- Table 4.1** Density, thermal and mechanical properties of pure Al, Al-Si-AlN-(Si₃N₄) composites, AlN and Si₃N₄ ceramics [75, 76].

LIST OF FIGURES

- Figure 1.1** A schematic diagram for a material-property map showing two materials, M_1 and M_2 , and different property combination of P_1 and P_2 [1]. The four possible combinations of properties are marked from A to D. Reprinted from Acta Mater, 51, 19, M.F. Ashby and Y.J.M. Brechet, Designing hybrid materials, 5801, Copyright (2003), with permission from Elsevier.
- Figure 1.2** Various processing routes for the synthesis of metal-ceramic composites with different processing temperature.
- Figure 1.3** Schematic diagram for (a) powder metallurgy: homogeneously blended metal/ceramic powders are hot pressed, and (b) diffusion bonding process in which high temperature and pressure are applied to the degassed capsule.
- Figure 1.4** (a) Spark plasma sintering (SPS) instrument installed in KITECH, (b) schematic diagram of SPS process and mechanism of Joule heating by DC current, (c) appearance of the sintered specimen with a shape of cylinder and (d) SEM micrograph of the sintered composites composed of metallic glass matrix (dark) and tantalum secondary phase (bright).

Figure 1.5 (a) High pressure torsion apparatus installed at NIMS, (b) schematic diagram of high pressure torsion deformation, and microstructure of the HPT deformed Al-Si₃N₄ composites fabricated by the consolidation of Al and Si₃N₄ powders after (c) 10 revolutions (N = 10) and (d) 50 revolutions (N = 50).

Figure 1.6 Schematic diagrams for (a) pressure infiltration and (b) stir casting where the liquid alloys are agitated by mechanical force to minimize settling of the reinforcing particles.

Figure 1.7 Schematic diagrams for XD process. The elements X reacts with Y at the temperature above the melting point of A, and the product Z is *in-situ* formed in the liquid A.

Figure 1.8 Schematic diagrams (a) for the mechanism of directed melt oxidation (DIMOX) of aluminum alloy melt in the oxidizing atmosphere and (b) for the net-shape fabrication of metal-ceramic composites by DIMOX process. Reprinted from J. Mater. Process. Tech, 68, 2, B.S.S. Daniel, V.S.R. Murthy and G.S. Murty, Metal-ceramic composites via in-situ methods, 132, Copyright (1997), with permission from Elsevier.

Figure 1.9 Schematic diagram for reactive melt penetration process. The aluminum melt penetrates the substrate and reacts with SiO₂. The reaction results in the formation of interpenetrating structure of Al and Al₂O₃ due to the volumetric contraction from SiO₂ to Al₂O₃.

- Figure 1.10** Schematic diagrams (a) for gas bubbling method and (b) for the formation mechanism of AlN at the periphery of N₂ bubbles.
- Figure 2.1** (a) Arc discharge machine installed in ESPark Laboratory and (b) schematic diagram of arc melting process utilized for the preparation of master alloys with desired compositions.
- Figure 2.2** Heat flow curves of baseline (empty pan), a reference material (Al₂O₃) and a sample for the estimation of specific heat.
- Figure 2.3** (a) Thermo-mechanical analyzer equipped with an intracooler installed in ESPark Laboratory and (b) a sample fixed on the stage with constant load by quartz rod.
- Figure 2.4** (a) Instruments for laser flash analysis installed in SNU and (b) schematic diagram for the laser flash analysis. The inset shows the sample in the instruments; the injection of laser pulse on the sample results in the emission of signal from the opposite surface.
- Figure 2.5** (a) Universal testing machine installed in ESPark Laboratory and (b) a sample fixed between two tungsten carbide plates with strain extensometer (LVDT).
- Figure 3.1** Schematic diagram showing processing procedure for the fabrication of Al-AlN composite sheet via repeated APAVN and cold rolling process.

- Figure 3.2** (a) Cross-section image of as-melted Al-AlN ingot ($t_N = 60$ sec) and (b) appearances of as-melted Al-AlN ingots with increasing nitridation time without repeating the sequence of APAVN process shown in Figure 3.1.
- Figure 3.3** XRD patterns of the as-rolled Al-AlN composites with different nitridation time ($t_N = 15, 30, 60, 120$ and 180 seconds).
- Figure 3.4** (a) Appearance and (b-d) microstructures of the as-rolled composites with different nitridation time ($t_N = 60, 120$ and 180 seconds).
- Figure 3.5** (a) Optical micrograph, (b) SEM micrograph and (c) high-resolution TEM micrograph with selected area diffraction patterns of the as-rolled Al-40 vol.% AlN composites.
- Figure 3.6** CTE of developed Al-AlN composites compared with that of various reported Al-AlN composites and theoretically predicted values [38-41].
- Figure 3.7** Correlation between TC and ITR in the composites and various ex-situ AMCs (V_p of 2nd phase is marked with number) [38-40, 47, 48]. Note that the in-situ AMCs with AlN nanoparticles showed invalid ITR due to their large oxygen contents and poor interface stability [38].
- Figure 3.8** Schematic diagram showing AlN formation mechanism in APAVN process.

- Figure 3.9** (a) Potential energy curves for dissociative adsorption of N_2 molecule and (b) schematic diagrams for a gas surface adsorption model [36].
- Figure 3.10** (a) Schematic diagram showing two representative AlN morphologies formed in as-melted Al-AlN ingot via APAVN process. SEM images of (b) plate-shaped AlN with rods (upper part of ingot) and (c) agglomeration of AlN particles (bottom part of ingot) after nitridation time of 60 seconds in APAVN process.
- Figure 3.11** (a) A TEM image of AlN agglomerates and (b) principle of electrowetting without and with external voltage applied. The contact angle decreases or increases as charge density at dielectric changes [57]. Reprinted from J. Appl. Phys., 92, 7, H.Moon, S.K. Cho, R.L. Garrel and C.J. Kim, Low voltage electrowetting-on-dielectric, 4080, Copyright (2002), with permission from AIP Publishing.
- Figure 3.12** Diffusion profiles of N in Al melt for APAVN process compared with those for gas bubbling method [36].
- Figure 3.13** Correlation between specific TC and CTE of the Al-AlN composites fabricated via APAVN process in relation to various metals, ceramics and AMCs [38-40, 47, 48].

- Figure 4.1** (a) The standard free energies of the nitride ceramics as a function of temperature [62] and (b) contact angle between molten alloy and Si_3N_4 substrate [63-66].
- Figure 4.2** Schematic diagram showing processing procedure for the fabrication of Al-Si-AlN-(Si_3N_4) composites by APADR process.
- Figure 4.3** XRD patterns of the Al-Si-AlN-(Si_3N_4) composites fabricated by APADR process.
- Figure 4.4** (a) OM micrograph and (b) SEM micrograph of the composite A55.
- Figure 4.5** (a) OM micrograph and (b) SEM micrograph of the composite AS73.
- Figure 4.6** Temperature dependence of infiltration pressure of Al melt into the Si_3N_4 preform S45 and S65.
- Figure 4.7** Schematic diagram showing the morphologies of in-situ formed AlN and residual Si_3N_4 phase in Al matrix during APADR process.
- Figure 4.8** (a) Thermal expansion behavior and (b) CTE of the developed Al-Si-AlN-(Si_3N_4) composites compared with that of pure Al and particulate Al-AlN composites.

- Figure 4.9** CTE of the developed Al-Si-AlN-(Si₃N₄) composites compared with that of various reported Al-AlN composites and theoretically predicted values [38-41].
- Figure 4.10** Correlation between thermal conductivity and CTE of the present Al-Si-AlN-(Si₃N₄) composites compared with various in-situ Al-AlN composites [38, 74].
- Figure 5.1** The standard free energies of the nitride ceramics as a function of temperature [62], which shows that ZrN is thermodynamically more stable than AlN at the whole temperature range.
- Figure 5.2** Schematic diagram showing processing procedure for the fabrication of Zr BMG/ZrN composites via APADR process.
- Figure 5.3** XRD patterns of the suction cast Zr BMG/ZrN composites with different diameter from 1 mm to 5 mm.
- Figure 5.4** DSC curves of the as-spun monolithic BMG and Zr BMG/ZrN composites with a table showing glass transition temperature (T_g), crystallization onset temperature (T_x) and enthalpy of crystallization (ΔH_{crys}).
- Figure 5.5** A cross-section image of suction-cast Zr BMG/ZrN composites with a diameter of 2 mm.
- Figure 5.6** SEM micrograph of suction-cast Zr BMG/ZrN composites with a diameter of 2 mm.

- Figure 5.7** High-resolution TEM micrograph of suction-cast Zr BMG/ZrN composites with selected area diffraction patterns of BMG matrix and in-situ formed ZrN particulates.
- Figure 5.8** Compressive stress-strain curves of the suction-cast monolithic Zr BMG and Zr BMG/ZrN composites with diameter of 1 mm. The inset shows modulus, yield strength, fracture strength and plastic strain of the specimens.
- Figure 5.9** Fracture morphologies of suction-cast Zr BMG/ZrN rods with diameter of 1 mm.
- Figure 6.1** Processing routes for synthesis of composite materials with respect to processing temperature, and advantages of the arc plasma processing route for the fabrication of novel metal-ceramic composites.

CHAPTER 1

Introduction

1.1. Metal-ceramic composites

As modern technologies require new materials with unusual combinations of properties that exceed the capacity of conventional materials, a wide range of material-property combinations have been investigated by the development of multi-phase materials. This situation has stimulated an interest for the research of composite materials by mixing at least two distinct phases or introducing novel processing methods to combine dissimilar materials. **Figure 1.1** shows an example of material-property map where two materials, M_1 and M_2 , have different property combinations of P_1 and P_2 [1]. The parts of the map inaccessible by the single materials can be achieved by combining M_1 and M_2 , and **Figure 1.1** shows four different cases from A to D; the latter is not desirable. The best combination of two properties is achieved in scenario A that is the ideal case. The scenario B is the rule of mixture that can be expected by any material scientists as two materials are initially combined. The scenario C is the typical cases we can face, which makes us to live with a compromise. Although the property gains in B and C are less satisfactory, they can still be useful for applications.

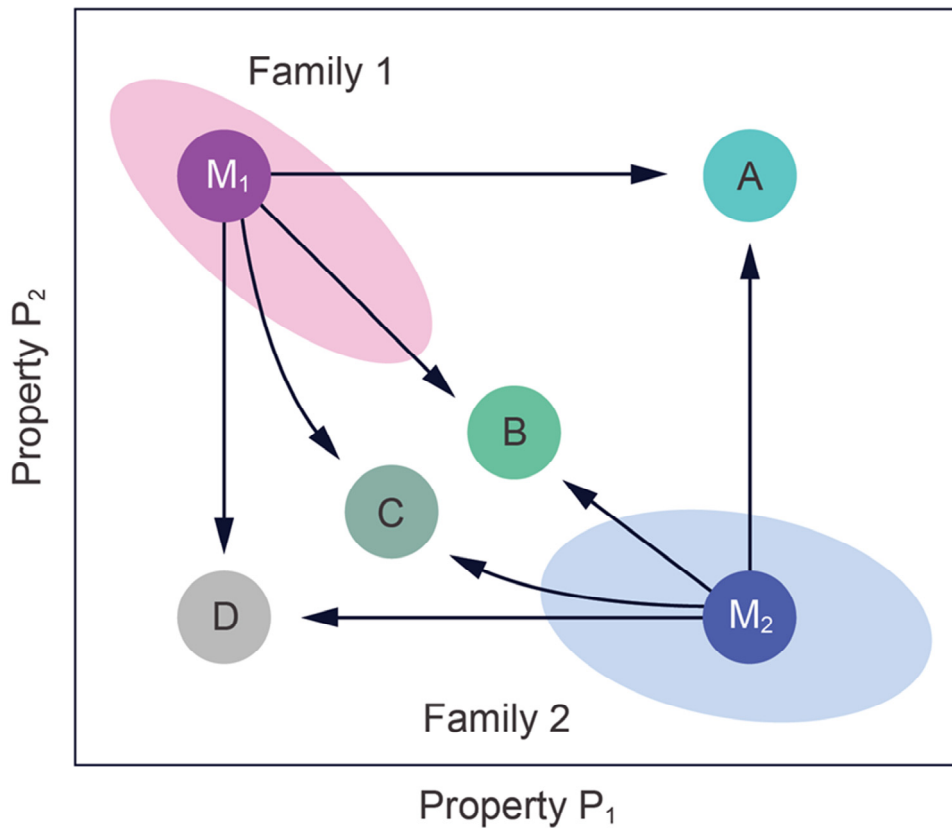


Figure 1.1 A schematic diagram for a material-property map showing two materials, M_1 and M_2 , and different property combination of P_1 and P_2 [1]. The four possible combinations of properties are marked from A to D. Reprinted from Acta Mater, 51, 19, M.F. Ashby and Y.J.M. Brechet, Designing hybrid materials, 5801, Copyright (2003), with permission from Elsevier.

Metal-ceramic composites consist of metal matrix and ceramic reinforcements in general, showing higher stiffness, strength, conductivity and service temperatures compared to the natural composites (e.g. bone, teeth and nacre) or polymer matrix composites that can exhibit thermal instability and degraded mechanical properties at elevated temperature [2, 3]. The metal-ceramic composites show various advantages with respect to unreinforced metals such as weight savings due to the combination of light-weight metals and ceramics, dimensional stability due to the inclusion of rigid reinforcements and high-temperature mechanical properties [4]. The improvement of physical properties in aluminum matrix composites is compared with unreinforced aluminum alloys in **Table 1.1** [5, 6]. In considering aluminum matrix composites for the industrial applications, the properties of particular interest are stiffness and strength as well as density. The improvement in Young's modulus of 6061 Al alloy/20 vol.% SiC composites is less than the modulus value estimated by rule of mixture between aluminum and SiC, but it is still be useful since the composites showed 50 % increase in the modulus comparing with unreinforced aluminum. Thermal properties of a composite are also of interest to the industrial applications since the improved dimensional stability of A356 alloy/60 vol.% SiC composites is beneficial for thermal management of high-power electronic devices. It is commonly considered that the addition of rigid reinforcements such as SiC, B₄C or Al₂O₃ in unreinforced metals always results in the increase of stiffness and strength at the expense of ductility. However, it was reported that the aluminum matrix composites with volume fraction of ceramic particles up to 50 vol.% can be ductile and tough by high stress triaxiality of the reinforcements and ductile nature of matrix failure [7]. Moreover, bulk metallic glasses, which exhibit large elastic limit and higher strength but low ductility compared to crystalline metals, reinforced with

the secondary crystalline phase showed the increase in ductility comparing with the monolithic metallic glasses due to the formation of multiple shear bands and preventing the propagation of shear bands under deformation [8, 9]. Thus, the design and development of novel metal-ceramic composites can draw a new combination of properties that was inaccessible by combining the conventional materials with the conventional process.

Table 1.1 Mechanical and thermal properties of pure aluminum, silicon carbide and commercially available metal matrix composites [5, 6].

	Density (g/cm ³)	Modulus (GPa)	Tensile strength (MPa)	Thermal conductivity (W/mK)	Thermal expansivity (10 ⁻⁶ /K)
Pure Al	2.70	70	50	230	23.6
SiC	3.10	410	-	200	4.0
6061 Al alloy	2.68	69	310	167	23.6
6061/20vol.% SiC	2.78	105	500	-	-
A356 alloy	2.67	76	280	151	21.4
A356/60vol.% SiC	3.0	290	-	180	7.8

There have been considerable efforts on the development of novel metal-ceramic composites for their industrial or extreme environmental applications. **Figure 1.2** shows the various processing routes for synthesis of metal-ceramic composites. In the solid-state processing, the powders of metals and reinforcements are utilized to fabricate metal-ceramic composites. Due to the strong affinity for oxygen, the metal powders such as aluminum, magnesium or titanium should be carefully treated during the whole process, which raises the raw material and processing cost. In the liquid-state processing, reinforcing materials as a powder or fiber form are immersed in molten alloys. The liquid alloy is stirred by mechanically or inductively to achieve homogeneous distribution of the reinforcements, but the alloy composition, temperature and processing time should be carefully controlled due to the high reactivity between the melt and reinforcements. The interaction results in the formation of interfacial compound layer, which degrades mechanical or thermal properties of the resulting composites in general. In the in-situ processing, reinforcing materials, which is thermodynamically stable ceramic phase, are spontaneously synthesized in molten alloys during the process. This has stimulated an interest for the research of developing in-situ process since the manufacturing cost of metal-ceramic composites is dominated by raw materials cost that is about 63 % of the total cost [10]. However, based on the thermodynamics and kinetics, the in-situ processes require high temperature and long processing time, which is uneconomical to industrial applications. Thus, it is necessary to develop a novel processing routes to overcome the problems and open the possibility for the various applications. In this study, a wide range of processing routes is surveyed and a novel processing, arc plasma-induced accelerated reaction, is proposed. The various resulting composites formed by arc plasma processing are introduced and their properties are systematically investigated.

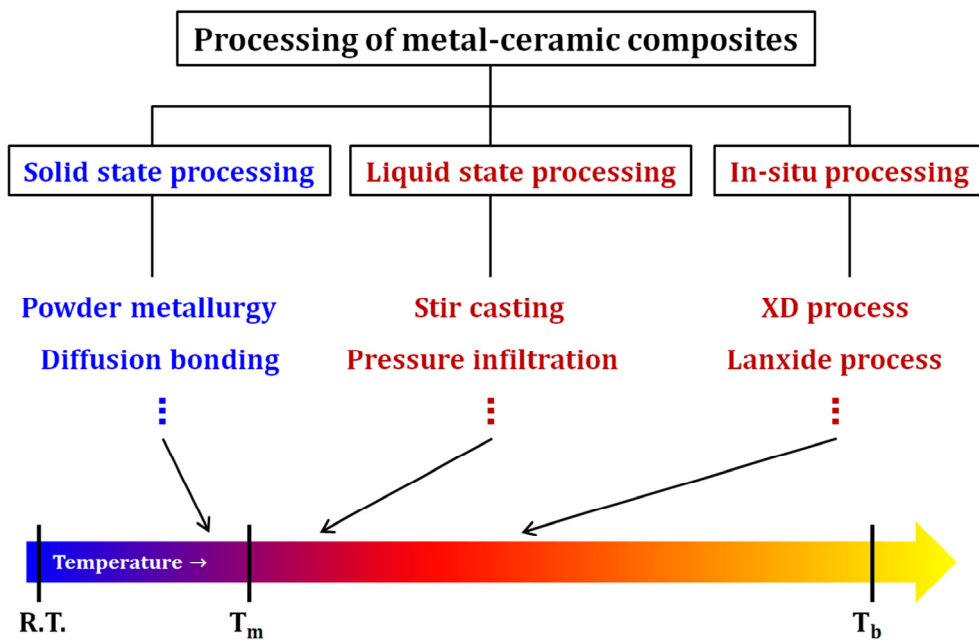


Figure 1.2 Various processing routes for the synthesis of metal-ceramic composites with different processing temperature.

1.2. Fabrication of metal-ceramic composites

The processing routes for the metal-ceramic composites are categorized as solid-state, liquid-state and in-situ processing which were divided by the state of metal matrix during the process. Procedure, advantages and disadvantages of the process will be discussed in detail.

1.2.1. Solid-state processing

In the solid-state processing, a form of powder or foil of metals and reinforcements is chosen as the starting materials. In general, particles or fibers of reinforcements are commonly blended with metal powders and the mixture is hot-pressed, followed by sintering to fabricate a composite. It should be noted that the wettability between the liquid metal and ceramic particles is less important since the matrix and reinforcements are mixed in the solid states [11].

1.2.1.1. Powder metallurgy

Powder metallurgy refers to the process where metal and ceramic powder are mixed, pressed and sintered to fabricate particulate or whisker-reinforced metal-ceramic composites [**Figure 1.3(a)**] [12]. Since as-received metal and ceramic powders are easily aggregated, it is important to break the agglomerations so that the matrix and reinforcing powders can be blended homogeneously. The powder mixtures are prepared by dry method or wet method where a volatile solvent with low surface tension such as ethanol or acetone was mixed with the powders and agitated to achieve uniform distribution of reinforcements. The powder mixtures are compacted by hand-pressing or cold isostatic pressing to prepare what is called a green body with a shape of disk or rectangular. The green body is dried in oven or degassed in vacuum to remove any moisture from the surface of the particles. Degassing and hot pressing

in an inert atmosphere may be necessary if the removal of surface oxide is required since the presence of the oxide skin prevents the bonding between metal and ceramic powder. The hot pressed metal-ceramic composite can be further deformed by secondary processing such as rolling or extrusion to manufacture plate or bar-shaped products. It should be noted that the size ratio between metal and ceramic powders is very important to attain a uniform distribution of reinforcements in the metal matrix. With the larger metal powder in size, the ceramic powders can be packed in the interspacing of the larger metal particles, leading to clustered microstructure. Thus, the metal and ceramic powders with comparable particle size should be utilized to produce the composites with uniform distribution of reinforcements [2].

1.2.1.2. Diffusion bonding

Diffusion bonding is one of common solid-state processing developed for the fabrication of fiber-reinforced composites [**Figure 1.3(b)**]. The main advantages of the process are that a variety of metal matrix can be employed and orientation and volume fraction of fibers can be easily controlled [2]. In this process, fiber arrays are placed on a metal sheet and another metal sheet is stacked, which can be repeated until the required thickness of the fiber/metal stack is achieved. While the stack is degassed, hot-pressed and sintered in vacuum under high pressure, interdiffusion of elements between the clean metal surfaces occurs, leading to diffusion bonding and consolidation. In another example, fiber arrays can be coated with matrix by spraying molten metal to bind the fibers together. The composite sheets are then stacked, and inserted into a container to degas, hot-press and sinter them to fabricate composites. As the interspacing and fraction of fibers is controlled, high volume fraction of fibers up to 80 vol.% can be attained in metal matrix. The disadvantages of the process are

that long processing time, high temperature and pressure are required for diffusion bonding of metal layer. In case of the spraying, fiber arrays may react with or be damaged by molten metals [3], which degrades the mechanical properties of the composites. Orientation and distribution of fibers are also important since localized stress concentration can be arisen at the agglomeration of fibers.

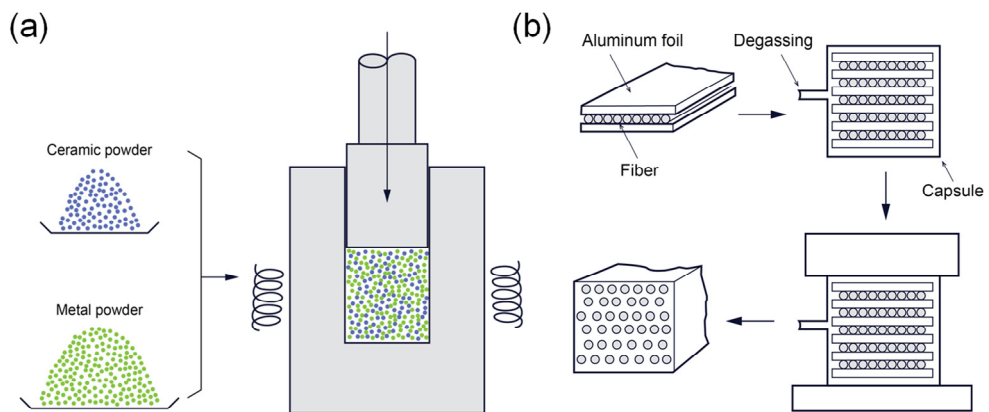


Figure 1.3 Schematic diagram for (a) powder metallurgy: homogeneously blended metal/ceramic powders are hot pressed, and (b) diffusion bonding process in which high temperature and pressure are applied to the degassed capsule.

1.2.1.3. Spark plasma sintering

Spark plasma sintering (SPS) is a high-speed powder consolidation process since the sintering step is finished within a few minutes. In SPS, a pulsed DC current directly passes through the graphite crucible and conductive powder compacts, which results in Joule heating [**Figure 1.4(a) and (b)**]. In contrast to the conventional hot pressing where the heat is supplied by external heating, SPS shows that the heat is generated internally between the powders by DC current, leading to very short sintering time, approximately 5–20 minutes, and fast heating and cooling rate up to 1000 K/min. The spark discharge and Joule heating results in the densification of the compacts at lower temperature compared to conventional hot pressing process, the good bonding of reinforcements with matrix and the decrease in interfacial thermal resistance between them. Recently, the metallic glass powder and its mixture with brass or Ta powder were successfully consolidated at its super-cooled liquid region ($T_g/T_l \sim 0.6$) [13]. The resulting composites with a shape of cylinder exhibited theoretical density of about 100 % [**Figure 1.4 (c)**] and retained amorphous structure without any crystallization, which is promising for the fabrication of the novel composites with high strength and ductility [**Figure 1.4 (d)**].

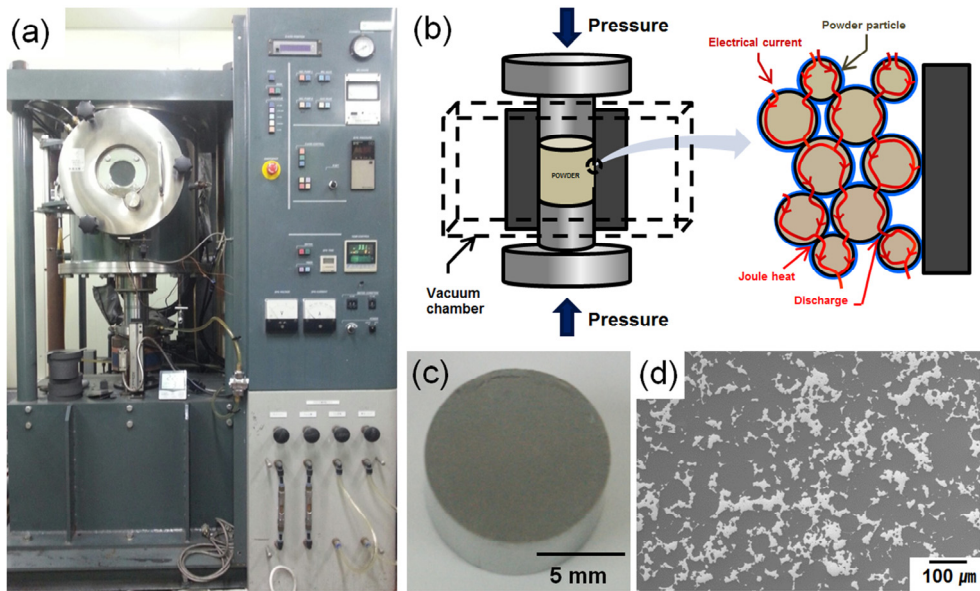


Figure 1.4 (a) Spark plasma sintering (SPS) instrument installed in KITECH, (b) schematic diagram of SPS process and mechanism of Joule heating by DC current, (c) appearance of the sintered specimen with a shape of cylinder and (d) SEM micrograph of the sintered composites composed of metallic glass matrix (dark) and tantalum secondary phase (bright).

1.2.1.4. Mechanical alloying

Mechanical alloying (MA) is a blending process where powder mixtures are mixed in a high-energy ball mill to fabricate composites with fine and uniform distribution of reinforcements [14]. In this process, more than two kinds of powders are mixed and compressed, breaking their oxide skins on the surface. Then, the powder mixtures are welded, fragmented and broken as the milling balls collide to the composite powders, which can be repeated for a long time (more than 10 h). The milled powders are then hot pressed to sinter them and remove internal residual stress. MA is a solid-state processing, but the alloys with atomic scale homogeneity or non-equilibrium state can be obtained such as supersaturated solid solution or amorphous alloys which cannot be produced by the casting of a liquid metal. MA process was originally developed for the fabrication of oxide-dispersion strengthened superalloys, but this process is widely used for the research of metastable crystalline alloys or nano-structured composites.

1.2.1.5. High pressure torsion

High pressure torsion (HPT) is one of the severe plastic deformation process involving high compressive pressure with torsional straining [15]. The disk-shaped sample located between two massive anvils is compressed above 1 GPa [**Figure 1.5(a) and (b)**], subjected to a torsional strain as follows

$$\gamma = \frac{2\pi Nr}{h} \quad (1.1)$$

where N is the number of revolutions, r is distance from the center and h is the thickness of the sample. Grain refinement or microstructural fragmentation are anticipated when the bulk materials are severely deformed by HPT [16]. However, the HPT deformation can be applied for not only bulk samples but also powder mixtures

to consolidate the powders and produce densely packed metal-ceramic composites at room temperature [17]. **Figure 1.5(c) and (d)** show that the Al-Si₃N₄ composites prepared by HPT deformation of Al and Si₃N₄ powders (N = 10 and 50) are fully consolidated without sintering at elevated temperature and the reinforcing particles are uniformly dispersed with increasing shear strain, which is promising for manufacturing metal-ceramic or metal-carbon composites where the interfacial reaction between molten metal and reinforcements should be avoided.

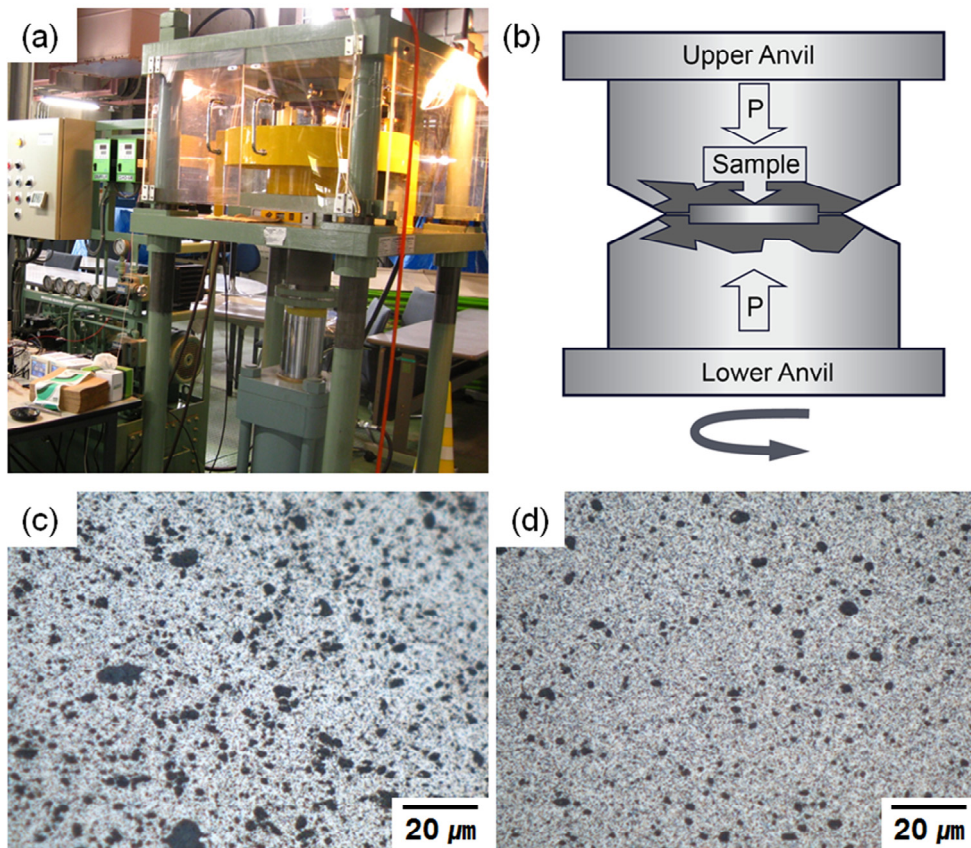


Figure 1.5 (a) High pressure torsion apparatus installed at NIMS, (b) schematic diagram of high pressure torsion deformation, and microstructure of the HPT deformed Al-Si₃N₄ composites fabricated by the consolidation of Al and Si₃N₄ powders after (c) 10 revolutions (N = 10) and (d) 50 revolutions (N = 50).

1.2.2. Liquid-state processing

In the liquid-state processing, ceramic reinforcements are poured into liquid metal. There are two general ways to achieve complete wetting of the particles by melt: by means of chemical and mechanical treatment. Chemical processes include application of coatings to the surface of the reinforcements, and mechanical processes include applications of stirring or external pressure to improve wetting between reinforcements and molten metal. The addition of certain elements such as Ca, Li or Mg to molten alloys has also been found to improve wetting. During the stirring and casting, inert gas atmosphere is preferred to prevent the oxidation melt and the inclusion of surface oxide into the melt [11].

1.2.2.1. Pressure infiltration

In the pressure infiltration process, molten alloys are forced by externally applied pressure to infiltrate a preform [**Figure 1.6(a)**]. The pressure (normally 10-100 MPa for Al alloy) can be applied by means of a ram or gas pressure to infiltrate the pre-heated preform. For infiltration of the preform, the addition of alloying elements like Mg or Si can be effective to reduce surface tension and to improve wettability of the molten alloys. The pressure infiltration process can be used to obtain metal-ceramic composites with volume fraction of reinforcements more than 40 %, which is not achievable in conventional casting technique [18]. Recently, fabrication of high volume fraction composites up to 85 vol.% has been reported by preparing preforms as bimodal powder mixtures or sintered ceramic sponge with open cell structure [19-21]. The principal advantages of the pressure infiltration process comparing with conventional casting are net-shape forming, reduced porosity or shrinkage and minimization of forming interfacial compound due to the shorter processing time.

1.2.2.2. Stir casting

Stir casting process utilize the conventional casting technique to produce Al or Mg alloys [22]. Particulate reinforcements are poured into molten alloys and stirred to improve the wettability of ceramic particles by the melt and obtain uniform distribution of the particles [**Figure 1.6(b)**]. For the homogeneous dispersion, the difference in density between the matrix and reinforcements should be considered unless the particles may sink or float in the melt. It is also important to consider the cooling rate of molten alloys since the dendritic growth of the matrix can result in segregation of reinforcements at the interdendritic area. The additive elements such as Ca, Mg or Si can be introduced to the matrix to improve the wettability and minimize the reactivity between the reinforcements and molten alloys. In case of Al-SiC composites, silicon is typically used to prevent the formation of the undesirable compound, Al_4C_3 [2]. The metal-coated reinforcements can be efficiently dispersed in molten alloys due to the improved wettability; these treatments can reduce the stirring time that affects the formation and growth of the interfacial compounds. Depending on the amount of the particulate reinforcements in the molten alloys, the viscosity of the melt varies as a function of volume fraction [$\eta_c = \eta_m(1+2.5V_p+10.05V_p^2)$, V_p is the volume fraction of the particles] [23], which limits V_p of the composites up to about 30 vol.%. The resulting composite ingots can be treated by secondary mechanical processing to manufacture the form of final products such as billet or sheet.

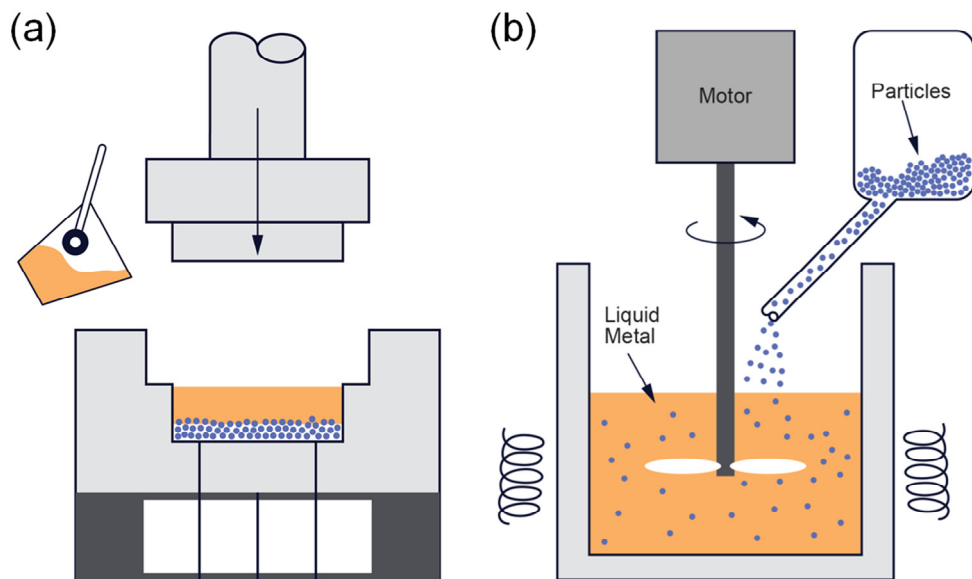


Figure 1.6 Schematic diagrams for (a) pressure infiltration and (b) stir casting where the liquid alloys are agitated by mechanical force to minimize settling of the reinforcing particles.

1.2.2.3. Centrifugal casting

In the centrifugal casting, optimal distribution of the reinforcements can be achieved by inducing a centrifugal force that increases from zero at the rotation center to the periphery of the rim. Gradient structure in volume fraction of reinforcements can be obtained, leaving particle-lean region and particle-rich region that exhibits improved wear resistance. The centrifugally cast composites is suitable for the products with symmetrical shape around a rotational axis such as brake rotor or cylinder liner in engine block.

1.2.3. In-situ processing

The advantage of in situ processes, in general, is that the reaction eliminates problems related to the formation of interfacial compounds, so a relatively clean and well-bonded interface is formed. However, the number of combination of metal and ceramic where the reaction is beneficial, however, is limited, and the relatively fine size distribution of the in-situ formed reinforcements can significantly increase the liquid viscosity [11].

1.2.3.1. XD process

The XD process involves an exothermic reaction between two materials, leading to the in-situ formation of reinforcements in molten alloys (**Figure 1.7**) [24]. The reinforcements such as TiC or TiB₂ can be formed by the reaction ($2B + Ti + Al \rightarrow TiB_2 + Al$, $C + Ti + Al \rightarrow TiC + Al$) where the size, fraction and distribution of the reinforcements as well as matrix composition can be tailored by controlling processing temperature or molar ratio of the reactants. The resulting metal-ceramic composites fabricated by XD process exhibit uniform distribution of the fine (average diameter: < 2 μm) ceramic particles up to 40 vol.% [24] that is advantageous for the increase in modulus, enhanced wear resistance and improved strength at elevated temperature. However, the reactive synthesis of the reinforcements results in the change of molar volume, release of latent heat and formation of byproduct like Al₄C₃, which is undesirable to the mechanical properties of metal-ceramic composites.

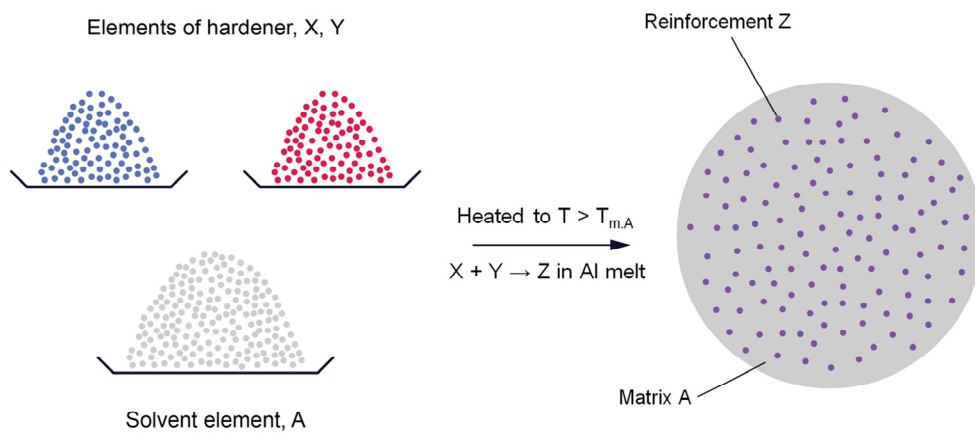


Figure 1.7 Schematic diagrams for XD process. The elements X reacts with Y at the temperature above the melting point of A, and the product Z is *in-situ* formed in the liquid A.

1.2.3.2. Lanxide process

Lanxide process is based on the liquid-gas reaction where molten alloys are treated at flowing gas environment for more than 10 hours, which leads to the formation of interconnected metal-ceramic structure (**Figure 1.8**) [25]. Depending on the gas atmosphere in the chamber, the process can be named as directed melt oxidation (DIMOX) process or directed melt nitridation (PRIMEX) process for the fabrication of oxide or nitride reinforced composites, respectively. In this process with processing temperature above 1273 K, a reaction product with microporous channel such as Al_2O_3 or AlN initially forms on the liquid surface and the product grows outward by continuous wetting the microchannel [**Figure 1.8(a)**]. Thus, the resulting composites exhibit interpenetrating structure where volume fraction of metal and ceramic phase is variable by the control of processing parameters such as alloy composition, atmosphere and processing temperature and time. The direct melt reaction can be applied to infiltrate a preform prepared by compacting particulate or fibrous reinforcements [**Figure 1.8(b)**]. The preform prepared with a shape of the desired product made by growth barrier can be spontaneously infiltrated by the direct melt reactions. However, the application of this process turned out to be uneconomic and undesirable since the process requires high temperature and long processing time, and the number of the combination of the matrix and reinforcements appropriate for the direct melt reaction is limited.

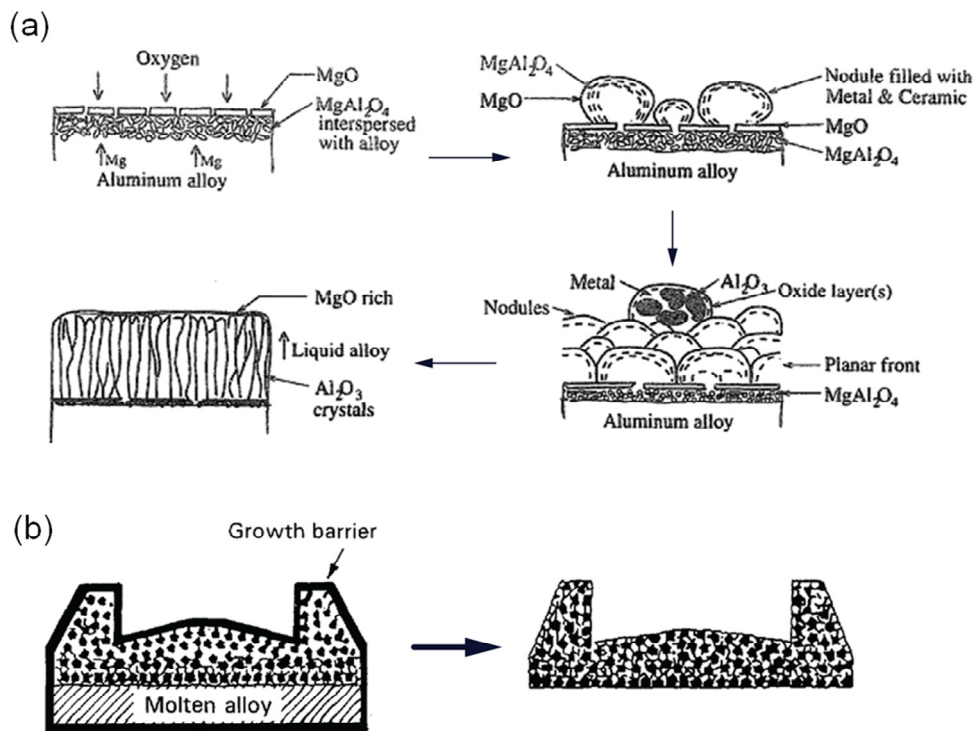


Figure 1.8 Schematic diagrams (a) for the mechanism of directed melt oxidation (DIMOX) of aluminum alloy melt in the oxidizing atmosphere and (b) for the net-shape fabrication of metal-ceramic composites by DIMOX process. Reprinted from J. Mater. Process. Tech, 68, 2, B.S.S. Daniel, V.S.R. Murthy and G.S. Murty, Metal-ceramic composites via in-situ methods, 132, Copyright (1997), with permission from Elsevier.

1.2.3.3. Reactive melt penetration process

Reactive melt penetration of dense ceramic substrate results from a liquid phase displacement reaction that leads to the formation of co-continuous metal-ceramic composites (**Figure 1.9**), especially reported in Al-SiO₂ system [26]. In this process, sacrificial ceramic preform bodies (reactant) are immersed in molten alloys, and the displacement reaction between the melt and ceramic can be carried out at the wide range of temperature. During the reaction, the layer of thermodynamically favorable ceramic phase is formed at the surface of the reactant. At a critical thickness of the newly formed layer, the layer is broken and voids are formed due to the volume contraction of the substrate caused by the difference in molar volume between the reactant and product. The voids are then wet by molten alloys, and the melt penetrates and reacts with the unreacted reactant. These reactions continue until the melt reaches the outer surface of the reactant, then the final products are fabricated. The rate of reaction, size and interspacing of ceramic phase increases as reaction temperature increases, which is beneficial for the improvement of physical properties such as fracture toughness or thermal conductivity.

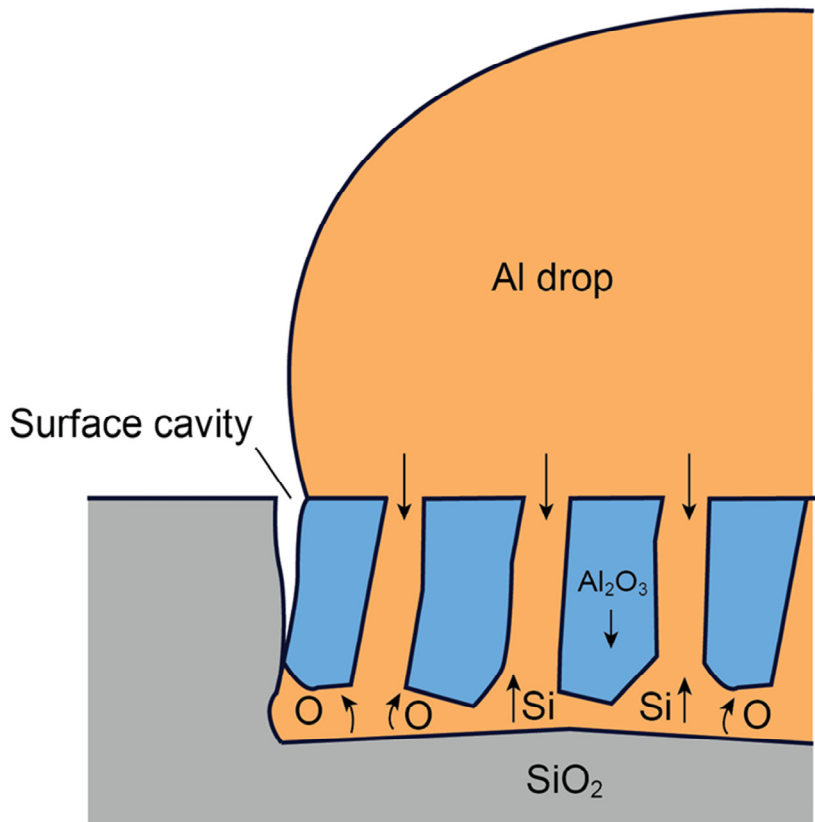


Figure 1.9 Schematic diagram for reactive melt penetration process. The aluminum melt penetrates the substrate and reacts with SiO_2 . The reaction results in the formation of interpenetrating structure of Al and Al_2O_3 due to the volumetric contraction from SiO_2 to Al_2O_3 .

1.2.3.4. Gas bubbling method

Gas bubbling method is one of the in-situ process where reinforcements are synthesized at the interface between molten alloys and bubbles composed of O, N or C bearing gases (**Figure 1.10**) [27]. In the process, the furnace is evacuated and back-filled with argon gas to make inert atmosphere in the chamber. Then, alloy ingots placed in a crucible are heated, especially over 1273 K in Al alloys. The O, N or C-bearing gases, such as CH₄, CO₂, N₂ or NH₃, can be directly injected to the melt through ceramic tube, then the in-situ reaction is carried out for several hours, leaving fine ceramic particles (< 3 μm in size [28]) in the matrix. The additive elements like Mg or Si can be introduced to accelerate the in-situ reaction of the molten alloys since the elements act as a catalysis by forming intermediate phase like Mg₃N₂. CH₄ or NH₃ gas, which is easily dissociated at elevated temperature, can be selected as a bubbling gas into the melt since the dissociated hydrogen reduces partial pressure of oxygen in the bubble and accelerates the in-situ reaction [29, 30]. Although high processing temperature and long duration time are required in gas bubbling method, but the volume fraction of in-situ formed reinforcements is relatively low. The number of combination of alloys and gases where gas bubbling method is feasible is limited since lots of the system with carbon show the formation of undesirable phase such as Al₄C₃ [30].

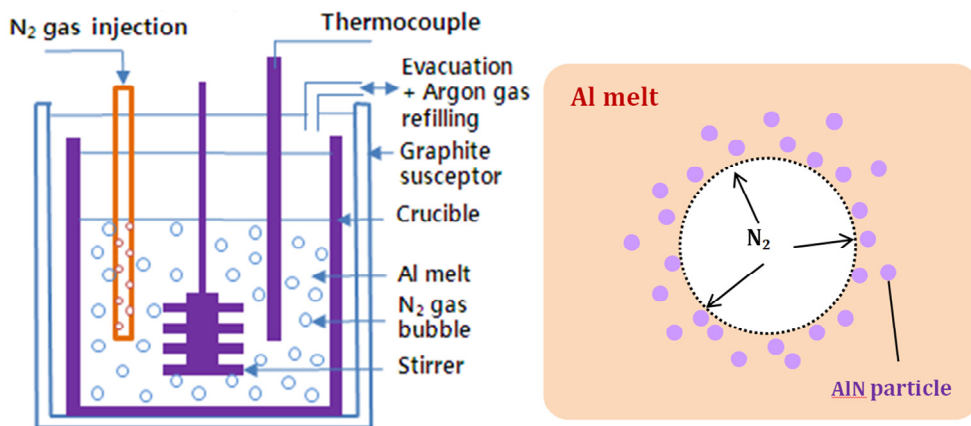


Figure 1.10 Schematic diagrams (a) for gas bubbling method and (b) for the formation mechanism of AlN at the periphery of N₂ bubbles.

CHAPTER 2

Experimental procedures

2.1. Sample preparation

2.1.1. Arc melting

The alloy ingots with desired compositions were prepared by arc melting method with a constant arc voltage of 20 V and arc current of 150 A [**Figure 2.1(a)**]. Pure elements (≥ 99.9 % in purity), placed on water-cooled copper hearth, were melted under a Ti-gettered argon atmosphere with total pressure of 40 kPa (99.999 % purity) [**Figure 2.1(b)**]. The ingots were re-melted five times to ensure compositional homogeneity before casting. When it is necessary to prepare master alloys containing Ag or Mn, the elements were stacked between other constituents to minimize evaporation under arc plasma due to their high vapor pressure.

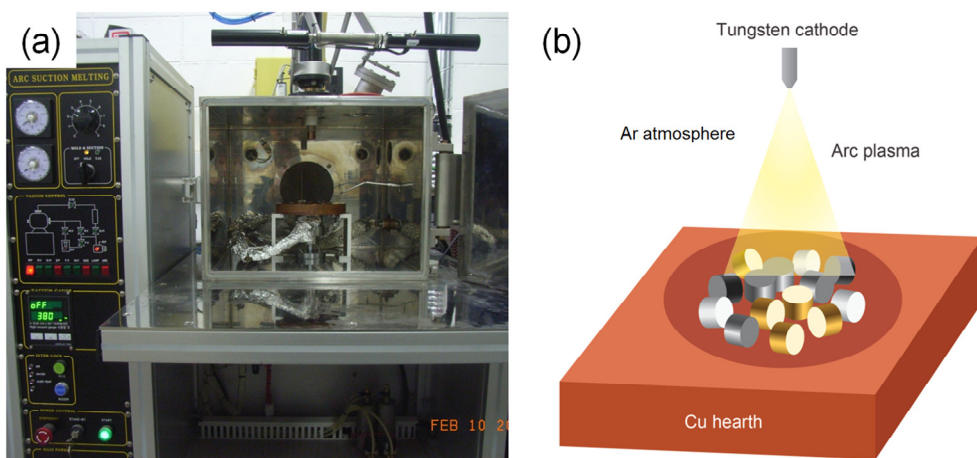


Figure 2.1 (a) Arc discharge machine installed in ESPark Laboratory and (b) schematic diagram of arc melting process utilized for the preparation of master alloys with desired compositions.

2.1.2. Rapid quenching

The arc-melted ingots were crushed into small pieces and inserted in a quartz tube with a small nozzle (less than 1 mm in diameter). The tube is installed in the melt-spinning apparatus and then the chamber was evacuated and back-filled by argon gas with a pressure of 40 kPa. The pieces are inductively re-melted and molten alloys are quenched by the injection of the melt on a rotating copper wheel with linear velocity of 40 m/s. It is worth noting that the melt may react with quartz tube; silicon diffuses out of the quartz tube and dissolves into the melt, which was already described in **Section 1.2.3.3**. Thus, the quenching process should be finished at the moment the pieces of alloys completely melt in the tube.

2.1.3. Suction casting

To obtain alloy/composite samples with rod shape, the alloy ingots, placed on a water-cooled copper mold, were melted by arc plasma and suction-cast into the mold with cylindrical cavities of variable diameter from 1 mm to 12.5 mm and height from 30 mm to 50 mm.

2.1.4. Powder compaction

Ceramic powders were compacted by at room temperature into a disk shape with dimensions of Φ 13 mm \times 2 mm, followed by cold isostatic pressing at a pressure of 200 MPa. The pressed preform was dried in an oven at 423 K for 12 h to remove moisture. For the preparation of preform with high V_p of ceramic particles, bimodal powder mixtures were prepared from the powders with different mean diameter of the particles. The maximum V_p of particles (\sim 70 vol.%) can be achieved when the relatively coarse and fine particles are mixed as the 7:3 ratio in volume [20].

2.2. Structural characterization

2.2.1. X-ray diffraction

Phase constitution and crystal structures were confirmed by X-ray diffraction (XRD, Bruker, New D8 Advance, Germany) using monochromatic Cu K α radiation ($\lambda = 0.15405$ nm) for a 2θ range of 20-80° with a scanning rate of 4 degrees per minute. Samples were ground by using 600-grit SiC paper to prepare flat surface for the diffraction.

2.2.2. Preparation of metallographic specimen

The samples like composite ingots or suction-cast rods were sectioned by high speed saw (Allied, TechCut 5, USA), low speed saw (Allied, TechCut 4, USA) and/or diamond wire saw (Well diamond wires saws, Model 3032, USA) to obtain metallographic samples. The sectioned samples were encapsulated in cold-mount by using low viscosity epoxy resin and hardener (Allied, EpoxySet, USA). The mounted samples were ground on SiC paper (320-800 grit size), polished with diamond suspension (6-1 μm) and finally polished by colloidal silica suspension (0.05 μm) by using grinding/polishing machine (Allied, DualPrep, USA).

2.2.3. Optical microscopy

Optical micrograph was obtained by optical microscope (OM, Nikon, Eclipse LV 150, Japan) with automatically moving stage (Prior, Proscan III, USA) which is advantageous for tiling various images to produce an image with large area. Volume fraction, size and interspacing of composite samples were analyzed by using image analysis software (IMT i-solution, iSolution DT, USA).

2.2.4. Secondary electron microscopy

Secondary electron micrograph was obtained by scanning electron microscope (SEM, Hitachi, SU70, Japan) equipped with energy dispersive X-ray spectroscopy (EDS). To obtain the microstructures, the samples were fixed on the aluminum alloy or brass holder by using electrically conductive adhesives such as silver paste or carbon tape.

2.2.5. Transmission electron microscopy

Transmission electron microscope (TEM, JEOL, JEM 2100F, Japan) was used to obtain high-resolution images of the samples. The thin foil specimens for TEM observation were prepared by Ar ion milling using precision ion polishing system (PIPS, Gatan, Model 691, USA)

2.3. Thermal analysis

2.3.1. Differential scanning calorimetry

2.3.1.1. Specific heat

Thermal response of materials with increasing temperature was characterized by differential scanning calorimetry (DSC, Perkin Elmer, DSC 8500, USA). Specific heat was determined by DSC in the temperature range of 273 K – 600 K under argon gas at a flow rate of 20 mL/min. To obtain accurate results around 273 K, intracooler was utilized to thermally equilibrate the platinum holder under room temperature. Specimens were prepared by slicing alloys/composites with thickness under 0.3 mm to ensure uniform temperature distribution. The weight of samples was precisely measured by using ultra micro electrical balance (Sartorius, SE2, Germany) with a resolution of 0.1 µg. Calculation of specific heat of samples was performed by the equation for multiple curve method as follows (Fig. 2.1);

$$\frac{dQ}{dt} = zY = m \times C_p \times \frac{dT}{dt} \quad (2.1)$$

where Q, t, z, Y, m, C_p, T were amount of heat, time, a coefficient related to instrumental calibration, vertical displacement between specimen curve and baseline at a given temperature (shown in **Figure 2.2**), sample mass, specific heat and temperature, respectively. Assuming that the coefficient, z, is constant regardless of the samples, specific heat of a sample can be estimated using equation (2.1)

$$C_{p,s} = \frac{m_r}{m_s} C_{p,r} \frac{Y_{1,s}}{Y_{1,r}} \quad (2.2)$$

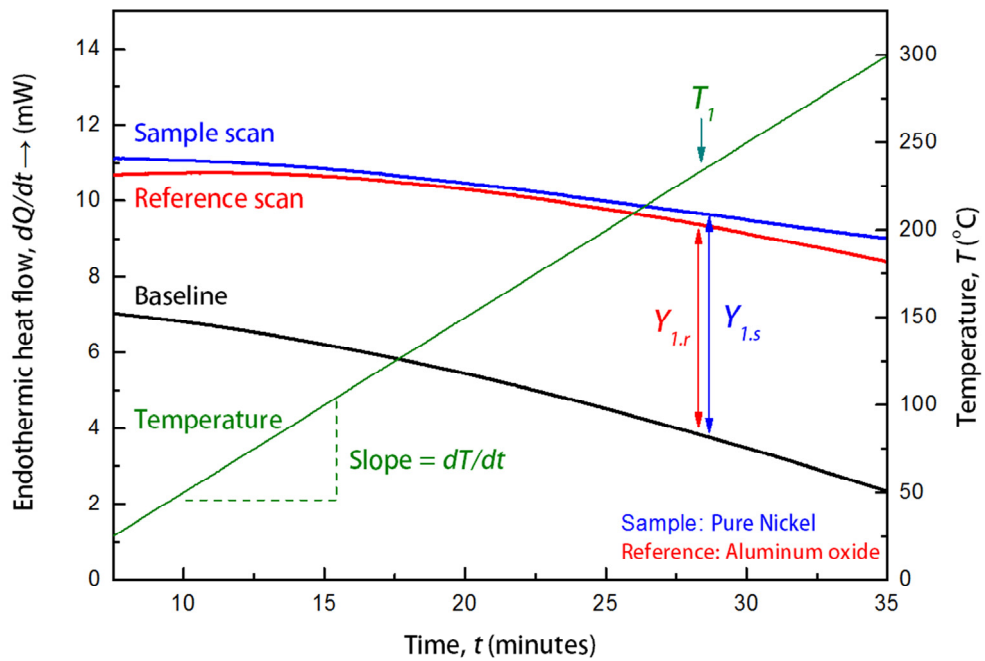


Figure 2.2 Heat flow curves of baseline (empty pan), a reference material (Al_2O_3) and a sample for the estimation of specific heat.

2.3.1.2. Characteristic temperature of metallic glass

Glass transition and crystallization of a metallic glass were identified by DSC apparatus. A disk-shaped specimen sliced from alloy ingots or rapidly quenched ribbon sample was enclosed in aluminum crucible and heated at a heating rate from 5 K/min to 80 K/min. Enthalpy of crystallization was measured by integrating the area of exothermic crystallization peak.

2.3.2. Thermo-mechanical analyzer

Thermal expansion behavior of samples was characterized by using thermo-mechanical analyzer (TMA, TA instruments, Q 400, USA) equipped with intracooler [Figure 2.3(a)]. To ensure uniform temperature distribution of the sample during the experiment, cross-sectional area of the sample was controlled smaller than 3 mm in width or 3 mm in diameter. The sample with flat and parallel ends was placed on stage and pressed by quartz rod with a constant load of 0.1 N [Figure 2.3(b)]. According to ASTM E831, the specimen was heated at a constant heating rate of 5 K/min under argon gas at a flow of 100 mL/min. Coefficient of thermal expansion (CTE) was determined by the dimensional change of the samples as follows;

$$\text{CTE} = \frac{1}{L_0} \frac{(L_T - L_0)}{(T - T_0)} \quad (2.3)$$

where T_0 is room temperature (RT), L_0 is the sample length at RT and L_T is the length of sample at a given temperature. Without special notification, CTE in this thesis refers to the value measured at the temperature range of 300 K – 373 K.

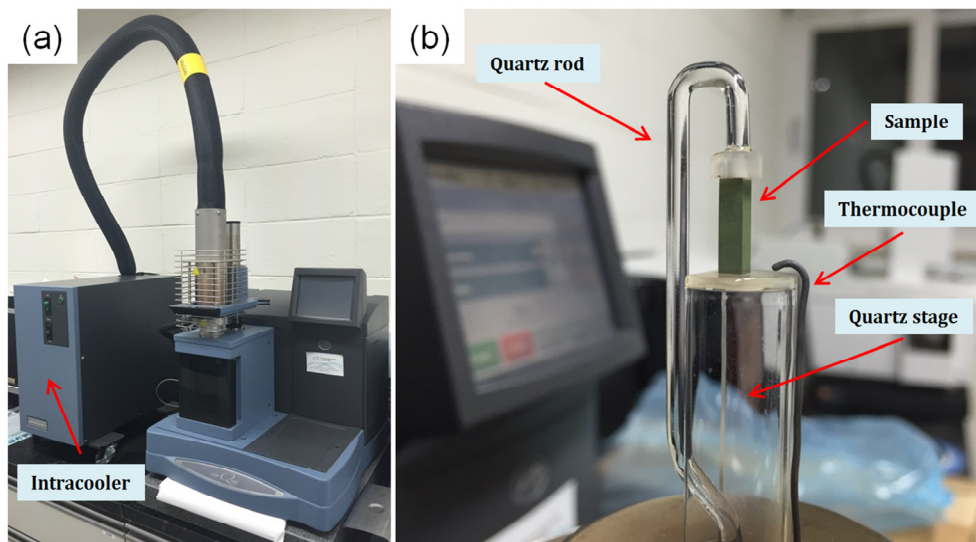


Figure 2.3 (a) Thermo-mechanical analyzer equipped with an intracooler installed in ESPark Laboratory and (b) a sample fixed on the stage with constant load by quartz rod.

2.3.3. Laser flash analysis

Thermal conduction in materials can be evaluated by calculating the product of thermal diffusivity (α), specific heat and density (ρ) as follows;

$$\kappa = \alpha \times C_p \times \rho \quad (2.4)$$

α was measured by laser flash analysis (NETZSCH, LFA 447, Germany) under argon gas at a flow of 100 mL/min [Figure 2.4(a)]. Disk-shaped samples with faces flat and parallel within 0.5 % of their thickness were prepared with diameter range from 6 mm to 12.5 mm. Surface of the samples was scratched by 320-grit SiC paper and then coated by graphite spray to improve the ability of laser absorption. To prevent surface oxidation of the sample during test, the chamber was evacuated and back-filled by argon gas at least three times before the test. α of the sample was obtained by measuring the time ($t_{1/2}$) required for the rear surface temperature rise to reach one half of its maximum value, and then the α can be calculated ($\alpha = 0.1388 \times h^2/t_{1/2}$) [Figure 2.4(b)].

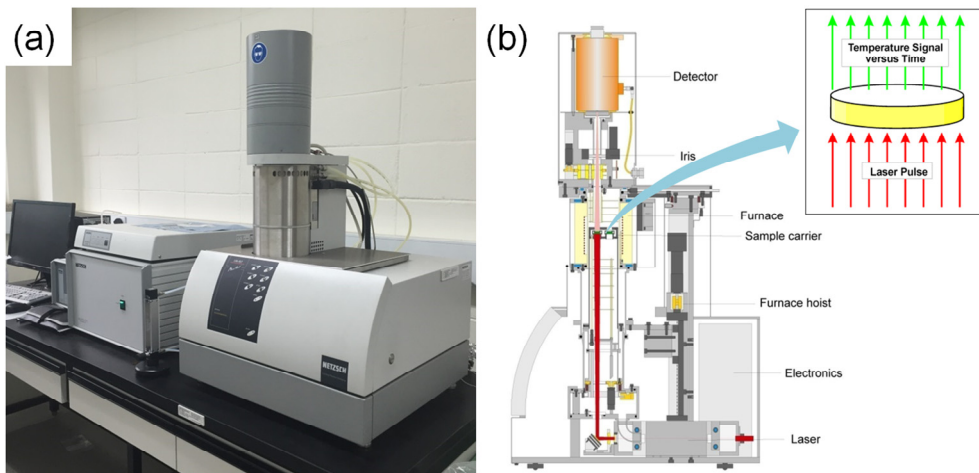


Figure 2.4 (a) Instruments for laser flash analysis installed in SNU and (b) schematic diagram for the laser flash analysis. The inset shows the sample in the instruments; the injection of laser pulse on the sample results in the emission of signal from the opposite surface.

2.4. Mechanical behavior

2.4.1. Uniaxial compression test

Compressive properties of a sample was characterized by universal testing machine (UTM, Instron, Instron 5967, USA) equipped with 30 kN load cell [Figure 2.5(a)]. Cylindrical samples were prepared with faces flat and parallel within 1 % error of their height. According to ASTM E9, the sample was recommended to be machined with the diameter/height ratio as 2:1 for the determination of compressive strength of high-strength materials such as metallic glasses. The sample was fixed between the anvils of UTM with two tungsten carbide plates to prevent permanent deformation of the anvils due to the high strength of metallic glasses. Uniaxial compression test was performed at a constant strain rate of 10^{-4} /sec until the sample fractured. Compressive strain was measured by linear variable differential transformer (LVDT) with resolution of 0.5 μm [Figure 2.5(b)]. Fractography of the sample was taken by observing the pieces of broken sample using SEM.

2.4.1. Three-point bending test

Flexural strength and fracture toughness (K_{IC}) of a sample was measured by UTM (Instron, Instron 5944) equipped with 4 kN load cell. The sample was machined with a thickness of 1.5 - 2.0mm and width of 3.0 - 3.2 mm. Three-point bend tests were performed to obtain stress-strain information with a support span of 10 mm at a displacement rate of 1 $\mu\text{m/s}$. The K_{IC} was measured on single-edge notched bend sample loaded in three-point bending with a span of 10 mm. The notch was first introduced by using a low speed saw and then sharpened by repeatedly sliding a razor blade [31].

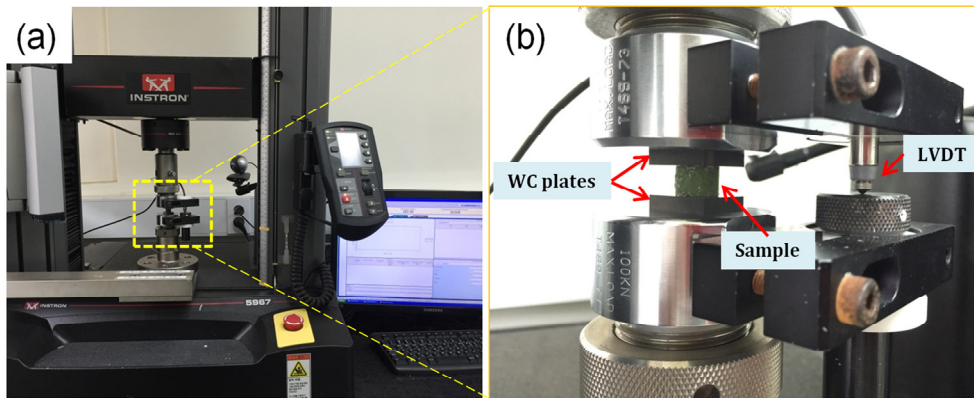


Figure 2.5 (a) Universal testing machine installed in ESPark Laboratory and (b) a sample fixed between two tungsten carbide plates with strain extensometer (LVDT).

CHAPTER 3

In-situ synthesis of cold-rollable aluminum-aluminum nitride composites via arc plasma-induced accelerated volume nitridation

3.1. Introduction

As thermal management industry has focused on finding new materials to improve heat dissipation that affects reliability and performance of the electronic devices, Al matrix composites (AMCs) have attracted considerable interest due to their low density, high thermal conductivity (TC) and low coefficient of thermal expansion (CTE) [32]. However, AMCs manufactured by conventional ex-situ process are economically unfavorable due to expensive reinforcing materials and thermodynamically unstable due to interfacial reaction between matrix and reinforcements [30]. Thus, in-situ fabrication of AMCs with ceramic 2nd phase such as TiC, Al₂O₃ and SiC has been investigated for several decades and various processes like self-propagating high temperature synthesis [33], directed melt oxidation [34, 35] or gas bubbling method [27-30, 36, 37] were developed as a feasible process depending on the formation of ceramic 2nd phase.

Recently, aluminum nitride (AlN) has been considered as an attractive 2nd phase in AMCs due to excellent TC and low CTE [27, 38-41]. Thus, a few scenarios have been proposed to fabricate in-situ AMCs with AlN by nitridation of Al melt by gas-melt reaction [27, 35]. For example, as a directed melt nitridation process [35], molten Al-(Mg, Si) alloys were heated above 1273 K and held for more than 12 hours, which promotes formation of microporous AlN on the liquid surface and outward growth of AlN by continuous wetting of the liquid alloy through the microchannel, resulting in the formation of AMCs with interconnected network of the alloy and AlN. Although this process leads to formation of AMCs with high volume fraction (V_p) of AlN above 50 vol.%, TC of Al matrix abruptly deteriorates with the addition of alloying elements, Mg and Si [42]. And in case of gas bubbling method, nitrogen-bearing gas was injected into Al melt at 1273-1473 K for 6 hours, but V_p of AlN obtained by mainly surface nitridation was less than 10 vol.% [36], which is impractical to be applied for heat sinks. Furthermore, thermal plasma evaporation process utilizes high energy of plasma to synthesize AlN and Al-AlN particles within several minutes [43]. In the process, however, in-situ formed particles were very small in size (50 nm in diameter) and the particles should be sintered with Al powders to produce bulky Al-AlN composites [38]. In sum, although various approaches for fabricating in-situ AMCs with AlN by nitridation of Al melt have been proposed, we are still far away from continuous production of in-situ Al-AlN composites with attractive thermal properties through cost-effective processing.

In the present study, we report in-situ formation of Al-AlN composites via arc plasma-induced accelerated volume nitridation (APAVN) of pure Al melt using N₂ gas. In APAVN process, AlN 2nd phase in Al melt was explosively produced by direct reaction between Al melt and dissociated nitrogen and arc plasma-induced ultra-high

temperature. Al-AlN composite sheets were successfully fabricated by cold-rolling the as-cast Al-AlN ingots. The distinctive microstructure and thermal properties of the as-rolled composites were systematically characterized. Indeed, the formation mechanism and formation kinetics of AlN in newly developed APAVN process were carefully discussed.

3.2. Results and discussion

Nitridation of Al was performed by arc melting method with a constant arc voltage of 20 V and arc current of 150 A. **Figure 3.1** illustrates the sequence of APAVN process fabricating Al-AlN composite sheets. Pure Al pieces, placed on water-cooled copper hearth, were melted under Ar-N₂ mixed atmosphere (2:1 ratio, 99.999 % purity, total pressure of 60 kPa), which leads to in-situ formation of AlN in Al melt. Cross-section of the as-melted Al-AlN ingot revealed that the in-situ formed AlN was uniformly dispersed in Al matrix [**Figure 3.2(a)**], but the AlN was shown as thin lines or branch, which will be discussed later. To minimize evaporation of Al and AlN, arc melting was carefully performed for less than 60 seconds at a time. Otherwise, the as-cast Al-AlN ingots become significantly porous and irregular in shape, which was shown in **Figure 3.2(b)** [44]. The button-shaped Al-AlN ingots were cold-rolled with a thickness reduction of 10 % per pass, resulting in fragmentation and dispersion of AlN in Al matrix. To fabricate composites with higher fraction of AlN, the as-rolled composites were cut and re-melted in Ar atmosphere to prepare Al-AlN buttons, and then the buttons were melted again in Ar-N₂ mixed atmosphere for secondary nitridation. The whole process in **Figure 3.1** was repeated up to three times (total nitridation time: 180 seconds).

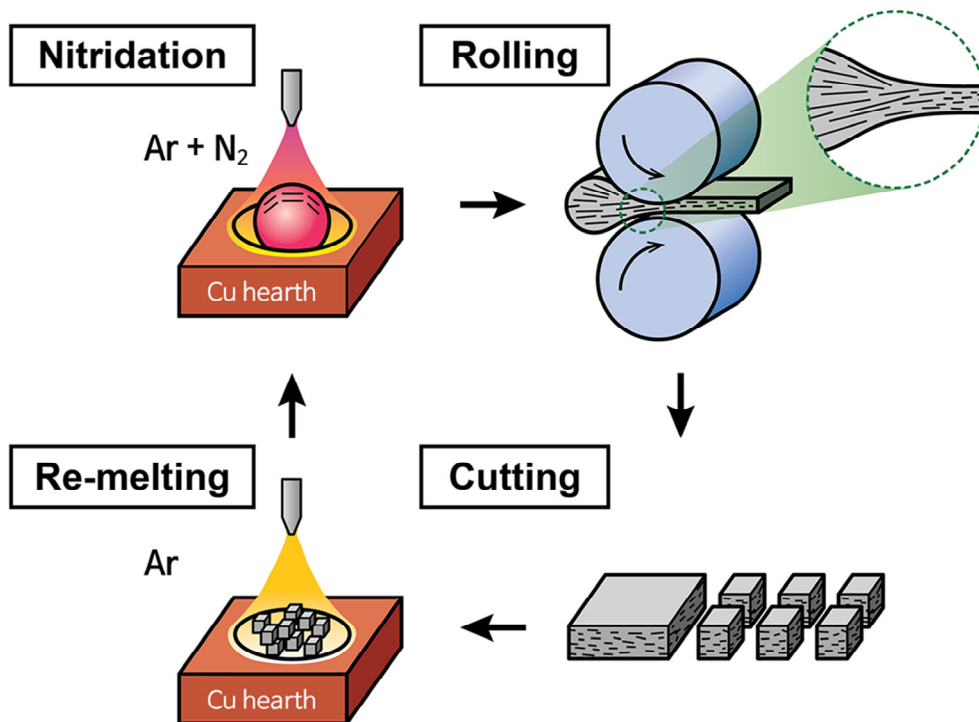


Figure 3.1 Schematic diagram showing processing procedure for the fabrication of Al-AlN composite sheet via repeated APAVN and cold rolling process.

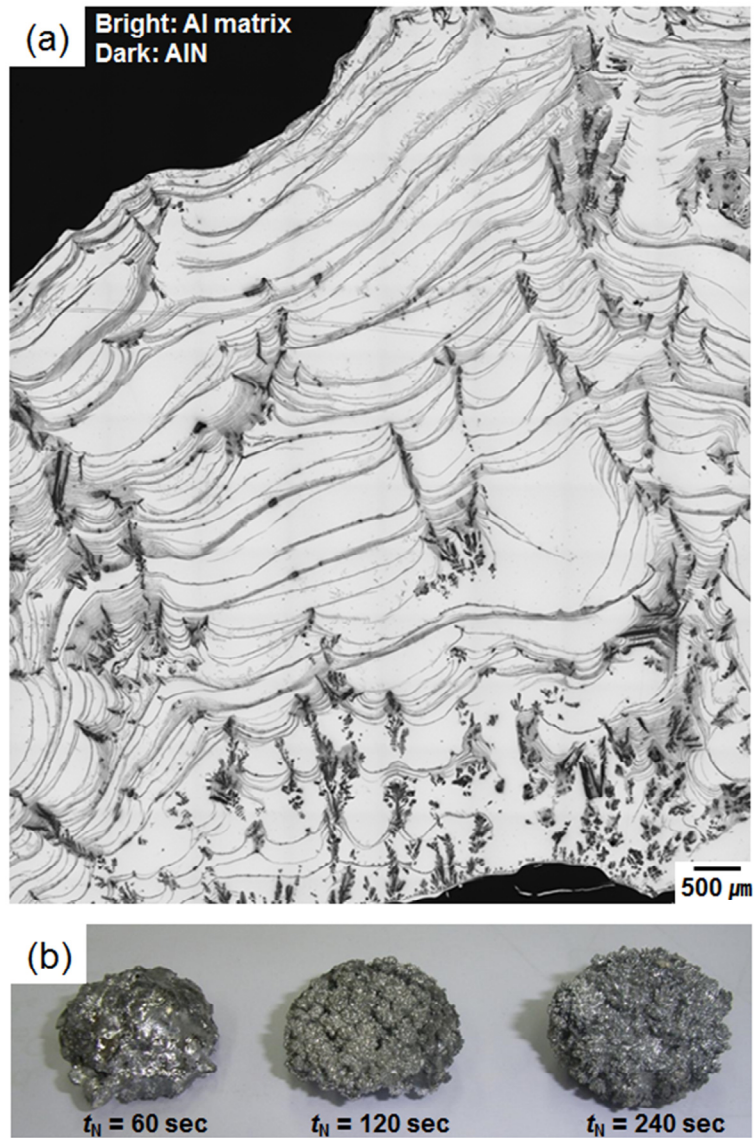


Figure 3.2 (a) Cross-section image of as-melted Al-AIN ingot ($t_N = 60 \text{ sec}$) and (b) appearances of as-melted Al-AIN ingots with increasing nitridation time without repeating the sequence of APAVN process shown in Figure 3.1.

3.2.1. Microstructures

Figure 3.3 shows XRD patterns of as-rolled Al-AlN composites with different nitridation times. V_p of AlN in composites increased as the nitridation time (t_N) increases (**Figure 3.4**), but was saturated around 40 vol.% ($V_p=40[1-\exp(-t_N/40)]$) since the Al melt with large fraction of AlN can be overheated by arc melting due to the insufficient cooling [44], leading to evaporation of Al and decomposition of AlN ($T_{dec}=2627$ K at 60 kPa). The composite ($t_N=180$ sec) contained about 40 vol.% of AlN, which is the highest value among in-situ Al-AlN composites formed by nitridation of pure Al melt using N_2 gas [27, 28, 36, 37]. At the maximum V_p of AlN, the specific weight gain normalized by t_N ($=[\text{weight of in-situ formed AlN}]/[\text{total volume of Al melt} \cdot t_N]$) in APAVN process is 2.94×10^{-1} g/min·cm³, which is about 400 times higher than that in gas bubbling method (6.91×10^{-4} g/min·cm³ [36]).

Figure 3.5(a) shows optical micrograph of as-rolled Al-40 vol.% AlN composites, indicating a typical microstructure of particulate composites with homogeneously dispersed AlN. The average diameter of the AlN particles (d_p) is about 5 μm [**Figure 3.5(b)**]. The particles appeared approximately round-shaped, resulting from surface smoothing of AlN to reduce total free energy during arc melting. **Figure 3.5(c)** shows a high-resolution TEM image of interface between Al matrix and AlN particles with their selected area electron diffraction patterns. The AlN particles were well-bonded to Al matrix without any contaminant or oxide layer since the in-situ formation of AlN by arc melting method prevents surface oxidation and improves wettability between Al melt and AlN. In particular, **Figures 3.5(b) and (c)** reveal that the AlN particles were completely wet by Al melt with arc plasma-induced ultra-high temperature over 2000 K (measured by pyrometer [44] or estimated by Al vapor pressure [45]) despite poor wettability of AlN by Al below 1573 K [46].

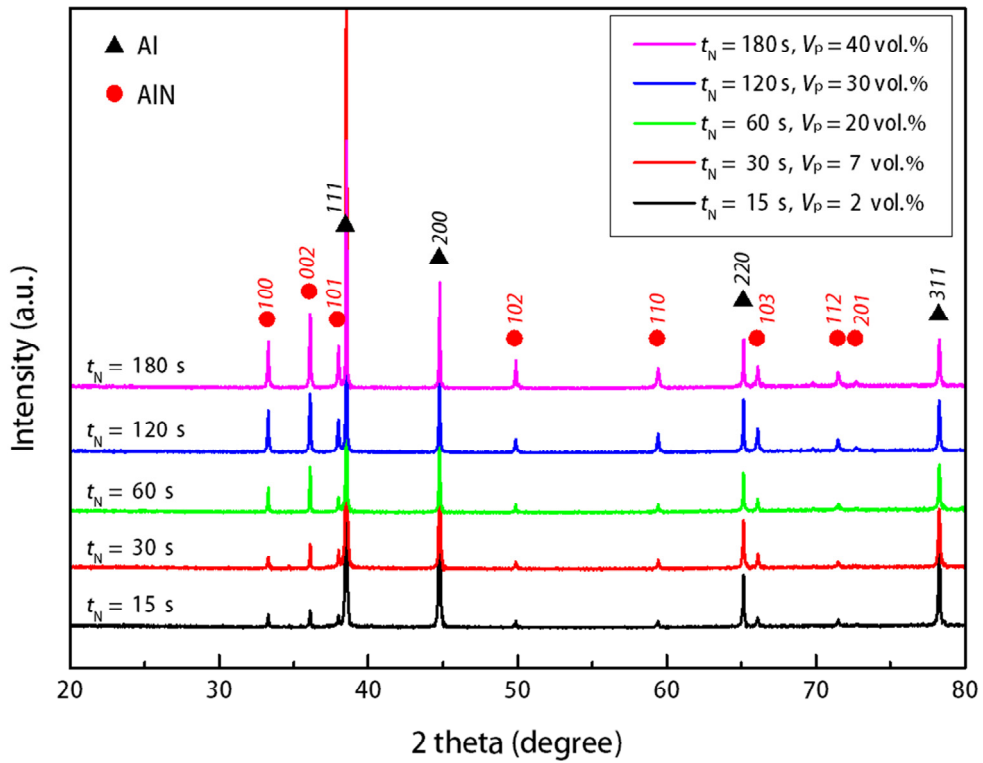


Figure 3.3 XRD patterns of the as-rolled Al-AIN composites with different nitridation time ($t_N = 15, 30, 60, 120$ and 180 seconds).

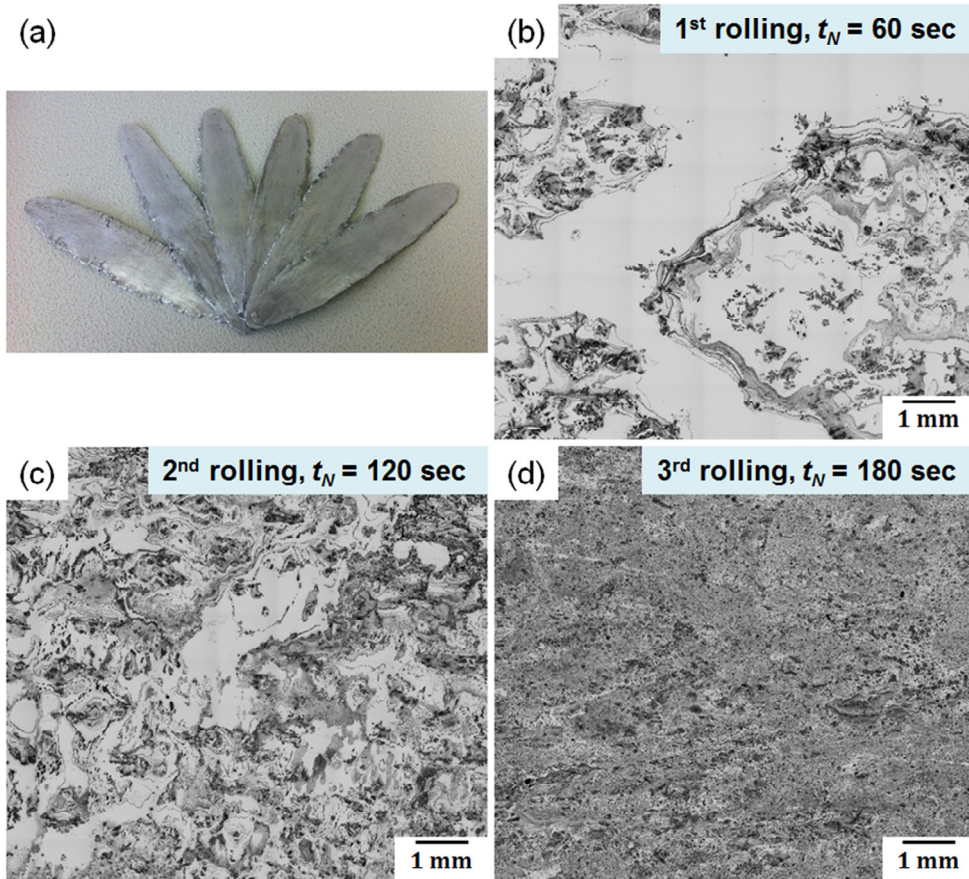


Figure 3.4 (a) Appearance and (b-d) microstructures of the as-rolled composites with different nitridation time ($t_N = 60, 120$ and 180 seconds).

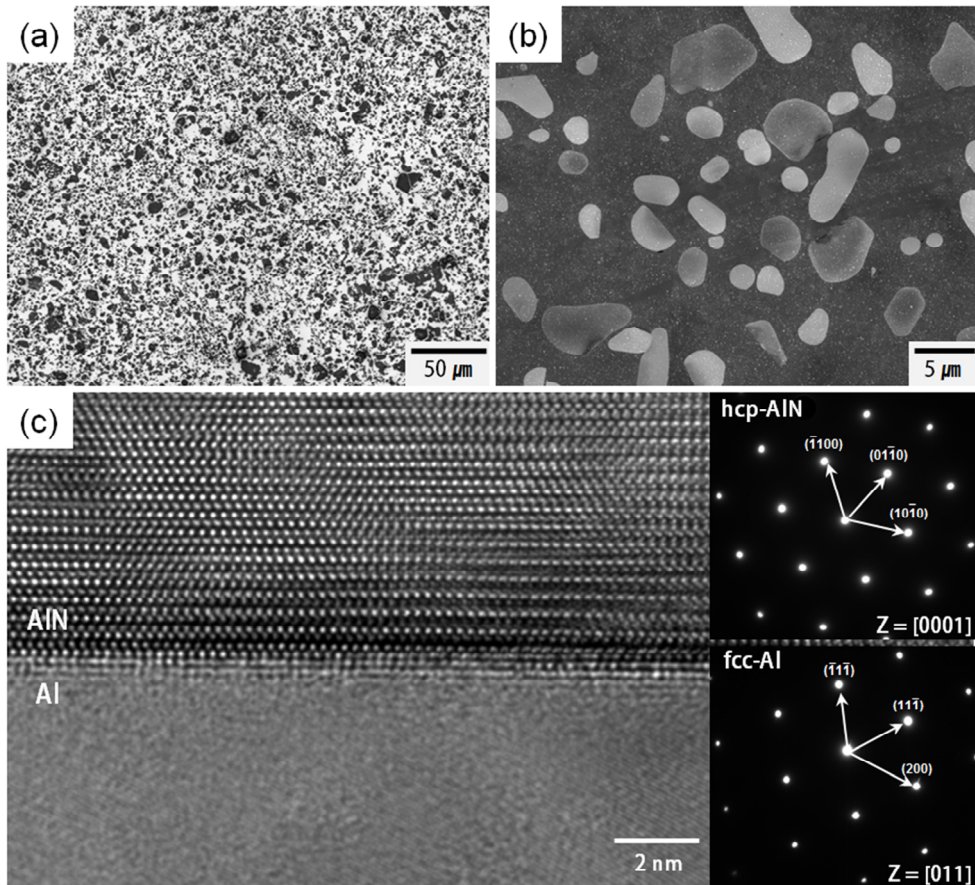


Figure 3.5 (a) Optical micrograph, (b) SEM micrograph and (c) high-resolution TEM micrograph with selected area diffraction patterns of the as-rolled Al-40 vol.% AlN composites.

3.2.2. Thermal properties

Figure 3.6 shows CTE of developed Al-AlN composites compared with that of various reported Al-AlN composites and theoretically predicted values [38-41], indicating that CTE roughly decreases with increasing V_p of AlN ($14.6 \times 10^{-6} \text{ K}^{-1}$ for 40 vol.% AlN). Compared to Turner's model assuming equilibrium of internal stress between particles and matrix [$\alpha_c = (\alpha_m V_m K_m + \alpha_p V_p K_p) / (V_m K_m + V_p K_p)$], CTE of the present composites was well matched with Kerner's model assuming volumetric expansion of a spherical particle wet by matrix [11];

$$\alpha_c = \alpha_m V_m + \alpha_p V_p + V_p V_m (\alpha_p - \alpha_m) \times \frac{B_p - B_m}{V_m B_m + V_p B_p + 3B_p B_m / 4G_m} \quad (3.1)$$

where α , V , B and G represent CTE ($23.6 \times 10^{-6} \text{ K}^{-1}$ for Al and $4.0 \times 10^{-6} \text{ K}^{-1}$ for AlN), volume fraction, bulk modulus (75.2 GPa for Al and 202 GPa for AlN) and shear modulus (26.2 GPa for Al and 126 GPa for AlN), respectively, and subscripts c, m and p refer to composites, matrix and particles, respectively. The correspondence between CTE of the present composites and Kerner's model indicates that the AlN particles introduce a constraint on thermal expansion of the Al matrix [2], resulting from their strong interfacial cohesion that was shown by microstructures above [**Figure 3.5(b) and (c)**].

Figure 3.7 shows correlation between TC and interfacial thermal resistance (ITR) in developed Al-AlN composites and various ex-situ AMCs (V_p of 2nd phase in the composites is marked with number) [38-40, 47, 48]. TC of as-rolled Al-AlN composites is 194 W/m·K, 178 W/m·K and 163 W/m·K for the samples with 20 vol.%, 30 vol.% and 40 vol.% of AlN, respectively. The decrease in TC with increasing V_p of AlN can be explained by H-J model [49], which describes effective TC of particulate composites as follows;

$$K_c = K_m \frac{[2(\frac{K_p}{K_m} \frac{K_p}{rh} - 1)V_p + \frac{K_p}{K_m} + \frac{K_p}{rh} + 2]}{[(1 - \frac{K_p}{K_m} + \frac{K_p}{rh})V_p + \frac{K_p}{K_m} + \frac{K_p}{rh} + 2]} \quad (3.2)$$

where K , r and h represent TC, radius of particles, and reciprocal of ITR. TC of composites decreases with increasing V_p and decreasing size of particles due to the increase in total interfacial area that acts as a barrier to thermal conduction. In particular, it should be mentioned that in-situ AMCs with AlN nanoparticles showed invalid ITR due to poor interface stability by oxide layer. Thus, it is expected that the present composites (d_p : 5 μm) exhibit higher TC than AMCs reinforced with in-situ formed AlN (d_p : 50 nm) fabricated by arc plasma evaporation and hot-pressing [38]. ITR of composites is affected by interfacial adherence that can be degraded by formation of interfacial gap or compound layer. Calculated ITR of the present composites was about $1.5 \times 10^{-8} \text{ m}^2\text{K/W}$ that is similar to that of AMCs produced by pressure-assisted infiltration [39] or squeeze casting [40], and that is about ten times lower than that of plasma-sprayed AMCs which exhibit poor interfacial bonding such as interfacial gaps or sprayed layer-layer boundary [47, 48]. The low ITR of the present composites is attributed to strong interfacial bonding between Al and AlN without any interfacial compound layer.

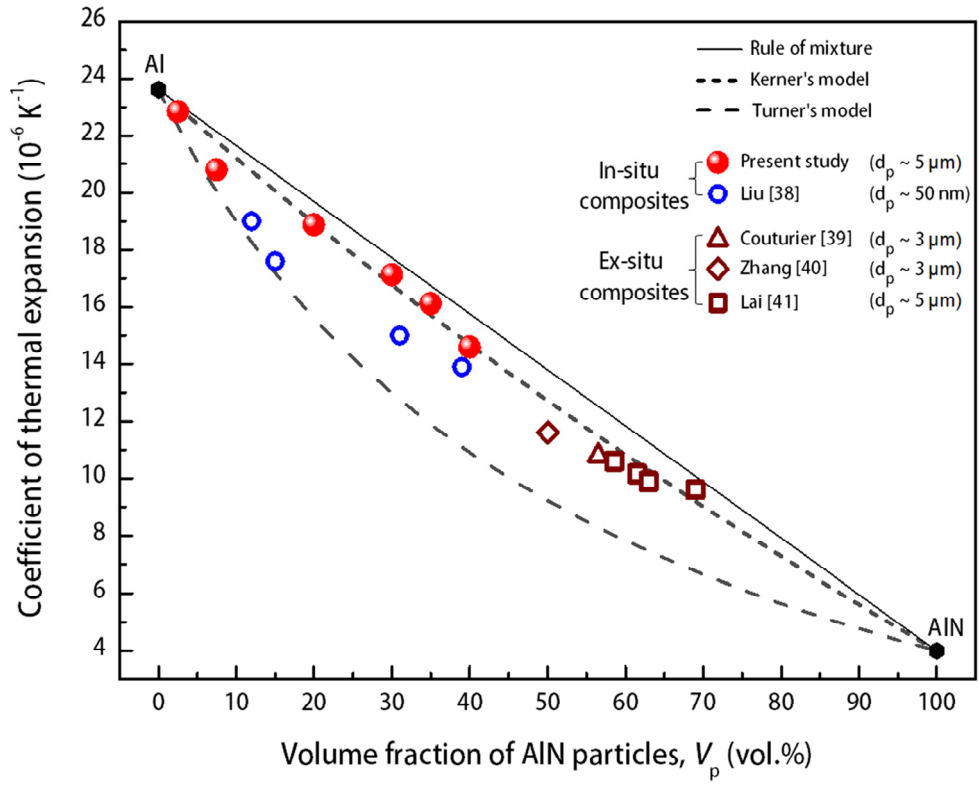


Figure 3.6 CTE of developed Al-AlN composites compared with that of various reported Al-AlN composites and theoretically predicted values [38-41].

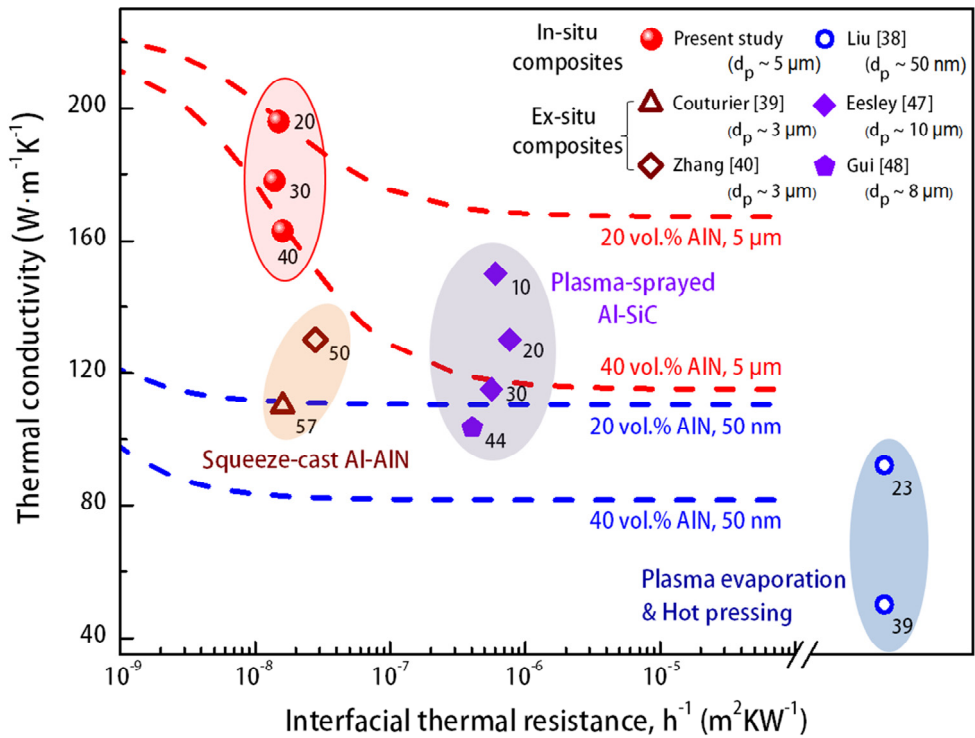


Figure 3.7 Correlation between TC and ITR in the composites and various ex-situ AMCs (V_p of 2nd phase is marked with number) [38-40, 47, 48]. Note that the in-situ AMCs with AlN nanoparticles showed invalid ITR due to their large oxygen contents and poor interface stability [38].

3.2.3. Formation mechanism and kinetics of AlN in APAVN process

Our results demonstrate the feasibility of in-situ forming Al-AlN composites by APAVN through arc melting of pure Al with N₂ gas. Formation of AlN (Al+N=AlN, ΔH= -322 kJ/mol) is thermodynamically favorable, but oxygen content in N₂ gas should be carefully controlled to reduce deleterious effects of oxygen on the nitridation of Al [30]. The addition of Mg in Al alloys was effective to initiate nitridation of Al melt since Mg acts as an oxygen getter [35] and a catalysis by forming intermediate Mg₃N₂ phase that reacts with Al (2Al+Mg₃N₂→2AlN+3Mg) [27]. However, TC of Al matrix significantly deteriorates with the addition of Mg [42], which reduces applicability of AMCs to heat sink applications. In this study, Al-AlN composites with high V_p of AlN (up to 40 vol.%) were synthesized within 180 seconds by newly developed APAVN process of pure Al melt with commercial N₂ gas. The formation mechanism and formation kinetics of AlN in APAVN process were carefully discussed and compared with gas bubbling method where N₂ gas is directly injected to Al melt and results in mainly surface nitridation.

3.2.3.1. Evaluation of AlN formation mechanism in APAVN process

Figure 3.8 graphically illustrates the detailed AlN formation mechanism in APAVN process. Nitrogen molecules (N₂) are dissociated into atomic nitrogen (N) by arc plasma-induced ultra-high temperature [50] (Step 1). The dissociated N is dissolved to Al melt through gas-melt interface subjected to elevated temperature over 2000 K [44, 45] (Step 2). It should be noted that dissolution of dissociated N into Al melt is instantaneous due to absence of activation energy for the chemisorption [**Figure 3.9(a)**] [51], while chemisorption of N₂ requires overcoming activation energy barrier (308 kJ/mol) due to the transition from physisorbed state to

chemisorbed state [**Figure 3.9(a) and (b)**] [36]. Furthermore, solubility of N in Al at 2000 K was estimated to be about 0.3 at.% [52], indicating that dissolution of dissociated N is thermodynamically favorable at the gas-melt interface. Thus, arc melting method can be an effective route to dissolve significant amount of N into Al melt and improved wettability, leading to volume nitridation of Al. Thus, AlN is explosively in-situ formed at inside melt as well as gas-melt interface (Step 3). Due to strong temperature gradient of Al melt cooled by copper hearth, N₂ bubbles are recombined at the bottom of the Al melt [50] (Step 4), resulting in formation of AlN particles during the rise of the bubbles in the Al melt with high content of dissolved N [28] (Step 5). The in-situ formed AlN in Step 5 exhibited different morphology compared to the AlN formed in Step 3, which will be discussed in **Figure 3.10**. The bubbles escape from the Al melt due to buoyancy force and N₂ molecules are released from the bubbles (Step 6).

Figure 3.10 shows schematic diagrams for two representative AlN morphologies formed by APAVN process (Step 3 and Step 5 in **Figure 3.8**). First, AlN synthesized in Step 3 exhibited the form of plates with large area [**Figure 3.10(b)**], which is a typical morphology of AlN formed at the surface of Al melt. Thickness of the plates was close to 5 μm, which is larger than that of AlN layer (350 nm) formed on surface of liquid Al under N₂ atmosphere at 973 K [53], indicating that formation of thicker AlN plates with large area (> 100 μm in diameter) is favorable in APAVN process. During arc melting, the in-situ formed plates sank to the bottom of Al melt due to the difference in their density (2.7 g/cm³ for Al and 3.3 g/cm³ for AlN), and improved wettability between AlN and Al melt by arc plasma-induced ultra-high temperature results in continuous wetting of the Al melt through surface of AlN plate. Consequently, new plates were synthesized at the gas-melt interface, which leads to

stacking of AlN plates in the whole Al melt. Simultaneously, AlN rods appeared to grow from the plates toward the gas-melt interface [Figure 3.10(b)]. The unidimensional growth of AlN can be explained by vapor-liquid-solid (VLS) growth mechanism [54] in which supersaturation of liquid Al by N promotes anisotropic crystal growth of the AlN from the plates [55]. The supersaturation may result from delayed convection of Al melt between the pre-stacked plates where the dissolved N is locally enriched. Second, AlN synthesized in Step 5 exhibited the form of agglomerates of small AlN particles ($d_p < 2.5 \mu\text{m}$) [Figure 3.10(c)]. Growth of the agglomerates was initiated from AlN seed, formed at the interface between Al melt and N_2 bubble [27], toward the gas-melt interface due to the gradient of dissolved N. The appearance of the agglomerates was similar to the surface of nitrided Al powder at the temperature below 1273 K [53, 56], indicating limited growth of AlN crystals due to the relatively low temperature. Figure 3.11(a) shows the TEM image that the agglomerates were well-bonded with Al matrix even at the narrow interspacing of AlN, indicating that the in-situ formed AlN was completely wet by Al melt through the arc plasma-induced reaction. The wettability between a ceramic and a melt can be improved by the electrowetting on dielectric (EWOD) effect [57]. The EWOD effect on the ceramic substrate is caused by an external voltage applied to the liquid [Figure 3.11(b)]. In the APAVN process, arc voltage imposed on the apparatus was 20 V, which can reduce the contact angle significantly [57, 58]. Thus, the enhanced wettability of AlN by Al melt can be explained by the EWOD effect as well as arc plasma-induced high temperature.

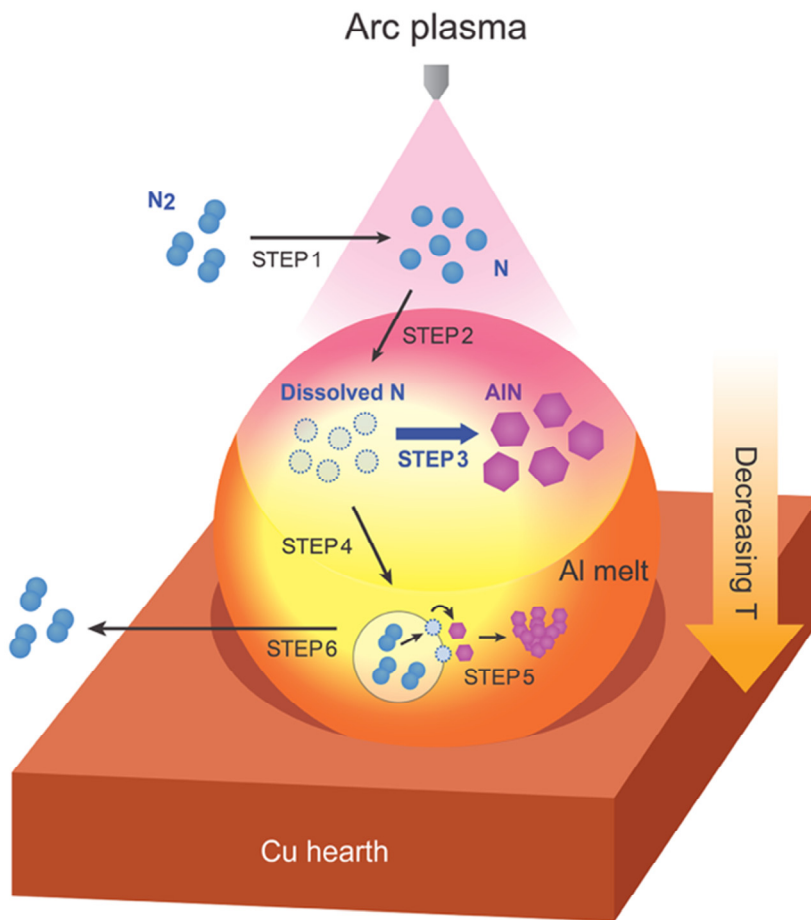


Figure 3.8 Schematic diagram showing AIN formation mechanism in APAVN process.

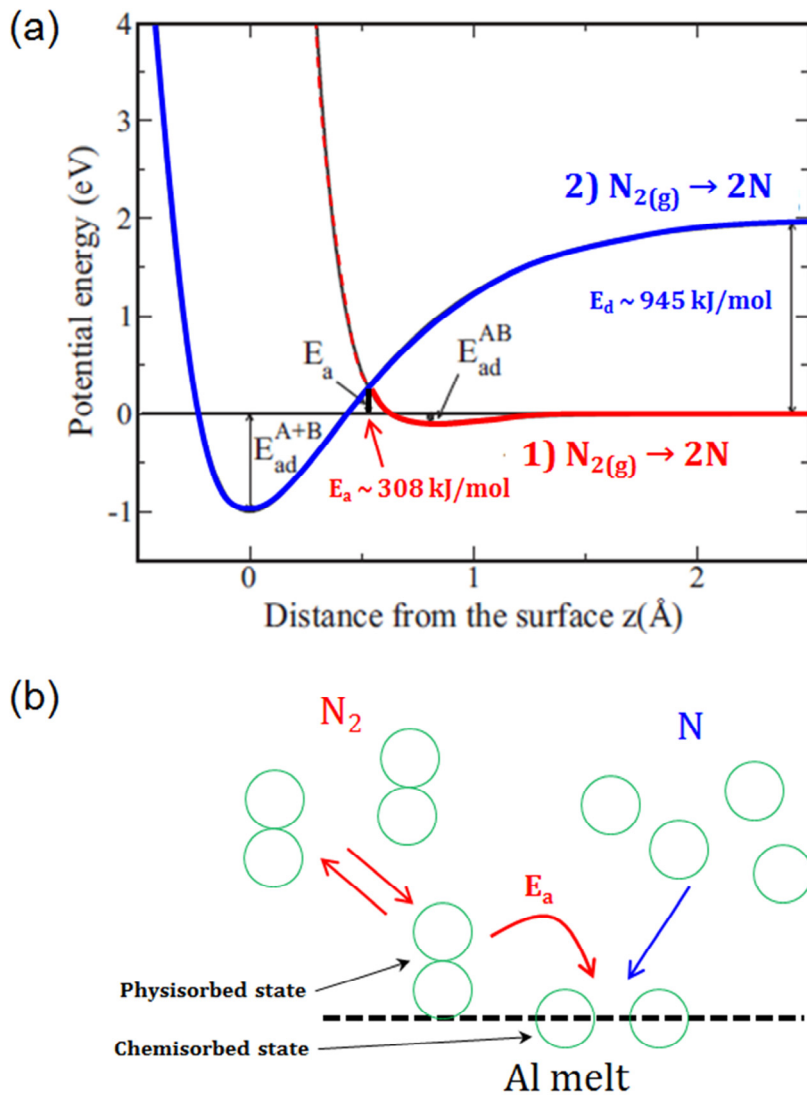


Figure 3.9 (a) Potential energy curves for dissociative adsorption of N_2 molecule and (b) schematic diagrams for a gas surface adsorption model [36].

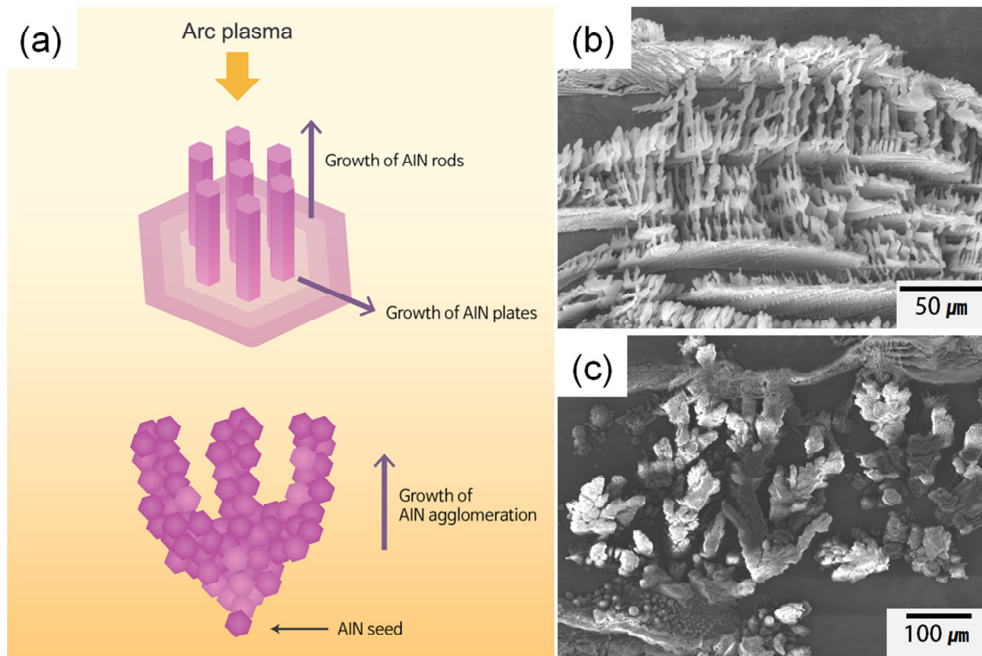


Figure 3.10 (a) Schematic diagram showing two representative AlN morphologies formed in as-melted Al-AlN ingot via APAVN process. SEM images of (b) plate-shaped AlN with rods (upper part of ingot) and (c) agglomeration of AlN particles (bottom part of ingot) after nitridation time of 60 seconds in APAVN process.

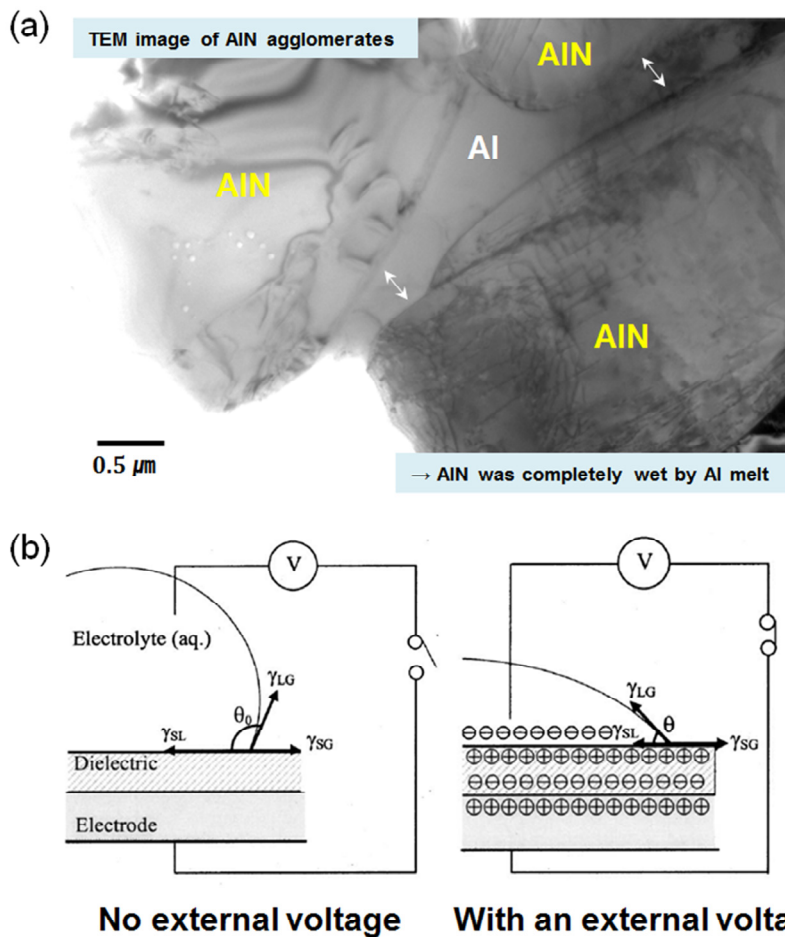


Figure 3.11 (a) A TEM image of AlN agglomerates and (b) principle of electrowetting without and with external voltage applied. The contact angle decreases or increases as charge density at dielectric changes [57]. Reprinted from J. Appl. Phys., 92, 7, H.Moon, S.K. Cho, R.L. Garrel and C.J. Kim, Low voltage electrowetting-on-dielectric, 4080, Copyright (2002), with permission from AIP Publishing.

3.2.3.2. Comparison of AlN formation rate between APAVN process and gas bubbling method

Since the AlN formation rate (θ_{AlN}) in gas bubbling method was evaluated by considering concentration and diffusion of the dissolved N in Al melt [28, 29], the predominance of N diffusion in this study was investigated by determining concentration profiles. The diffusion of N in Al melt was estimated by Fick's second law as follows;

$$\frac{\partial C_N}{\partial t} = D_N \frac{\partial^2 C_N}{\partial x^2} \quad (3.3)$$

where C is concentration (in moles per liter), and D_N is diffusivity of N in Al melt as follows;

$$D_N = D_0 \exp\left(-\frac{E_N}{RT_1}\right) \quad (3.4)$$

where D_0 is pre-exponential constant, 3.75×10^{-7} m²/s, and E_N is activation energy for N diffusion, 26.47 kJ/mol [29]. R is gas constant and T_1 is Al melt temperature. With boundary conditions (at $x=0$, $C_N=C_{N,i}$ and at $x=\infty$, $C_N=0$), equation (3) yields a solution as follows;

$$C_{N,x} = C_{N,i} \left(1 - \operatorname{erf}\left(\frac{x_N}{2\sqrt{D_N t_N}}\right)\right) \quad (3.5)$$

where x_N and t_N are diffusion length and time of N, respectively. $C_{N,x}$ and $C_{N,i}$ are concentration of N at the distance x from the gas-melt interface and at the gas-melt interface, respectively. $C_{N,i}$ was evaluated as follows;

$$C_{N,i} = k C_{N,g} \quad (3.6)$$

where k and $C_{N,g}$ are dimensionless Henry's law constant and concentration of nitrogen gas in chamber, respectively. $C_{N,g}$ was evaluated as follows, assuming that the gas obeys ideal gas law ($PV=nRT$);

$$C_{N,g} = \frac{P_N}{RT_N} \quad (3.7)$$

where P_N and T_N refer to partial pressure and temperature of nitrogen gas. **Figure 3.12** shows the diffusion profiles of dissociated N in Al melt for APAVN process, calculated using equation (3.3-3.7), which was compared against those of N_2 gas for gas bubbling method [36]. Although P_N of APAVN process (0.2 atm) is lower than that of gas bubbling method (1.0 atm), the APAVN process exhibited higher $C_{N,i}$ (9.22×10^{-4} mol/L) than gas bubbling method (1.65×10^{-4} mol/L [36]) due to the difference in h in equation (3.6). In APAVN process, the k can be assumed as 1 since dissociated N by arc plasma is instantaneously dissolved into Al melt without overcoming activation energy (Step 2 in **Figure 3.8**). In gas bubbling method, the k was estimated as 1.99×10^{-2} at 1473 K that was derived from solubility of N in Al [59]. The θ_{AIN} in gas bubbling method was calculated by the equation, $\theta_{AIN} = a \cdot D_N^{0.5} C_{N,i}$ (a is constant) since formation of AlN occurs mainly at the gas-melt interface and C_N is much smaller than C_{Al} in the Al melt (surface nitridation) [29]. Based on the same assumption, θ_{AIN} in APAVN process is about ten times higher than that in gas bubbling method, since T_N is higher over 1000 K, and $C_{N,i}$ is about 5.6 times greater. However, it is insufficient to explain about 400 times higher specific weight gain normalized by t_N in APAVN process compared to that in gas bubbling method. Compared to gas bubbling method where nitrogen bubbles escape from Al melt within a few seconds, the dissociated N in APAVN process is continuously supplied to Al melt during nitration, resulting in volume nitridation as explained in **Figure 3.10(b)**. Therefore, the higher V_p of AlN in APAVN process can be rationalized by unique volume nitridation due to increased $C_{N,i}$ from the instantaneous chemisorption of dissociated N, increased $C_{N,x}$ from the enhanced N diffusion in Al melt, and improved wettability between AlN and Al melt.

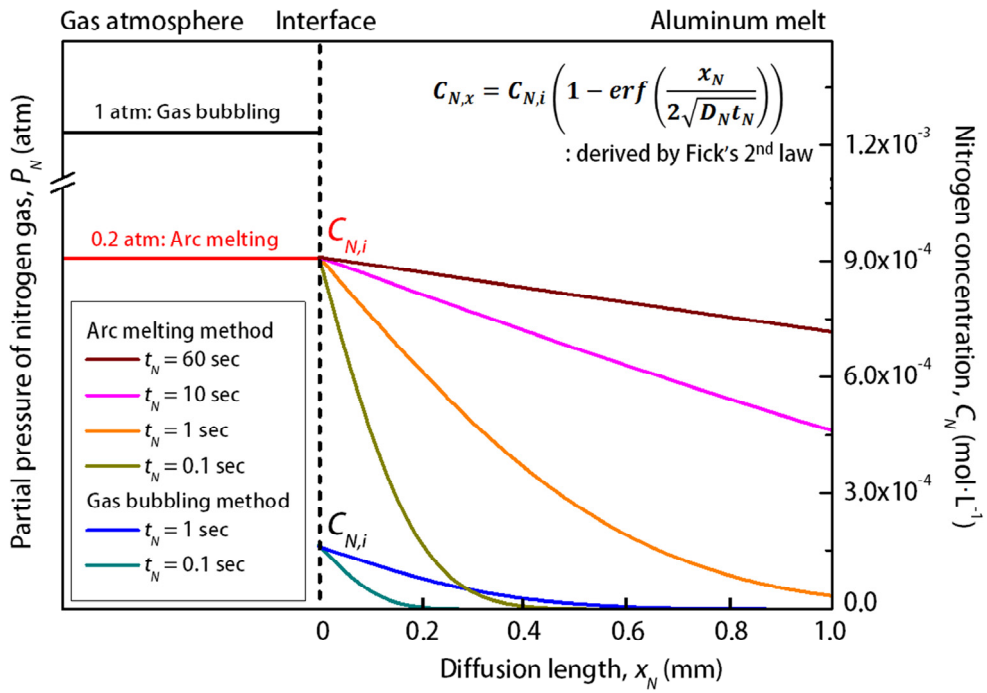


Figure 3.12 Diffusion profiles of N in Al melt for APAVN process compared with those for gas bubbling method [36].

3.2.3.3. Manipulation of thermal properties via APAVN process

Figure 3.13 shows specific TC of as-rolled Al-AlN composites via APAVN process compared with various pure metals, ceramics and AMCs as a function of CTE [38-40, 47, 48]. When it comes to materials choice for heat sink applications, the density is a major consideration. Late transition metals such as Mo and W were well known for their high TC with low CTE, but their high density limits their use. The as-rolled Al-AlN composites exhibited unique combination of higher specific TC and lower CTE than in-situ Al-AlN nanocomposites [38] or plasma-sprayed AMCs [47, 48], which can be manipulated by controlling V_p as well as size of AlN. Furthermore, ITR of Al-AlN interface, prepared by sputtering of Al on AlN single crystal in vacuum, is $4.3 \times 10^{-9} \text{ m}^2\text{K/W}$ [60], indicating that TC of the present composites can be further improved by optimizing processing parameters to reduce ITR. Consequently, the present Al-AlN in-situ composites formed by APAVN process exhibit attractive combination of higher specific TC and lower CTE as well as reduced materials cost; therefore, it seems promising for heat sink applications, especially for portable electronic devices.

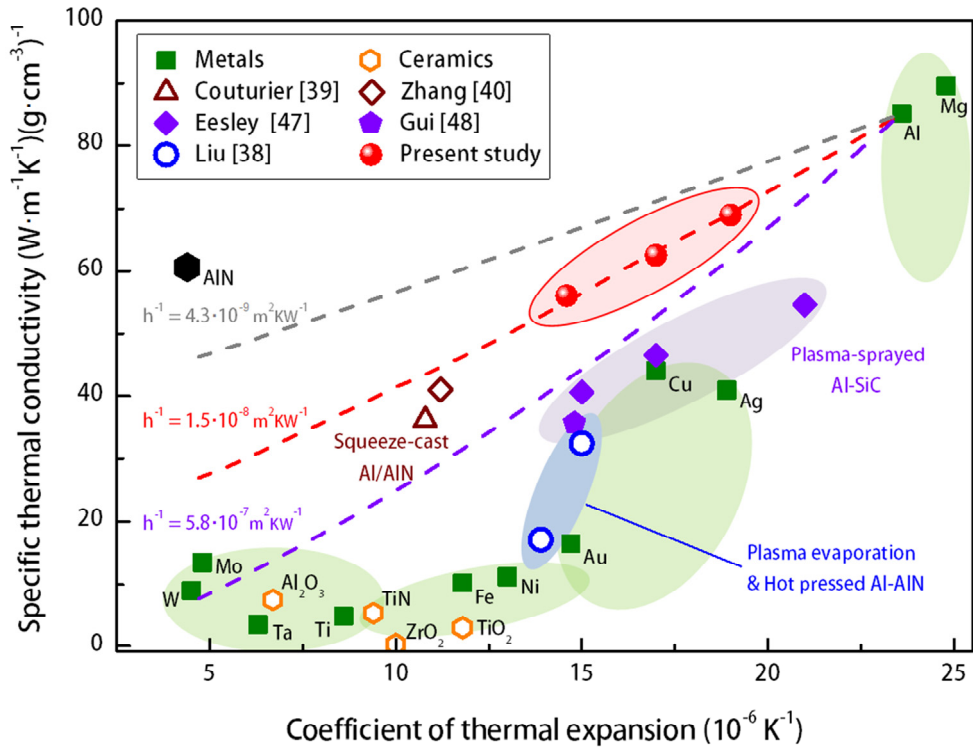


Figure 3.13 Correlation between specific TC and CTE of the Al-AIN composites fabricated via APAVN process in relation to various metals, ceramics and AMCs [38-40, 47, 48].

3.3. Conclusions

The present study shows the in-situ synthesis of Al-AlN composites with attractive thermal properties via APAVN process. APAVN resulted from instantaneous chemisorption of dissociated nitrogen, enhanced diffusion of the dissolved nitrogen in Al melt and improved wettability between AlN and Al melt, which leads to higher AlN formation of $\sim 2.94 \times 10^{-1} \text{ g/min}\cdot\text{cm}^3$, about 400 times higher than that in gas bubbling method ($6.91 \times 10^{-4} \text{ g/min}\cdot\text{cm}^3$). Thus, within a few minutes of repeated APAVN under commercial N_2 gas, volume fraction of AlN increased up to 40 vol.%, which is the highest value ever reported by in-situ nitridation of pure Al melt using high-purity N_2 gas. The composites contained homogeneously dispersed AlN particulates with strong interfacial bonding and low ITR, which results in unique combination of relatively low CTE ($14.6 \times 10^{-6} \text{ K}^{-1}$) and high TC (163 W/m·K). Our current finding gives us a guideline on how to design a simple process for continuous production of in-situ Al-AlN composite sheets with tailor-made thermal properties for heat sink applications.

CHAPTER 4

In-situ synthesis of aluminum matrix composites with high volume fraction of nitride ceramics by arc plasma-induced accelerated displacement reaction

4.1. Introduction

There is considerable interest in the development of new electronic packaging materials for the reliability of high-power electronic devices [4]. Aluminum matrix composites (AMCs) have received much attention in the thermal management industry due to their light-weight, high thermal conductivity and excellent dimensional stability. To meet the demand for the minimization of thermal stress induced by coefficient of thermal expansion (CTE) mismatch, it has been required to fabricate the AMCs with a high volume fraction of ceramic reinforcements more than 60 vol.% for thermal management of electronics [20]. Pressure infiltration process has been developed to fabricate the composites with relatively high fraction of reinforcements more than 50 vol.% [18]. Recently, the AMCs with volume fraction of reinforcements up to 85 vol.% have been produced by using the preform with interpenetrating network structure [21, 61]. However,

the interconnected preforms were prepared by sintering the green bodies at very high temperature (up to 2673 K for SiC reinforcement) and external pressure around 10 MPa was required to infiltrate the preform with Al melt [21], which is impractical to be applied for the continuous production of composites with high volume fraction of reinforcements..

Aluminum nitride (AlN) is an attractive reinforcement for the AMCs due to its high thermal conductivity, low CTE and thermodynamical stability in Al matrix [30]. Thus, in-situ formation of the AMCs with AlN has been investigated during the past decades and various processes like direct melt nitridation [25] or gas bubbling method [27, 28], where nitrogen bearing gas reacts with Al melt, has been developed. However, the gas-melt reaction requires high processing temperature above 1273 K and long processing time (more than 10 h in direct melt nitridation [35]) that are uneconomical to be used in heat sinks. The temperature dependence of standard free energies of the nitrides is shown in **Figure 4.1(a)** [62]. The in-situ formation of AlN can be expected by the displacement reaction between Al melt and Si₃N₄ as follows [62];



where Si diffuses out of Si₃N₄ during the reaction, and dissolves in the Al melt.

Figure 4.1(b) shows the contact angles of various liquids on Si₃N₄ as a function of temperature [63-66]. Due to the poor wettability, the infiltration of Al melt into Si₃N₄ preform (50 vol.% – 60 vol.% in volume fraction) should be assisted by external pressure above 40 MPa at 1223 K – 1273 K [67, 68]. The AMCs with Si₃N₄ have been fabricated by pressureless infiltration of Al-Mg alloys where the wettability of Si₃N₄ by Al melt was improved by the addition of Mg [66], but the spontaneous infiltration requires long processing time.

In the present study, we report the in-situ formation of AMCs with high

volume fraction of reinforcements by arc plasma-induced accelerated displacement reaction (APADR) between pure Al melt and Si_3N_4 . In APADR process, the Si_3N_4 powder preforms were spontaneously infiltrated with the Al melt, and AlN was formed by displacement of Si from Si_3N_4 and its replacement by Al by arc plasma-induced high temperature. The microstructure and thermal expansion behavior of the composites were systematically characterized.

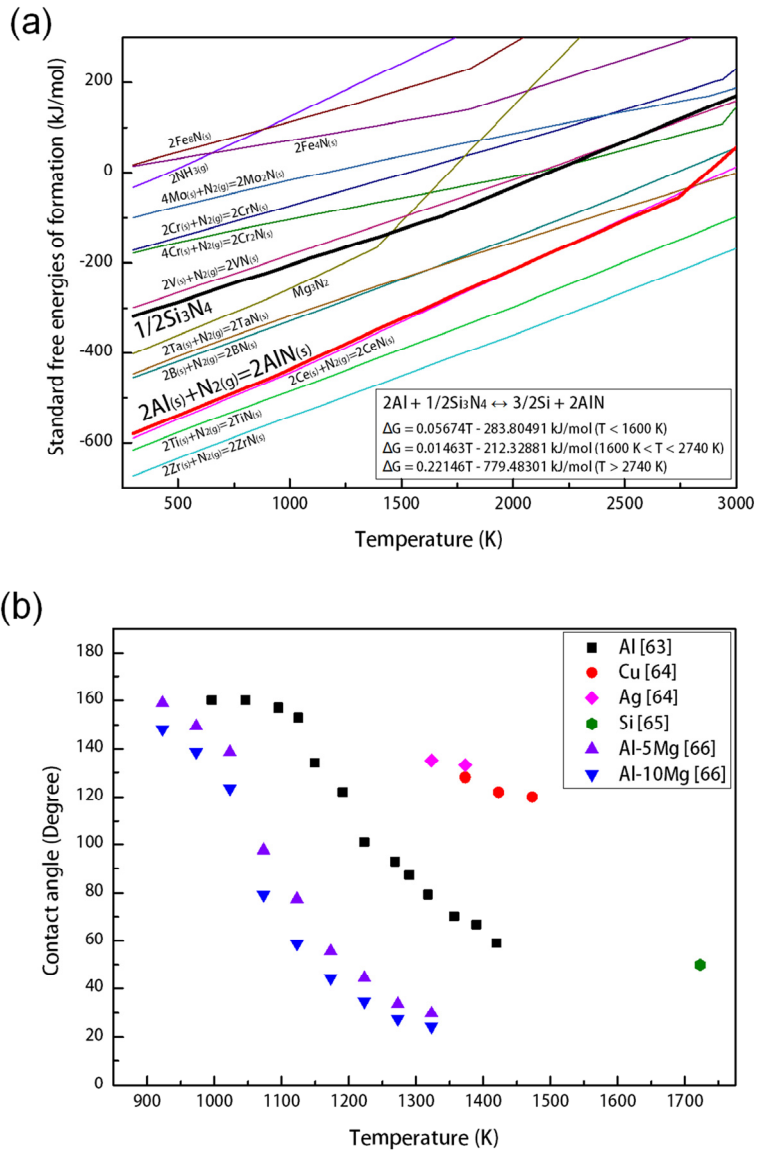


Figure 4.1 (a) The standard free energies of the nitride ceramics as a function of temperature [62] and (b) contact angle between molten alloy and Si_3N_4 substrate [63-66].

4.2. Results and discussion

The AMCs in the study were prepared by arc melting method with a constant arc voltage of 20 V and arc current of 150 A. **Figure 4.2** illustrates the sequence of APADR process fabricating AMCs with high volume fraction of reinforcements. A piece of Al (99.999 % purity), placed on the pressed Si_3N_4 preform, was melted under a Ti-gettered Ar (99.999 % purity) atmosphere of 40 kPa in total pressure [**Figure 4.2(a)**]. After the melting, the preform was covered with molten Al, leaving reaction layer at the periphery of the preform [**Figure 4.2(b)**]. The formation of reaction layer is attributed to the high temperature of Al melt, but the growth of the layer was limited due to fast cooling of the Al melt by water-cooled copper hearth. When the Al- Si_3N_4 piece was turned over and arc-melted again, arc plasma was generated toward the surrounding Al to avoid thermal shock of the preform [**Figure 4.2(c)**]. During the arc melting, a small amount of Al melt was evaporated from the piece, which may result from the high temperature of arc plasma [50] and the highly exothermic reaction between Al and Si_3N_4 ($\Delta H = -293$ kJ/mol at $T = 1500$ K [62]). The Si_3N_4 preform was simultaneously infiltrated and reacted with the Al melt, resulting in the formation of AlN-(Si_3N_4) reinforced AMCs [**Figure 4.2(d)**]. Si_3N_4 powder preforms with green density of 45 vol.% (preform S45) and 65 vol.% (preform S65) were prepared by compacting single (for the preform S45) or bimodal powder mixture (for the preform S65). The resulting composites fabricated from the preform S45 and S65 via APADR process will be referred as composite A55 and composite AS73, respectively.

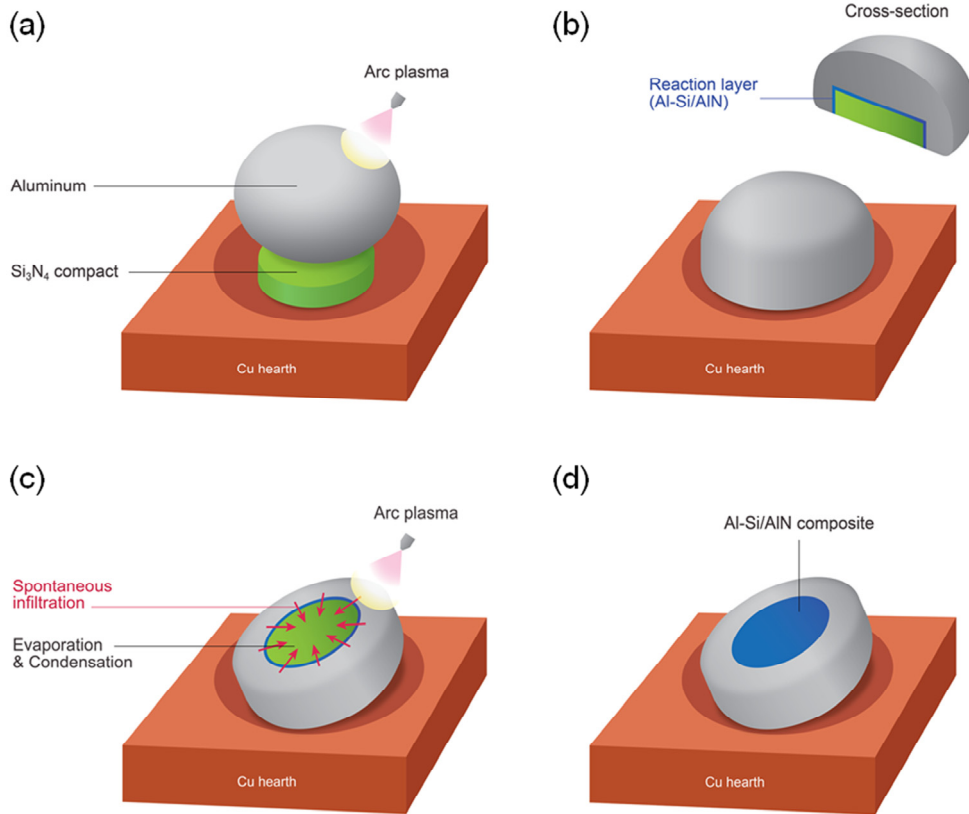


Figure 4.2 Schematic diagram showing processing procedure for the fabrication of Al-Si-AlN-(Si_3N_4) composites by APADR process.

4.2.1. Microstructures

Figure 4.3 shows XRD profiles of the composites prepared by the preform S45 and preform S65 infiltrated with the Al melt. The composite A55 showed three diffraction peaks of Al, Si and AlN, indicating all the fine Si_3N_4 particles were transformed to AlN particles according to Equation (4.1). The composite AS73 was composed of Si_3N_4 as well as Al, AlN and Si, indicating unreacted Si_3N_4 particles remained in Al matrix after the processing. Comparing with the XRD profile of the preform S65 (not shown), diffraction peaks of $\alpha\text{-Si}_3\text{N}_4$ were significantly reduced in the composite AS73. The distinctive reduction in peak intensity of $\alpha\text{-Si}_3\text{N}_4$ may result from $\alpha\text{-}\beta$ transformation in Si_3N_4 , which occurs over 2023 K without any sintering additives such as MgO or Y_2O_3 [69]. The Al melt that infiltrates the Si_3N_4 preform can be locally heated to the elevated temperature higher than 2000 K by arc plasma [44, 50] or exothermic heat that resulted in vaporization of Al melt, which can rationalize the $\alpha\text{-}\beta$ transformation of Si_3N_4 during the arc melting.

Optical micrograph of the composite A55 is present in **Figure 4.4(a)**. Uniform distribution of bright (Al-Si) and dark (AlN) phases was shown, which is similar to the microstructure of interpenetrating composites [70]. SEM observation [**Figure 4.4(b)**] revealed that the phases of gray, dark gray and bright contrast were identified as Al, Si and AlN by EDS analysis. The formation of co-continuous microstructure was attributed to the aggregation of the fine particles during the compaction, and sintering of the nitride phases due to the arc-plasma induced high temperature [44] and the highly exothermic reaction between Al and Si_3N_4 . The ligament size of Al matrix and AlN was measured to about 0.395 μm and about 0.6 μm , respectively. Si phase, which size is in range from 0.1 μm to 0.4 μm in size, appeared to be precipitated from the Al melt during the

solidification. Volume fraction of Al, Si and AlN phase was confirmed to 41 vol.%, 4 vol.% and 55 vol.%, respectively.

Figure 4.5(a) shows optical micrograph of the composite AS73. The microstructure revealed bimodal particle distribution in which the coarse particles were identified as Si_3N_4 , and the interspacing between the coarse particles was composed of Al-Si matrix, AlN AlN Si_3N_4 phases. Microstructural features of the interspacing were present in Figure 5(b). AlN particles are uniformly distributed in the matrix, but the degree of interconnection in the composite AS73 was reduced compared with that in the composite A55 [**Figure 4.4(b)**]. The ligament size of Al matrix was 0.987 μm and the size of AlN particles is in range from 0.2 μm to 5.0 μm . The size of Si phase was in range from 0.4 μm to 1.0 μm , which is larger than the composite A55. Volume fraction of Al, Si and nitride particulates (AlN and Si_3N_4) in the B composite was confirmed to 25 vol.%, 2 vol.% and 73 vol.%, respectively. In case of nitride particles with diameter larger than 5 μm , residual Si_3N_4 phase was observed inside the aggregation of AlN particles [marked in **Figure 4.5(b)**]. The unreacted Si_3N_4 exhibited rough and irregular edge compared with the smooth edge of AlN particles. The formation mechanism of AlN as well as the morphology of the unreacted Si_3N_4 will be discussed later.

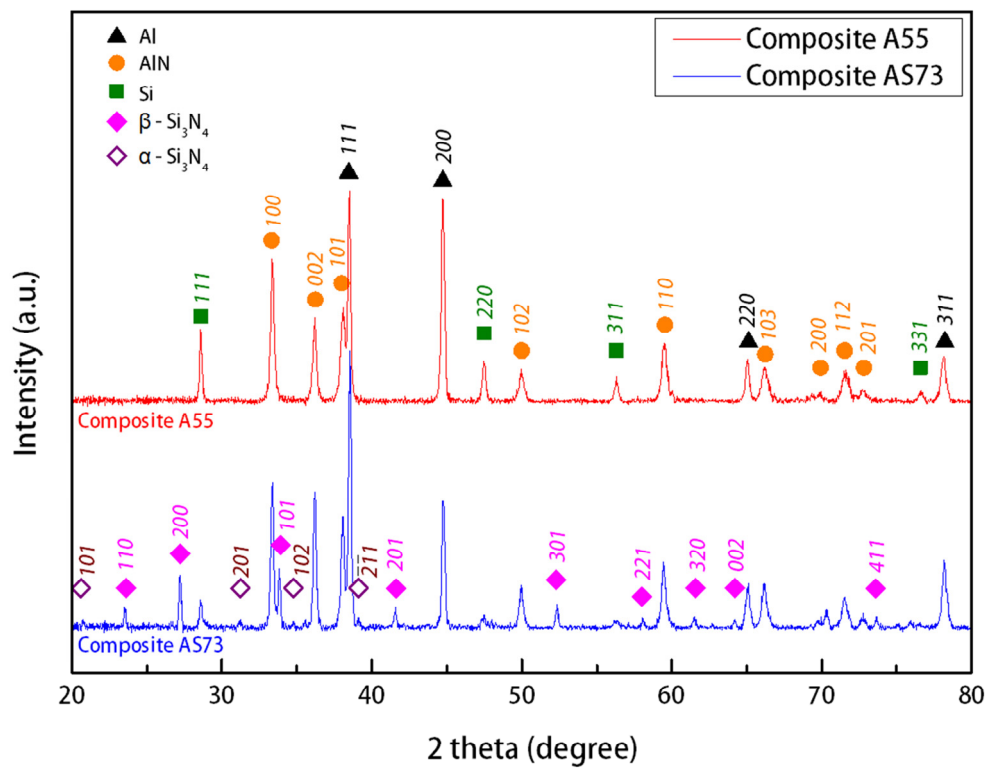


Figure 4.3 XRD patterns of the Al-Si-AlN-(Si₃N₄) composites fabricated by APADR process.

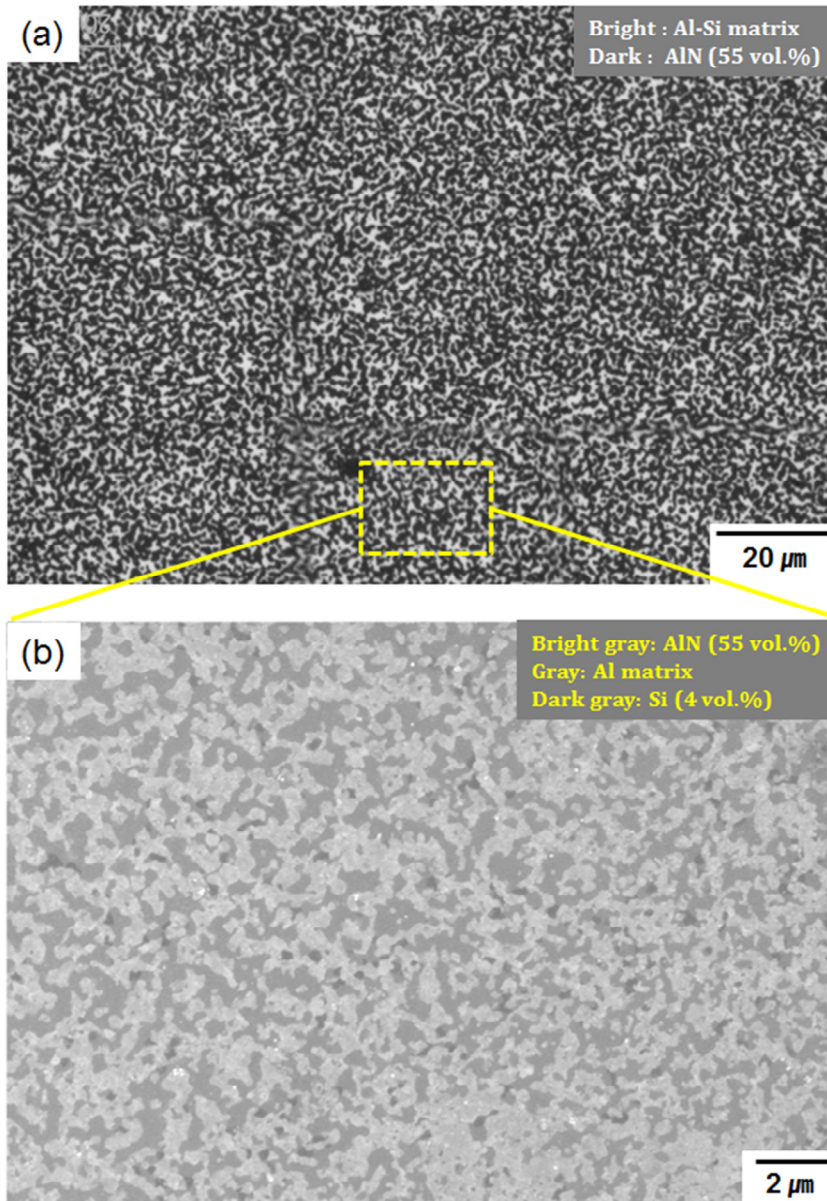


Figure 4.4 (a) OM micrograph and (b) SEM micrograph of the composite A55.

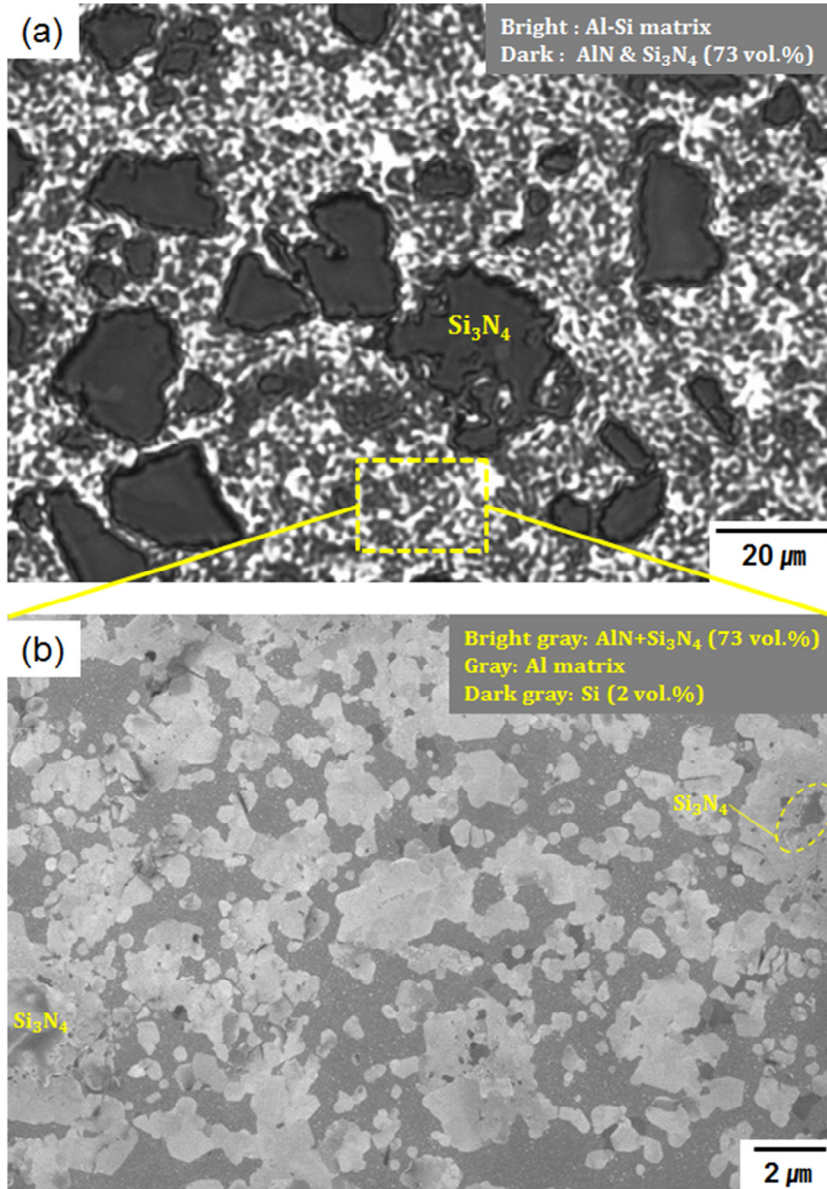


Figure 4.5 (a) OM micrograph and (b) SEM micrograph of the composite AS73.

4.2.2. Pressureless infiltration

In arc plasma processing, the Si_3N_4 powder preforms were infiltrated by Al melt without the aid of an external pressure. The pressureless infiltration of the Al melt can be driven by capillary pressure:

$$\Delta P = -\frac{2\gamma_{lv} \cos \theta}{r_c} \quad (4.2)$$

where γ_{lv} , θ and r_c are liquid-vapor surface tension, contact angle between the Si_3N_4 particles and the Al melt, and capillary radius of the preforms, respectively. The r_c for a powder preform can be estimated by [71]:

$$r_c = \frac{d_p v_p}{3\lambda(1-w)} \quad (4.3)$$

where d_p was mean diameter of the particles, v_p was volume fraction of porosity in the powder preform and λ was geometry factor that is usually taken to be 1.4 [71]. **Figure 4.6** showed the estimated capillary pressure for the infiltration of Al melt through the Si_3N_4 powder preforms S45 and S65 as a function of temperature calculated by using Equation (4.2) and (4.3). The calculated r_c for the preform S45 ($d_p = 0.6 \mu\text{m}$ and $v_p = 0.55$) was $0.175 \mu\text{m}$ that is similar to $0.197 \mu\text{m}$ obtained by measuring interspacing of AlN phase in Fig. 4(b). For the preform S65, the interspacing of AlN phase ($0.494 \mu\text{m}$) measured in **Figure 4.5(b)** was employed. The surface tension of the Al melt varied according to the following equation [$\gamma_{lv} = (868 - 0.152 \times (T - T_m)) \times 10^{-3}$ [45]], and the relationship between contact angle and temperature was obtained from the results of Nicholas et al [63]. In the two preforms, the capillary pressure were negative and higher than 1 MPa over 1350 K, which rationalizes the pressureless infiltration of Al melt through Si_3N_4 preforms in the arc melting method.

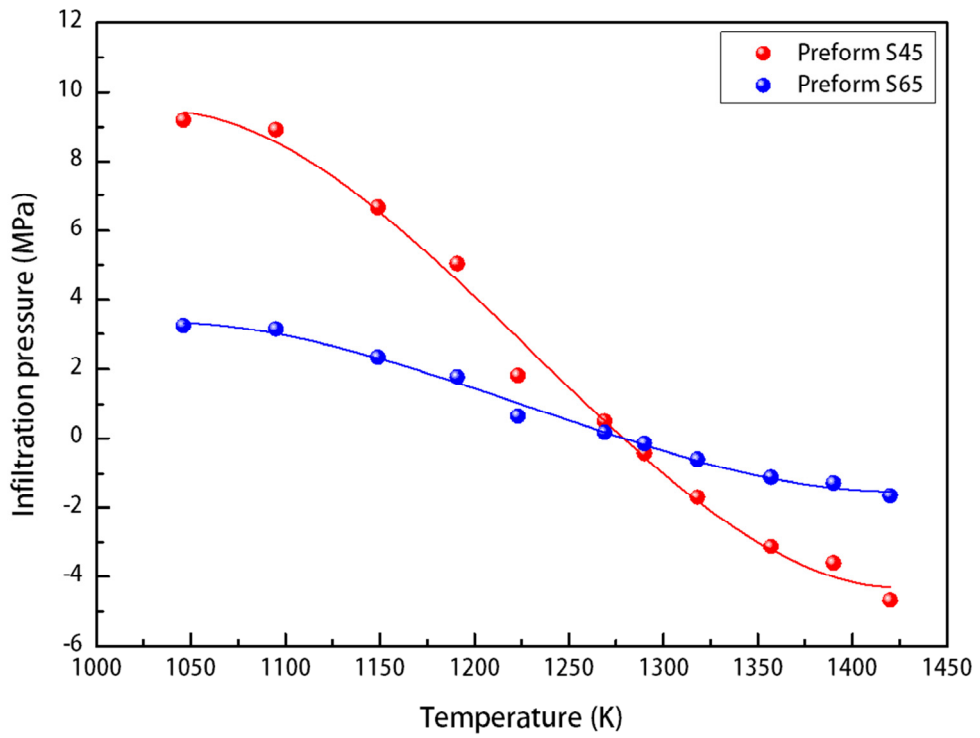


Figure 4.6 Temperature dependence of infiltration pressure of Al melt into the Si_3N_4 preform S45 and S65.

4.2.3. Formation mechanism

In the plasma processing, the Al melt subjected to elevated temperature simultaneously infiltrates the powder preforms and reacts with Si_3N_4 , resulting in the formation of nitride reinforced composites according to Equation (4.1). It should be noted that we found the difference in volume fraction of nitride phase between the preforms and the resulting composites (from 45 vol.% to 55 vol.% for the composite A55 and from 65 vol.% to 73 vol.% for the composite AS73). This can be understood by considering the Pilling-Bedworth Ratio (PBR) between reactant (Si_3N_4) and product (AlN) as follows:

$$\text{PBR} = 4 \times \frac{\text{molar volume of AlN}}{\text{molar volume Si}_3\text{N}_4} = 4 \times \frac{w_{\text{AlN}}\rho_{\text{Si}_3\text{N}_4}}{w_{\text{Si}_3\text{N}_4}\rho_{\text{AlN}}} \quad (4.4)$$

where w is molar mass and ρ is density of the nitrides. Since the nitrogen is supplied from solid phase, which is different from the case that the nitrogen is supplied from gas phase when a metal is nitrided, the molar quantity of nitrogen available for the reaction [Equation (1)] is fixed, thus the factor of 4 in Equation (4) arose from the stoichiometry of the reaction. The estimated PBR in the reaction was 1.13 that indicates that the transformation is accompanied by an approximately 13 % volumetric expansion, leading to the formation of protective AlN layer on Si_3N_4 . In both composites A55 and AS73, the in-situ formation of AlN from Si_3N_4 resulted in the increase of volume fraction of nitride phase in Al matrix. In the composite A55, the change in volume fraction of AlN was 22 %. The significant volume expansion of nitride phase over 13 % resulted from the aggregation and sintering of the fine nitride particles subjected to elevated temperature by arc plasma. The composite AS73 showed lesser change in volume fraction of nitride phase (12 vol.%) compared with the composite A55. This is attributed to the larger size of Si_3N_4 particles in preform S65 and the presence of unreacted Si_3N_4 phase in the resulting composites despite the

aggregation and sintering of the fine nitride particles. The mechanism for the formation of AlN and unreacted Si₃N₄ was illustrated in **Figure 4.7**. When the Si₃N₄ is submerged in Al melt, the displacement reaction occurred at the surface of Si₃N₄. Although Si diffuses out of the preform along the Al channels to the surrounding Al melt, the nitrogen reacted with Al and AlN phase initially formed at the surface of Si₃N₄ particles [72]. As the processing time by arc melting increased, the contact area between Al melt and Si₃N₄ was reduced by the formation and growth of AlN. As confirmed by PBR ratio, the AlN phase appeared to be grown at the periphery of Si₃N₄ and the path where Si and nitrogen dissolved from Si₃N₄ became narrow. Although the Al melt was constantly supplied, the in-situ reaction stopped due to the protective AlN layer, leaving unreacted Si₃N₄ and residual Al-Si melt in the inter-particle spacing. The unreacted Si₃N₄ exhibited rough and irregular edges that were shown in **Figure 4.5(b)**. The critical diameter of Si₃N₄ for the complete displacement reaction was about 5 μm. It should be noted that the thickness of AlN layer formed at the surface of Si₃N₄ was less than 0.1 μm in the Al - Si₃N₄ composites fabricated by pressure-assisted infiltration of 6061 Al alloy at 1073 K for 1 hour. Thus, Si₃N₄ in arc melting can be vigorously transformed into AlN in Al melt although the in-situ reaction provides the formation of protective AlN layer.

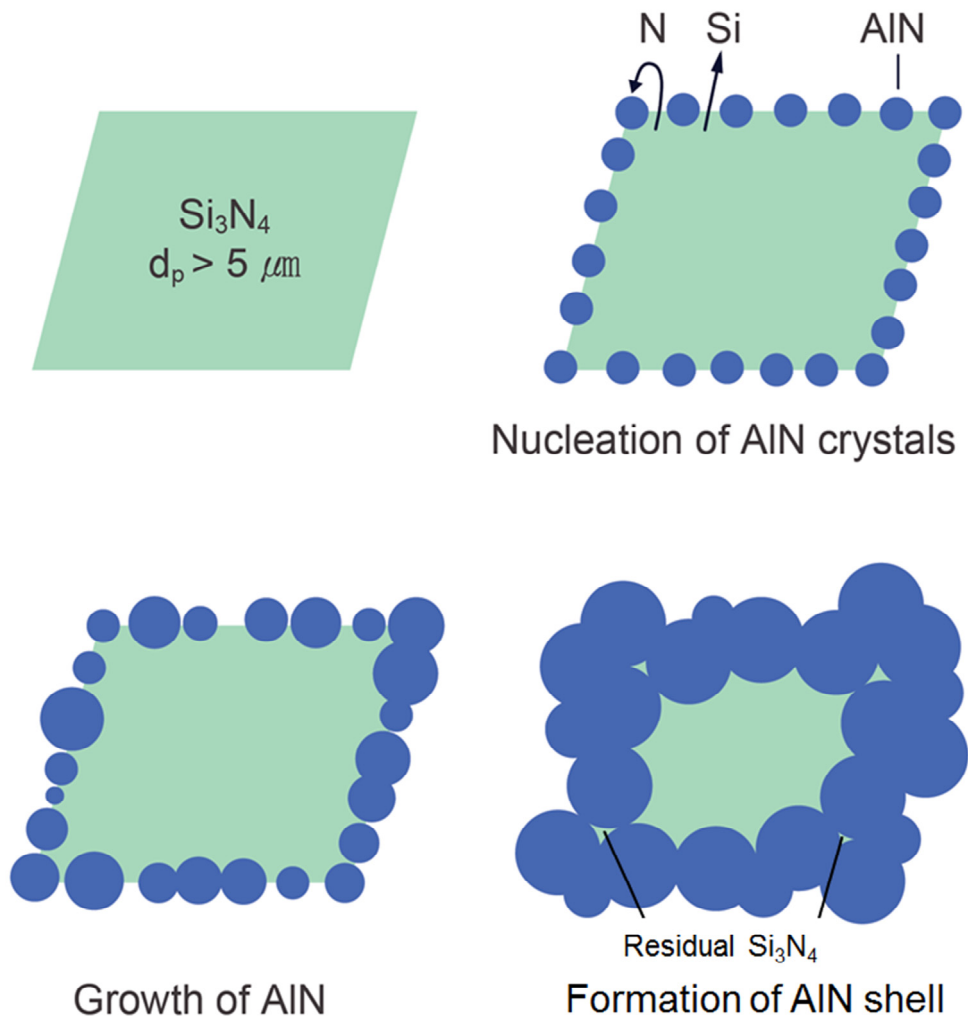


Figure 4.7 Schematic diagram showing the morphologies of in-situ formed AlN and residual Si_3N_4 phase in Al matrix during APADR process.

4.2.4. Thermal properties

Figure 4.8(a) shows linear expansion curves of the present composites A55 and AS73 with pure Al and in-situ Al-AlN composites as a function of temperature. With increasing volume fraction of nitride phases, the relative displacement ($\Delta L/L_0$) of the composites was reduced due to the low thermal expansivity of AlN ($4.4 \times 10^{-6}/K$) compared to Al ($23.6 \times 10^{-6}/K$). The two composites containing precipitated Si in matrix showed reduction in slope of $\Delta L/L_0$ curve after 573 K. The decrease in the slope is attributed to the increment of solid solubility of Si in Al with increasing temperature; 0.05 at.% at 523 K, 0.29 at.% at 673 K, 0.77 at.% at 773 K. Since the atomic volume of Si is bigger than that of Al, the dissolution of Si in Al can reduce the thermal expansion of the Al(Si) matrix at elevated temperature [61]. **Figure 4.8(b)** shows the calculated coefficient of thermal expansion (CTE) values as a function of temperature with pure Al and in-situ Al-AlN particulate composites. CTE can be estimated as follows;

$$\text{CTE} = \frac{1}{L_0} \frac{(L-L_0)}{(T-T_0)} \quad (4.5)$$

where T_0 indicates room temperature (RT) and L_0 is initial length of specimens at RT. Unlike Al and Al-AlN particulate composites that showed gradual increase in CTE with increasing temperature, the two composites showed maximum value of CTE at 623 K and reduction of CTE after 623 K, which is similar to the thermal expansion behavior of Si-containing AMCs [61, 73]. The composites AS73, with high volume fraction of nitride phase, retained its low CTE at the whole temperature range, which can be promising for base plate materials subjected to the elevated temperature.

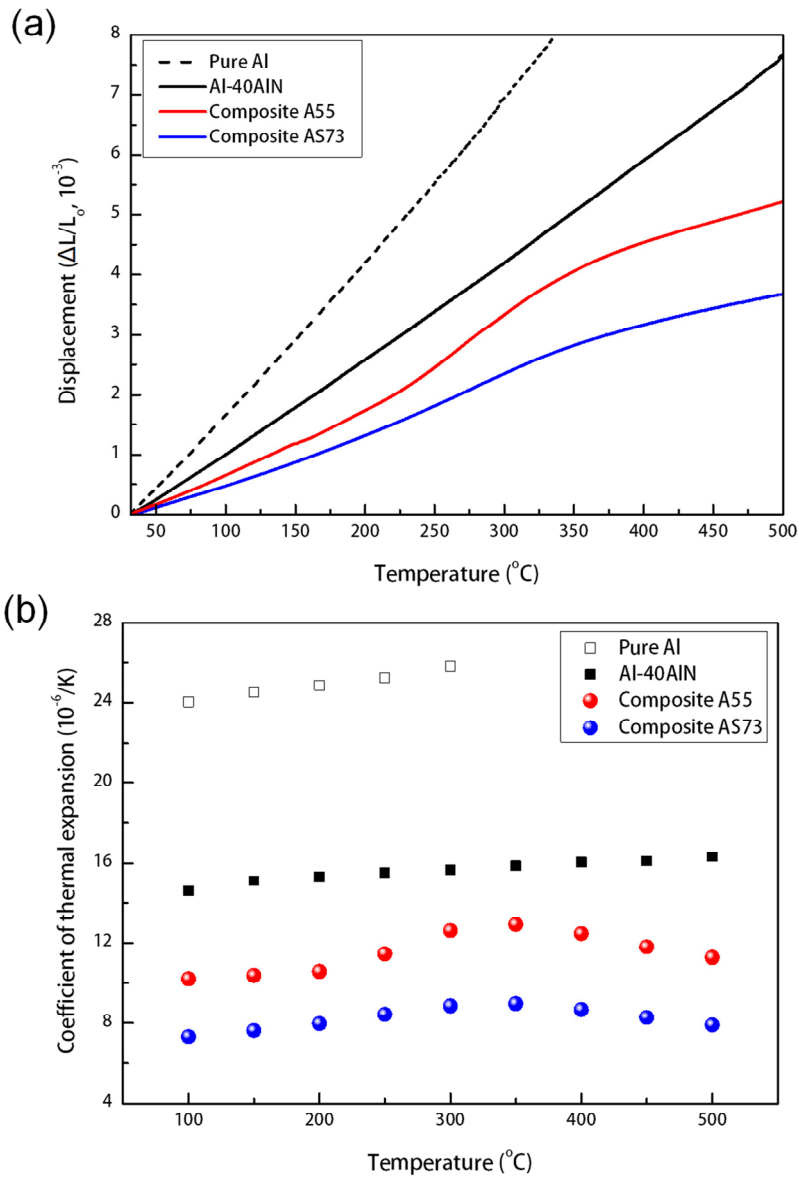


Figure 4.8 (a) Thermal expansion behavior and (b) CTE of the developed Al-Si-AlN-(Si_3N_4) composites compared with that of pure Al and particulate Al-AlN composites.

Figure 4.9 shows the CTE values as a function of volume fraction of nitride phase with various Al-AlN particulate composites. CTE values of the present composites A55 and AS73 were $10.2 \times 10^{-6}/\text{K}$ and $7.33 \times 10^{-6}/\text{K}$, respectively. Unlike Kerner's model where CTE of various Al-AlN particulate composites followed, CTE of the two composites were about 20 % deviated from Kerner's model. The deviation can be explained by the interpenetrating structure that exhibits little thermal expansion by Al matrix due to the rigidity of interconnected ceramic phase [61]. Moreover, the CTE of the composites can be affected by the precipitated Si with low CTE ($2.2 \times 10^{-6}/\text{K}$). Therefore, the interpenetrating structure formed by aggregation of fine AlN particles and Si phase formed by the in-situ reaction induce additional constraint for the expansion of Al matrix, which rationalizes CTE deviation of composites from Kerner's model.

Figure 4.10 shows the relationship between thermal conductivity and CTE of the present Al-Si-AlN-(Si₃N₄) composites compared with previously reported in-situ formed Al-AlN composites [38, 74]. Since AlN shows high thermal conductivity (200 W/m·K) as well as low CTE, it is expected that the Al/AlN particulate composites show high thermal conductivity with enhanced dimensional stability, which is suitable for thermal management of high-power electronics [32]. The present composites A55 and AS73 showed reasonable thermal conductivity, 59.5 W/m·K and 72.1 W/m·K, respectively. The significant deviation of thermal conductivity compared to the estimated value by rule of mixture may result from that the structure of AlN reinforcements in the present composites is fine for the efficient thermal conduction of electron and phonon. The H-J model [49] indicated that the increase in V_p and the decrease in size of reinforcements result in the reduction of thermal conductivity of composite materials due to the increased interfacial area that scatters electrons and phonons. The higher thermal conductivity in the composite AS73 than the composite

A55 seems to be abnormal according to the H-J model. It can be understood that the composite AS73 showed higher AlN interspacing compared with the composites A55 [Figure 4(b) and 5(b)], which provides to the more efficient thermal conduction path for both electrons and phonons. Thus, in the present composites, the size and composition of bimodal powder mixture should be optimized for the improvement of thermal conductivity as well as dimension stability.

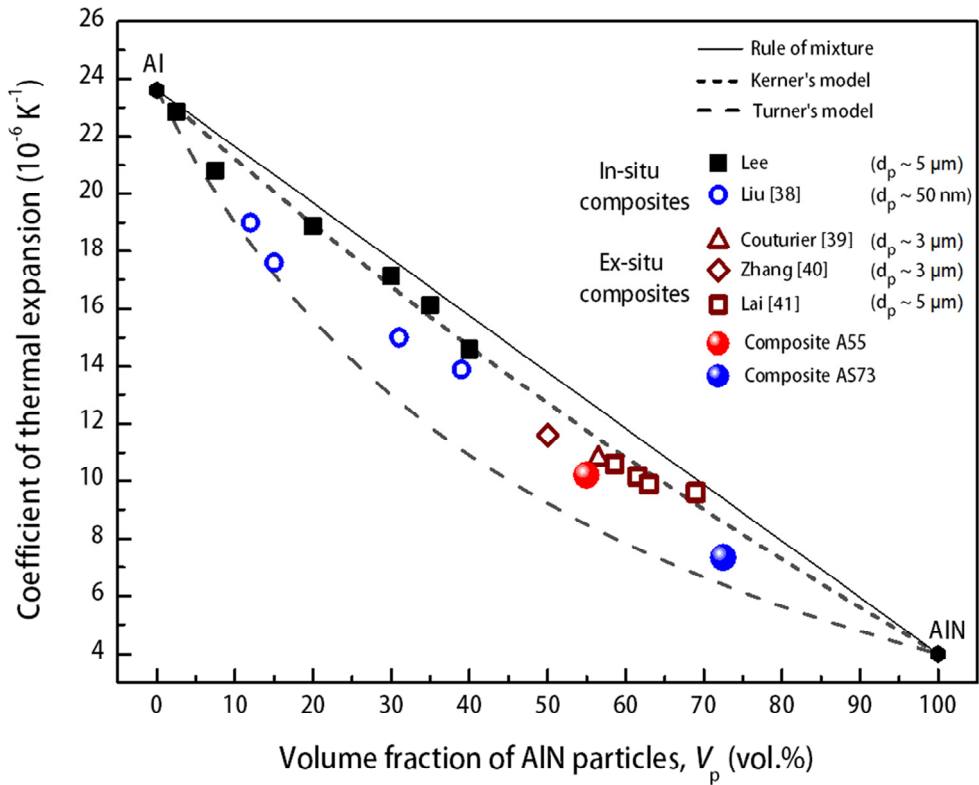


Figure 4.9 CTE of the developed Al-Si-AlN-(Si_3N_4) composites compared with that of various reported Al-AlN composites and theoretically predicted values [38-41].

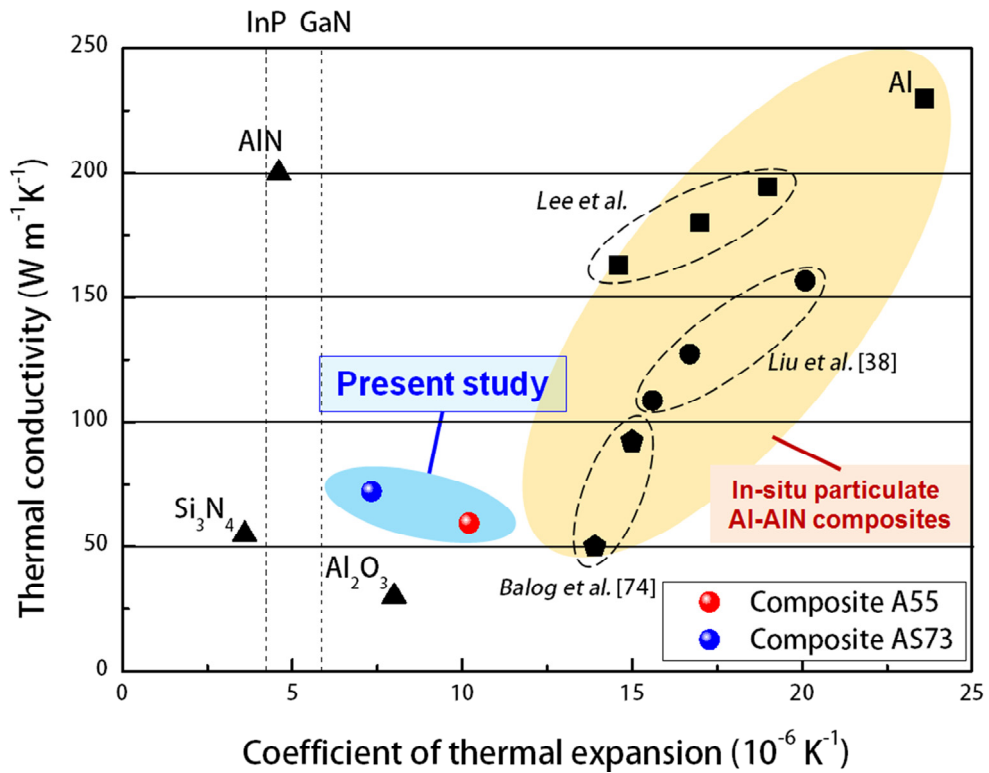


Figure 4.10 Correlation between thermal conductivity and CTE of the present Al-Si-AlN-(Si₃N₄) composites compared with various in-situ Al-AlN composites [38, 74].

4.2.5. Mechanical properties

A list of density, thermal properties and mechanical properties is shown in **Table 4.1**. Compared with unreinforced pure Al, the present composites A55 and AS73 exhibited improved flexural strength. However, the effect of strengthening on the present composites was unsatisfactory since the in-situ formation of AlN from Si_3N_4 is unfavorable for the enhancement of mechanical properties [75, 76]. It should be noted that in case of the present composite AS73, the strength value (305.5 MPa) is higher than the estimated value (269 MPa) from rule of mixture of Al and AlN. This means that the presence of unreacted Si_3N_4 phase in the in-situ composites may be desirable to retain the strength. Thus, the optimization of phase constitution as well as the size and composition of bimodal powder mixture would be effective for the improvement of mechanical properties as well as thermal properties as discussed in **section 4.2.4**.

Table 4.1 Density, thermal and mechanical properties of pure Al, Al-Si-AlN-(Si₃N₄) composites, AlN and Si₃N₄ ceramics [75, 76].

	Al	A55	AS73	AlN	Si ₃ N ₄
Density (g/cm ³)	2.70	3.01	3.13	3.30	3.20
CTE (10 ⁻⁶ /K)	23.6	10.2	7.33	4.4	3.6
Thermal conductivity (W/m·K)	230	59.5	72.1	200	30-55
Flexural strength (MPa)	50	203.9	305.5	350	941
Fracture toughness (MPa·m ^{0.5})	> 40	6.68	5.63	3-4	9.4

4.3. Conclusions

The present study shows the in-situ synthesis of AMCs with high volume fraction of AlN and Si₃N₄ by APADR process. During arc melting, the Al melt simultaneously infiltrated the preform and reacted with Si₃N₄, which was accelerated by high temperature of arc plasma and exothermic heat released from the in-situ reaction. The capillary pressure for pressureless infiltration of Al melts through Si₃N₄ powder preform was estimated to over than 1.0 MPa that is high enough to infiltrate the preform prepared by compacting fine ceramic particles. The interpenetrating structure of fine AlN particles was achieved by aggregation of fine Si₃N₄ particles during compaction, sintering by high temperature and volume expansion of nitride phase that was predicted by considering molar volume ratio between Si₃N₄ and AlN. The resulting composites showed more reduced CTE compared to Kerner's model, indicating the CTE of the composites was affected by their microstructure as well as volume fraction of nitride phase. These results give us a guideline on how to design composites with high volume fraction of ceramic phase for improving dimensional stability.

CHAPTER 5

In-situ synthesis of ZrN reinforced bulk metallic glass matrix composites by arc plasma-induced accelerated displacement reaction

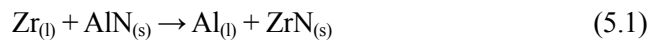
5.1. Introduction

Bulk metallic glasses (BMGs) have attracted considerable attention due to their promising properties such as extremely high strength, low Young's modulus and excellent corrosion resistance that are different from those of conventional crystalline alloys [77]. However, BMGs confront a challenging problem that they exhibit brittle fracture by the formation of localized shear bands [78]. Thus, metallic glass matrix composite materials containing secondary crystalline phases have been investigated to improve ductility of the BMGs [8, 9, 79, 80].

Among the various metallic glass matrix composites, ceramic particulate reinforced BMG composites have been developed to improve their mechanical properties such as fracture strength or ductility [81-85]. Yim et al [8] reported the synthesis of BMG matrix composites reinforced with SiC, WC or TiC particles by pressure infiltration process. The volume fraction of secondary phase was variable

from 10 vol.% to 30 vol.%, and the BMG composites with 10 vol.% of SiC or WC showed improved compressive ductility compared with the monolithic BMGs. [86]. However, the interfacial reaction between SiC and Zr during the melt infiltration process resulted in the formation of interfacial compound and voids, which degrades mechanical properties of composite materials in general [86]. Furthermore, the monolithic BMG and BMG composites showed a deviation in glass transition and crystallization temperature since the interfacial reaction altered matrix composition, which indicates that the undesirable reaction may lead to the degradation of thermal stability in BMG matrix [87].

Over the past decades, the in-situ formation of reinforcements in BMG melt has been investigated to fabricate the composites with strong interfacial bonding without the degradation of thermal stability and mechanical properties. Recently, ZrN reinforced BMG composites were fabricated by mixing BMG powder with AlN powder to prepare powder mixtures that was then compacted, melted and cast by copper-mold casting process [83]. According to the temperature dependence of standard free energies of the various nitrides (**Figure 5.1**) [62], the formation of ZrN is thermodynamically favorable as follows:



where Al diffuses out of AlN and dissolves in Zr-based BMG melt during melting. The processing of powder mixtures composed of AlN and Zr BMG resulted in the formation of pores in the cast specimens [83]. The pores in BMGs might improve the plasticity of the BMGs by the formation of multiple shear bands and the prevention of propagation of a localized shear band at the periphery. However, the role of pores for the mechanical properties in BMGs is complex since the pores may act for the stress concentration site to initiate the propagation of localized shear bands.

In the present study, we report the in-situ formation of ZrN reinforced Zr-based BMG composites by arc plasma-induced accelerated displacement reaction (APADR) between AlN particulates and Zr BMG. As a sacrificial reactant, particulate Al-AlN composites were melted with the constituent elements of Zr BMGs. In APADR process, the AlN particles were homogeneously dispersed in the BMG melt, and the ZrN was synthesized by the reaction of AlN and Zr during arc melting, which is thermodynamically favorable as shown in **Figure 5.1**.

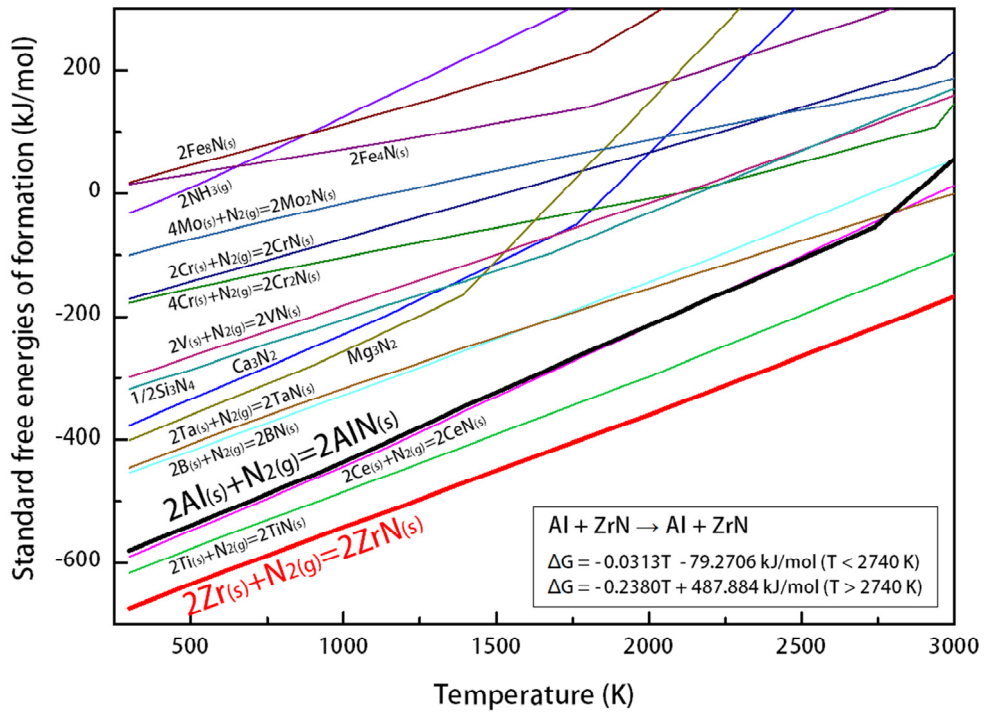


Figure 5.1 The standard free energies of the nitride ceramics as a function of temperature [62], which shows that ZrN is thermodynamically more stable than AlN at the whole temperature range.

5.2. Results and discussion

The master alloys of $Zr_{46}Cu_{30.14}Ag_{8.36}Al_8Be_{7.5}$, which shows the highest glass forming ability among the previously reported Zr based BMGs [88], were fabricated by arc melting pure elements of Zr, Ag, Al and Cu-4wt.%Be ($Cu_{77.3}Be_{22.7}$) alloy under Ar atmosphere. On the other hands, the ZrN reinforced $Zr_{46}Cu_{30.14}Ag_{8.36}Al_8Be_{7.5}$ matrix composite ingots were prepared by melting ZrCuAgBe master alloys, Al-40vol.% AlN particulate composites (average diameter: 5 μ m) and extra Zr together (**Figure 5.2**), which resulted in the formation of $Zr_{46}Cu_{30.14}Ag_{8.36}Al_8Be_{7.5}$ BMG/ZrN (Zr BMG/ZrN) composites. During arc melting, the AlN in the starting materials reacted with Zr in the melt and was transformed into ZrN since the in-situ reaction is thermodynamically favorable at the whole temperature range (**Figure 5.1**) [62]. The maximum volume fraction of ZrN particulates in the resulting composites was estimated as 4 vol.%. The amount of extra Zr, which is necessary for the maintenance of matrix composition to high glass-forming ability, was carefully calculated based on the total weight of AlN in Al-AlN composites and Al necessary for the preparation of master alloy with the composition of high glass-forming ability.

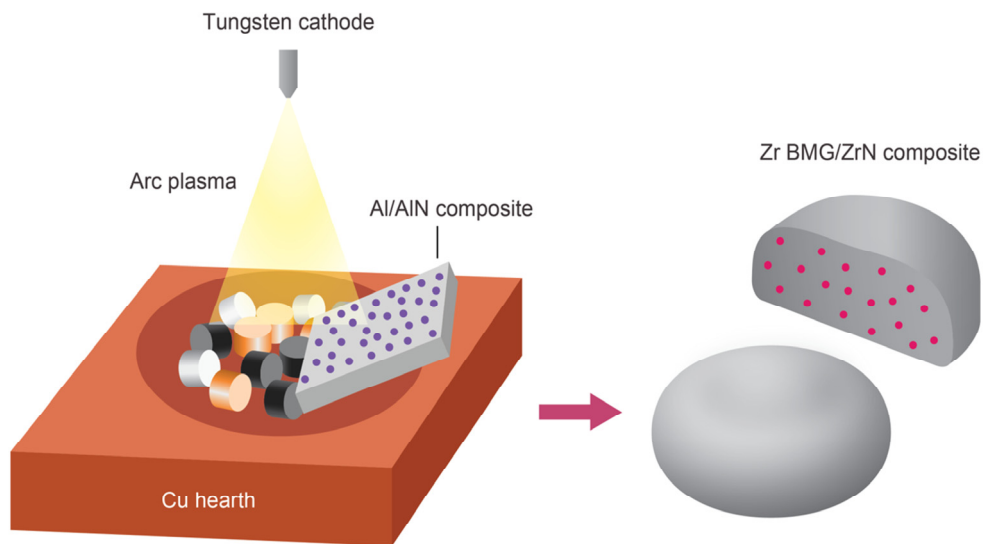


Figure 5.2 Schematic diagram showing processing procedure for the fabrication of Zr BMG/ZrN composites via APADR process.

5.2.1. Microstructures

The XRD patterns of the suction-cast Zr BMG/ZrN composites with diameter from 1 mm to 5 mm are presented in **Figure 5.3**. The composites with diameter up to 4 mm showed a typical broad diffraction maximum of the monolithic BMG and the crystalline peaks of fcc-ZrN phase. Despite increasing the diameter, the Zr BMG/ZrN composites retained their amorphous matrix without any crystalline peaks due to high glass-forming ability of the BMG that suppress the nucleation of any crystallites [88]. The partial crystallization of matrix in BMG rods with diameter of 5 mm may result from the delayed cooling of the glass-forming melt during suction-cast since the ceramic particulates embedded in the melt commonly show slow cooling compared with the melt.

In **Figure 5.4**, DSC curves of the ribbon specimens of the monolithic BMG and Zr BMG/ZrN composites were presented. The composites retained amorphous structure without the change in the enthalpy of crystallization (ΔH_{crys}), but showed the decrease in T_x about 10 K compared with the monolithic BMG. The slight change in characteristic temperature may result from the compositional change in the alloy matrix due to the incomplete displacement reaction between AlN and Zr. The liquid phase displacement reaction between the molten alloys and ceramic reinforcements can result in the liquid metal penetration (See **section 1.2.3.3**) or the formation of protective ceramic layer that is thermodynamically more stable (See **section 4.2.3**). Based on the calculation of Pilling-Bedworth Ratio (PBR) between reactant (AlN) and product (ZrN), the value can be estimated by following equation;

$$\text{PBR} = \frac{b}{a} \times \frac{w_{\text{ZrN}} \rho_{\text{AlN}}}{w_{\text{AlN}} \rho_{\text{ZrN}}} \quad (5.2)$$

where b/a is a coefficient that can be obtained from the stoichiometry of reaction ($\text{Zr} + \text{AlN} = \text{Al} + \text{ZrN}$, b/a is 1 in this reaction), w is molar mass and ρ is density of the

nitrides. The estimated PBR value, 1.20, indicates that the in-situ formation of ZrN leads to the volumetric expansion of nitride reinforcements during the APADR process. Thus, the in-situ reaction could be incomplete and the unreacted AlN may be present in Zr BMG/ZrN composites; thus the matrix composition of Zr BMG can be altered from the estimated composition.

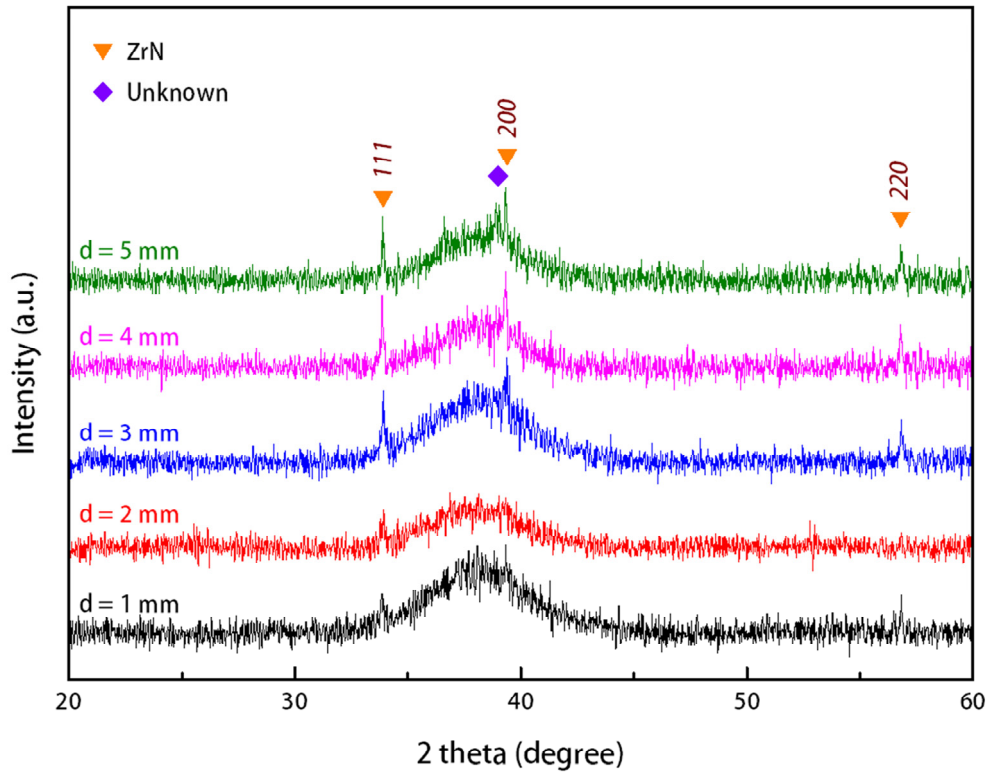


Figure 5.3 XRD patterns of the suction cast Zr BMG/ZrN composites with different diameter from 1 mm to 5 mm.

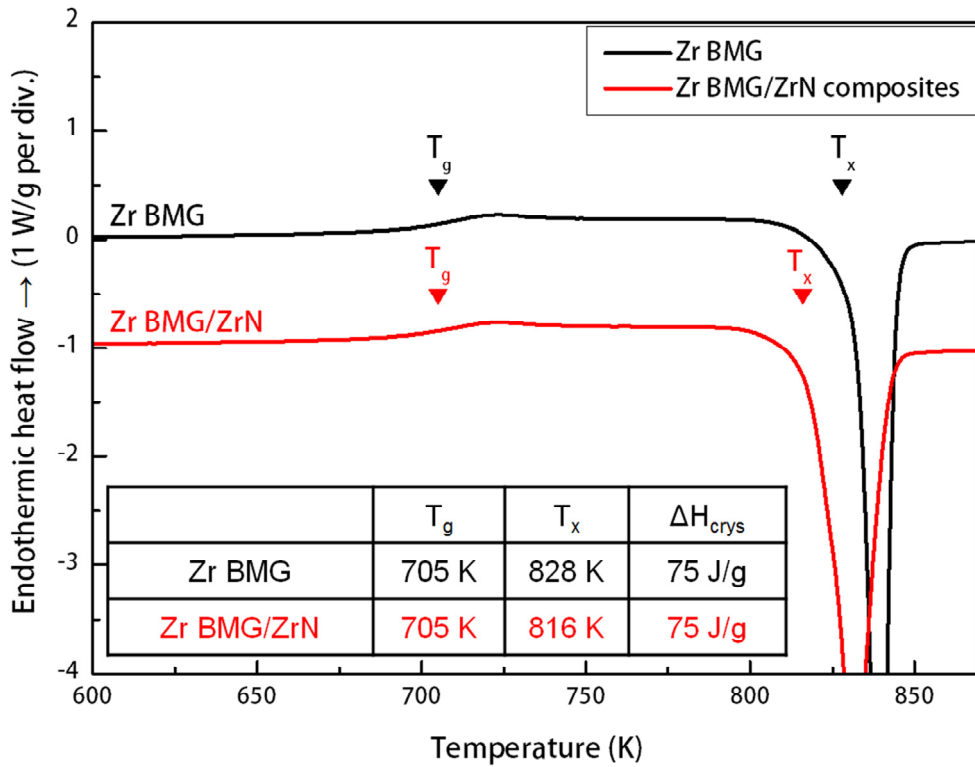


Figure 5.4 DSC curves of the as-spun monolithic BMG and Zr BMG/ZrN composites with a table showing glass transition temperature (T_g), crystallization onset temperature (T_x) and enthalpy of crystallization (ΔH_{crys}).

Figure 5.5 shows the cross-section of the suction-cast Zr BMG/ZrN composites with diameter of 2 mm. The in-situ formed ZrN particulates were uniformly distributed in the matrix. This is different from the composites fabricated by mixing reinforcements with master alloy by arc melting [89], which showed a little agglomeration of particulates in the matrix. The homogeneous dispersion of ZrN is due to the in-situ reaction which improves the wettability between the molten alloys and the products [84, 90] as well as the arc melting that is effective for homogeneous mixing of molten alloys. Comparing with the Zr BMG/ZrN composites prepared by copper mold casting of molten powder mixtures of Zr BMG and AlN [83], the suction-cast Zr BMG/ZrN composites showed few pores or voids in the BMG matrix.

Figure 5.6 shows SEM image of the Zr BMG/ZrN composites. The measured volume fraction of ZrN particles from **Figure 5.5** and **5.6** was about 4 vol.% that was almost similar to the estimated volume fraction from the calculation (See **section 5.2**). The ZrN particles appeared approximately spherical shape, resulting from surface smoothing of ZrN to reduce total free energies during arc melting. The average diameter of the ZrN particles was about 5 μm , which is similar to the size AlN particulates in the sacrificial Al-AlN composites (**Figure 3.5**). The in-situ formed ZrN particles were homogeneously dispersed in the BMG matrix, but the particles appeared to be slightly aggregated and connected to each other. It may result from the high temperature synthesis induced by arc plasma [50], leading to diffusion bonding of the ceramic particles each other.

Figure 5.7 shows high-resolution TEM micrograph and the selected area diffraction patterns of BMG matrix and ZrN phase. The interface between BMG and ZrN was clean and well bonded without any interfacial compounds, which is advantageous for the improvement of mechanical properties of the composites [90].

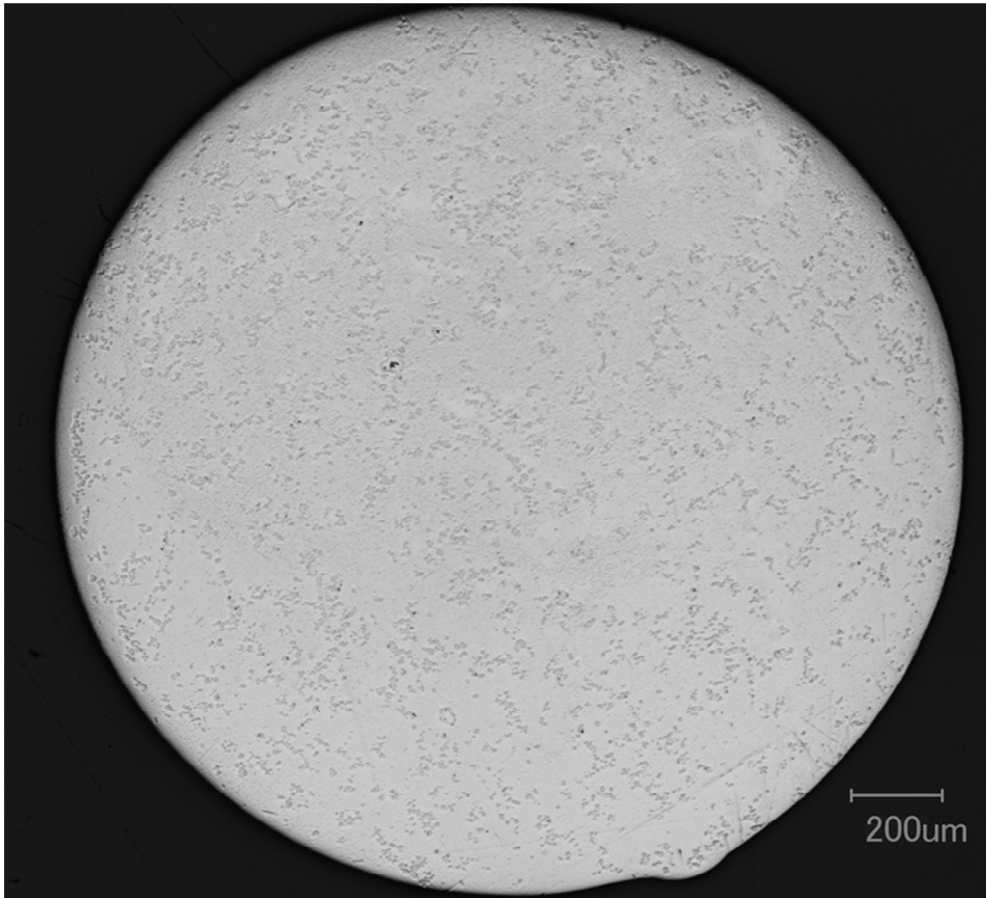


Figure 5.5 A cross-section image of suction-cast Zr BMG/ZrN composites with a diameter of 2 mm.

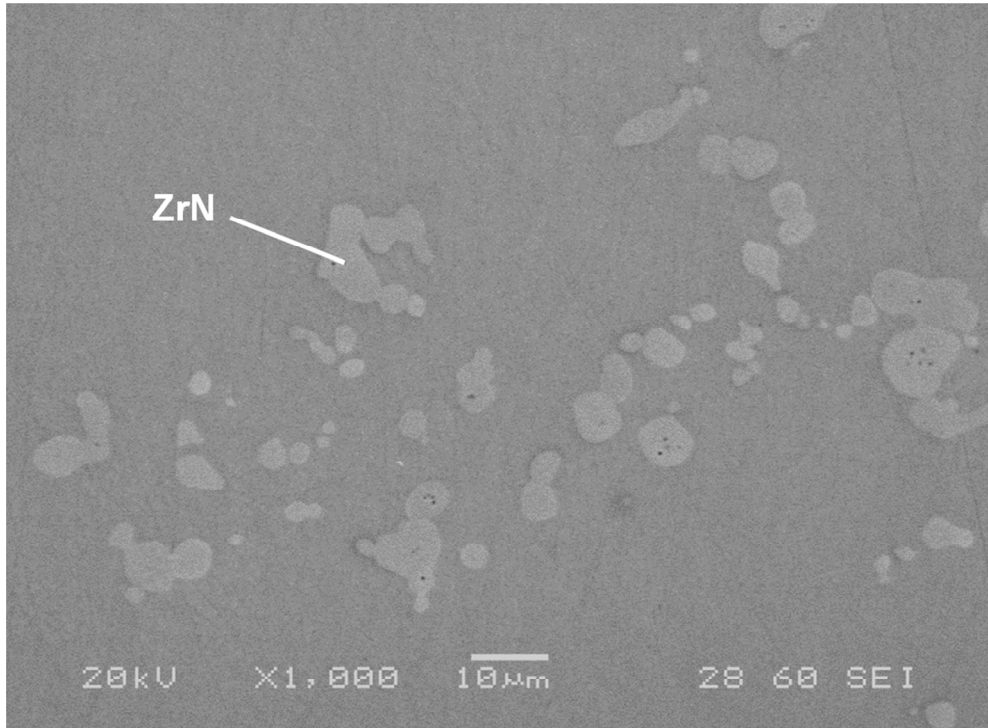


Figure 5.6 SEM micrograph of suction-cast Zr BMG/ZrN composites with a diameter of 2 mm.

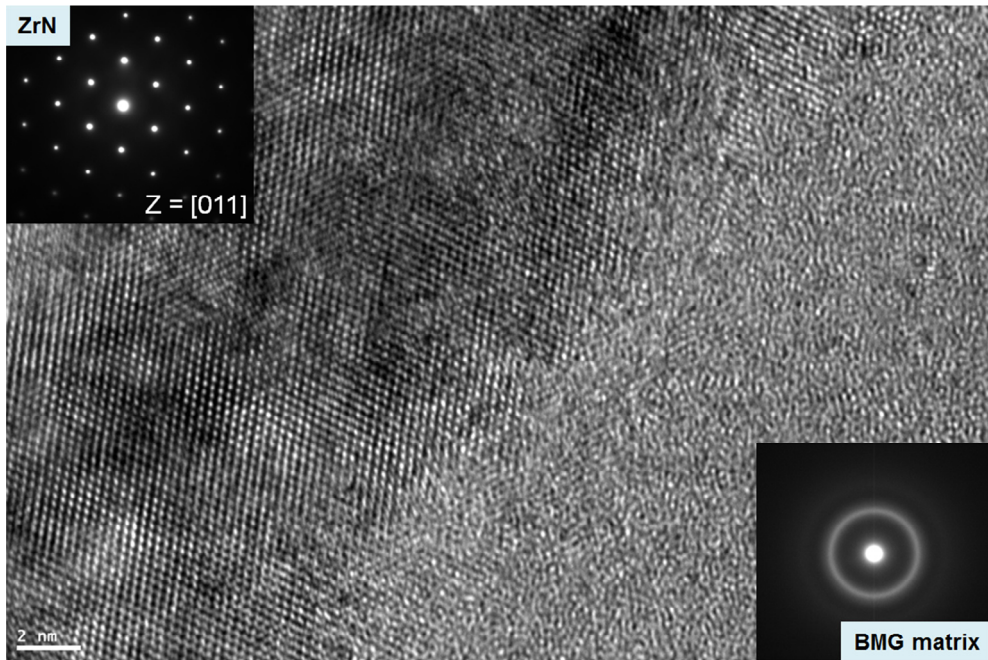


Figure 5.7 High-resolution TEM micrograph of suction-cast Zr BMG/ZrN composites with selected area diffraction patterns of BMG matrix and in-situ formed ZrN particulates.

5.2.2. Mechanical properties

Figure 5.8 shows compressive stress-strain curves of the monolithic BMG and the Zr BMG/ZrN composites. The composites showed about 7 % increase in Young's modulus compared with the monolithic BMG due to the higher modulus of ZrN (380 GPa) [91]. The composites exhibited similar yield strength (1800 MPa) compared with the monolithic BMG, but much higher fracture strength (2100 MPa) that is 16.7 % higher than the monolithic BMG (1800 GPa). The strengthening of the composites is attributed to the role of hard phase in BMG matrix that impedes the generation and the propagation of shear bands. The monolithic Zr BMG deformed elastically and fractured without any macroscopic yielding, but compressive plasticity, 2.5 %, was observed in the composites. The improved ductility of the composites may be due to the suppressed propagation of shear bands, the slip transfer from the BMG matrix to the particles and the strong interfacial bonding between the matrix and the reinforcements (**Figure 5.7**). The increasing serrated plastic flow of the composites was observed after yielding, indicating the formation of multiple shear bands during the compressive deformation.

The fracture morphologies of the Zr BMG/ZrN composites are displayed in **Figure 5.9**. **Figure 5.9(a)** shows SEM micrograph of external appearance of the composites. The fracture angle for the composites was about 41° with the stress axis, indicating that the fracture of the composites does not occur along the maximum shear stress plane. **Figure 5.9(b)** exhibits that the vein type morphologies and some molten drops were observed at the fracture surface of the composites, indicating that the composites underwent local softening or melting by the release of high elastic energy. The outer lateral surface of the composites revealed a high density of shear bands, indicating that plastic deformation (2.5 %) occurred before fracture [**Figure 5.9(a)**]

and (c)]. Moreover, the multiple shear bands were shown to be a wavy passing pattern. This indicates that the nucleation and propagation of shear bands are related to the plastic instabilities [92]. The plasticity and strength of hard phase reinforced BMG depend on the compressive strength of the reinforcements and stress partitioning in which the BMG matrix fractured by breaking the reinforcements [93]. **Figure 5.9(d)** shows the failed ZrN particles on the fracture surface, indicating the deformation mechanism of the Zr BMG/ZrN composites was similar to the case of Zr BMG/ZrC composites investigated by synchrotron X-ray diffraction [93].

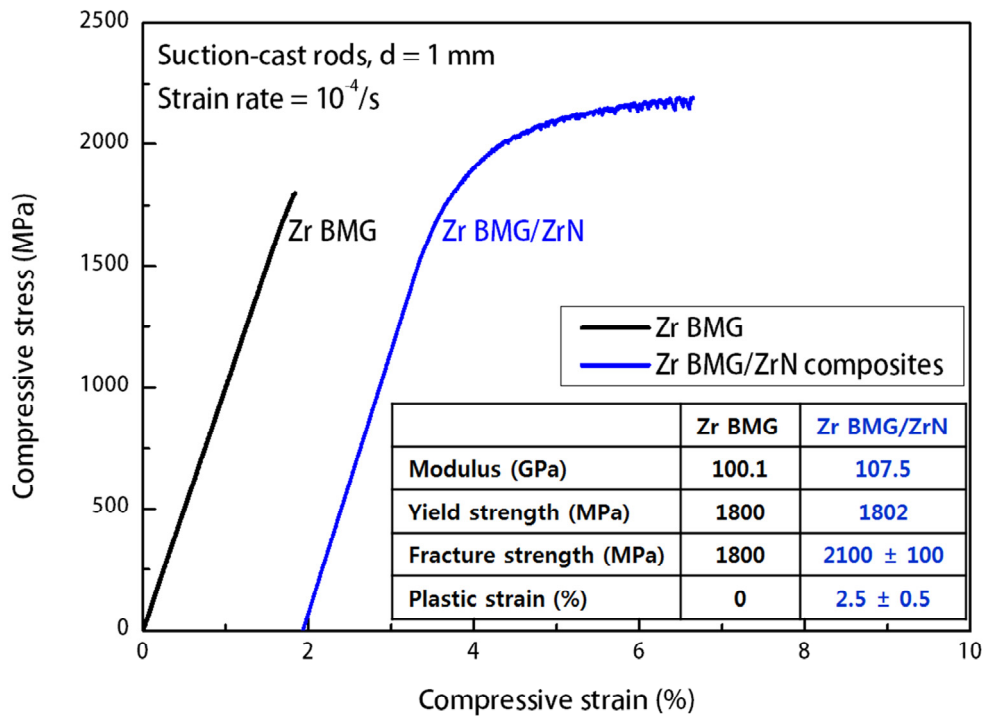


Figure 5.8 Compressive stress-strain curves of the suction-cast monolithic Zr BMG and Zr BMG/ZrN composites with diameter of 1 mm. The inset shows modulus, yield strength, fracture strength and plastic strain of the specimens.

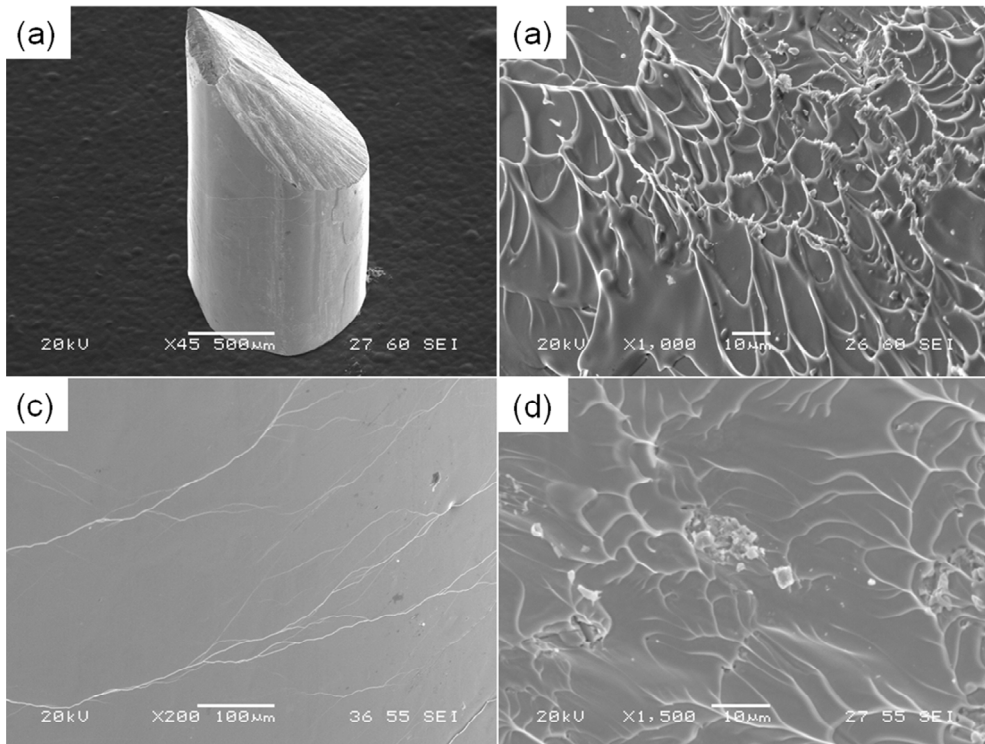


Figure 5.9 Fracture morphologies of suction-cast Zr BMG/ZrN rods with diameter of 1 mm.

5.3. Conclusions

The present study shows the in-situ synthesis of Zr BMG/ZrN composites by APADR process. During arc melting, the AlN particulates embedded in Al-AlN composites were homogeneously dispersed and the AlN was transformed into ZrN in Zr BMG melt, which was accelerated by arc plasma-induced high temperature and the exothermic heat released from the in-situ reaction. The suction-cast composites exhibited improved plasticity compared with the monolithic Zr BMG, resulting from the uniform distribution of ZrN particles that induced the formation of multiple shear bands and prevented the propagation of single shear bands. The increase in strength of the composites was attributed to strong interfacial bonding between the BMG matrix and ZrN particles, which leads to effective load transfer from the matrix to the particles. These results give us the guidelines to fabricate in-situ BMG matrix composites containing Zr and Al as constituent elements wherein the transformation of AlN into ZrN can be achieved by arc plasma processing.

CHAPTER 6

Conclusions

The development of novel metal-ceramic composites was investigated by using arc plasma processing. The arc melting of pure metals and alloys in controlled atmosphere resulted in the volume nitridation, the displacement reaction of metals with sacrificial reactants and the in-situ formation of thermodynamically stable reinforcements in the molten alloys. The arc plasma processing accelerated the chemical reaction between the melt and gaseous or solid reagents that requires high processing temperature and long processing time in the conventional in-situ processing routes. The arc plasma-induced reaction, which showed significant exothermic heat, was very reactive, but it does not degrade the mechanical or thermal properties since the products exhibit clean and strong interfacial bonding. Since the arc melting of alloys involved liquid-state processing under inert atmosphere composed of argon and/or nitrogen gas, any contamination or oxidation of the raw materials is unexpected in arc plasma processing.

The in-situ synthesis of Al-AlN composites with attractive thermal properties was feasible via arc plasma-induced accelerated volume nitridation (APAVN) process. APAVN of Al resulted from instantaneous chemisorption of dissociated nitrogen, enhanced diffusion of the dissolved nitrogen in Al melt and improved wettability

caused by arc plasma-induced high temperature and electrowetting effect. These led to higher AlN formation of $\sim 2.94 \times 10^{-1} \text{ g/min}\cdot\text{cm}^3$, about 400 times higher than that in gas bubbling method ($6.91 \times 10^{-4} \text{ g/min}\cdot\text{cm}^3$). Within a few minutes of repeated APAVN process under Ar/N₂ mixture atmosphere, volume fraction of AlN increased up to 40 vol.%, which is the highest value ever reported by nitridation of pure Al melt using N₂ gas. The Al matrix composites contained homogeneously dispersed AlN particulates with strong interfacial bonding and low ITR, which results in unique combination of relatively low CTE ($14.6 \times 10^{-6} \text{ K}^{-1}$) and high TC (163 W/m·K). The accelerated nitridation of Al melt gives us a guideline on how to design a simple process for continuous production of in-situ Al-AlN composite sheets with tailor-made thermal properties for heat sink applications.

The in-situ synthesis of Al matrix composites with high volume fraction of nitride reinforcements was feasible by arc plasma-induced accelerated displacement reaction (APADR) process. APADR resulted in the pressureless infiltration of Al melt into the powder preforms and the in-situ reaction of the melt with Si₃N₄ in a minute. The infiltration and reaction can be accelerated by arc plasma-induced high temperature and exothermic heat released from the in-situ reaction, which leads to the formation of thick and dense AlN products. The capillary pressure for the spontaneous infiltration of Al melts through Si₃N₄ preform was estimated to over than 1.0 MPa that is high enough to infiltrate the preforms with high volume fraction of ceramic particles. The interpenetrating structure composed of relatively fine AlN was achieved by sintering of aggregated fine nitride ceramics during arc melting. Volume expansion of secondary phases from the displacement reaction was observed in the resulting composites, which was coincident to the estimation calculated by considering molar

volume ratio between Si_3N_4 and AlN . These results give us a guideline on how to design Al matrix composites with improved dimensional stability.

The in-situ synthesis of ZrN reinforced composites was feasible by APADR process where Zr BMG instead of pure Al was applied as matrix. APADR resulted in the homogeneous dispersion of nitride ceramics and the transformation of AlN into ZrN in Zr BMG melt, which was accelerated by arc plasma-induced high temperature and the exothermic heat released from the in-situ reaction. The suction cast composites exhibited improved mechanical properties compared with the monolithic Zr BMGs, resulting from the uniform distribution of in-situ formed ZrN particulates that induced the formation of multiple shear bands and prevented the propagation of localized shear bands. The strong interfacial bonding between the BMG matrix and ZrN particles resulted in the increase of fracture strength, indicating the effective load transfer from the matrix to the ZrN hard phase. These results give us the guidelines to fabricate multi-component alloy matrix composites containing Zr and Al as constituent elements wherein the transformation of AlN into ZrN can be accomplished by arc plasma processing.

Figure 6.1 shows various processing routes for the development of composite materials with respect to processing temperature. Among the processes, arc plasma processing utilized high temperature close to boiling point where in-situ reactions such as volume nitridation or displacement reaction were significantly accelerated. Although arc plasma-induced reaction were confined to nitride reinforcements and Al and BMG matrix in this study, a wide range of combinations of reactants and products shown in **Figure 6.1** encourage us to enlarge the applicability of the processing, which would expand the research area of arc plasma processing routes for the development of novel metal-ceramic composites.

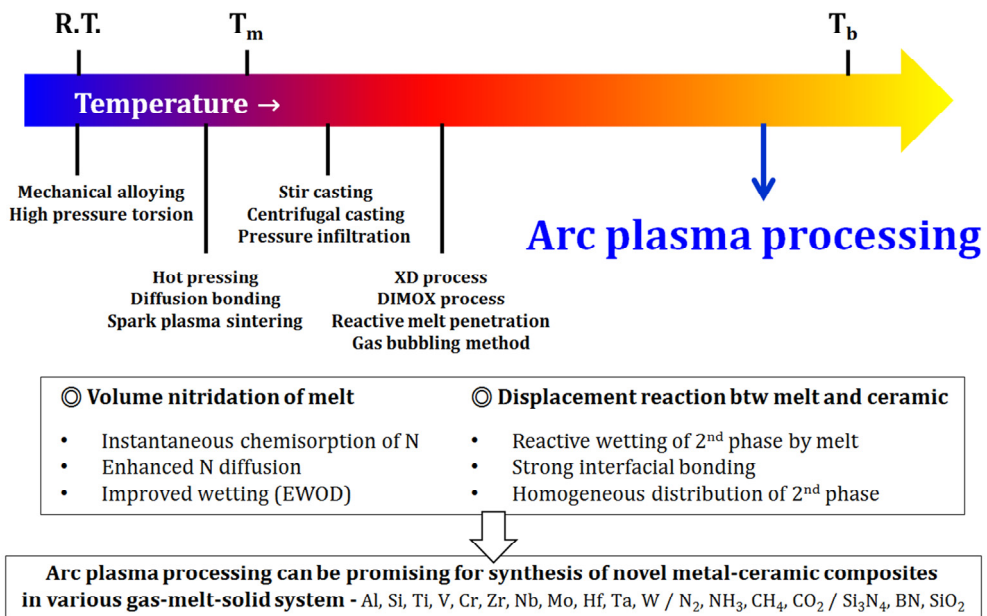


Figure 6.1 Processing routes for synthesis of composite materials with respect to processing temperature, and advantages of the arc plasma processing route for the fabrication of novel metal-ceramic composites.

Reference

- [1] M. Ashby, Y. Brechet, *Acta Mater.*, 51 (2003) 5801-5821.
- [2] K.K. Chawla, *Metal matrix composites*, Wiley Online Library, 2006.
- [3] D. Hull, T. Clyne, *An introduction to composite materials*, Cambridge university press, 1996.
- [4] D.B. Miracle, *Compos. Sci. Technol.*, 65 (2005) 2526-2540.
- [5] I. Polmear, D.S. John, *Light alloys: from traditional alloys to nanocrystals*, Butterworth-Heinemann, 2005.
- [6] M. Occhionero, R. Adams, K. Fennessy, *Proceedings of the Forth Annual Portable by Design Conference, Electronics Design*, 1997, pp. 24-27.
- [7] A. Miserez, R. Müller, A. Rossoll, L. Weber, A. Mortensen, *Mater. Sci. Eng. A*, 387 (2004) 822-831.
- [8] H. Choi-Yim, W.L. Johnson, *Appl. Phys. Lett.*, 71 (1997) 3808-3810.
- [9] C. Hays, C. Kim, W.L. Johnson, *Physical Review Letters*, 84 (2000) 2901.
- [10] J.E. Allison, G.S. Cole, *JoM*, 45 (1993) 19-24.
- [11] Y. Nishida, *Introduction to Metal Matrix Composites: Fabrication and Recycling*, Springer Science & Business Media, 2013.
- [12] J. Torralba, C. Da Costa, F. Velasco, *J. Mater. Proc. Technol.*, 133 (2003) 203-206.
- [13] J. Lee, H. Kim, T. Kim, Y. Kim, J. Bae, *J. Alloys Compd.*, 434 (2007) 336-339.
- [14] C. Suryanarayana, *Progress in materials science*, 46 (2001) 1-184.
- [15] A.P. Zhilyaev, T.G. Langdon, *Progress in Materials Science*, 53 (2008) 893-979.
- [16] M. Kawasaki, *J. Mater. Sci.*, 49 (2014) 18-34.
- [17] T. Tokunaga, K. Kaneko, Z. Horita, *Mater. Sci. Eng. A*, 490 (2008) 300-304.
- [18] R. Saha, E. Morris, N. Chawla, S. Pickard, *Journal of materials science letters*, 21 (2002) 337-339.

- [19] R. Hebert, J. Perepezko, H. Rösner, G. Wilde, *Scripta Mater.*, 54 (2006) 25-29.
- [20] J. Molina, R. Saravanan, R. Arpón, C. Garcia-Cordovilla, E. Louis, J. Narciso, *Acta Mater.*, 50 (2002) 247-257.
- [21] S. Li, D. Xiong, M. Liu, S. Bai, X. Zhao, *Ceramics International*, 40 (2014) 7539-7544.
- [22] S. Ray, *J. Mater. Sci.*, 28 (1993) 5397-5413.
- [23] D.G. Thomas, *Journal of Colloid Science*, 20 (1965) 267-277.
- [24] A. Westwood, *Metallurgical Transactions A*, 19 (1988) 749-758.
- [25] B. Daniel, V. Murthy, *Materials & Design*, 16 (1995) 155-161.
- [26] M. Breslin, J. Ringnald, L. Xu, M. Fuller, J. Seeger, G. Daehn, T. Otani, H. Fraser, *Mater. Sci. Eng. A*, 195 (1995) 113-119.
- [27] Q. Hou, R. Mutharasan, M. Koczak, *Mater. Sci. Eng. A*, 195 (1995) 121-129.
- [28] C. Borgonovo, D. Apelian, M. Makhlof, *JOM*, 63 (2011) 57-64.
- [29] Q. Zheng, R.G. Reddy, *Metallurgical and Materials Transactions B*, 34 (2003) 793-804.
- [30] Q. Zheng, B. Wu, R.G. Reddy, *Adv. Eng. Mater.*, 5 (2003) 167-172.
- [31] E. Munch, M.E. Launey, D.H. Alsem, E. Saiz, A.P. Tomsia, R.O. Ritchie, *Science*, 322 (2008) 1516-1520.
- [32] C. Zweben, *Jom*, 50 (1998) 47-51.
- [33] P. Li, E. Kandalova, V. Nikitin, A. Makarenko, A. Luts, Z. Yanfei, *Scripta Mater.*, 49 (2003) 699-703.
- [34] M.S. Newkirk, A. Urquhart, H. Zwicker, E. Breval, *J. Mater. Res.*, 1 (1986) 81-89.
- [35] H. Scholz, P. Greil, *J. Mater. Sci.*, 26 (1991) 669-677.
- [36] Q. Zheng, R. Reddy, *J. Mater. Sci.*, 39 (2004) 141-149.
- [37] S.S. Kumari, U. Pillai, B. Pai, *J. Alloys Compd.*, 509 (2011) 2503-2509.
- [38] Y.Q. Liu, H. Cong, H. Cheng, *J. Mater. Res.*, 24 (2009) 24-31.
- [39] R. Couturier, D. Ducret, P. Merle, J. Disson, P. Joubert, *J. Eur. Ceram. Soc.*, 17 (1997)

1861-1866.

- [40] Q. Zhang, G. Chen, G. Wu, Z. Xiu, B. Luan, *Materials Letters*, 57 (2003) 1453-1458.
- [41] S.-W. Lai, D. Chung, *J. Mater. Sci.*, 29 (1994) 6181-6198.
- [42] C.Y. Ho, M. Ackerman, K. Wu, S. Oh, T. Havill, *Journal of Physical and Chemical Reference Data*, 7 (1978) 959-1178.
- [43] M. Koczak, M.K. Premkumar, *Jom*, 45 (1993) 44-48.
- [44] K. Etemadi, *Plasma Chem. Plasma Proc.*, 11 (1991) 41-56.
- [45] J.E. Hatch, A. Association, *Aluminum: properties and physical metallurgy*, ASM International, 1984.
- [46] C. Toy, W. Scott, *J. Mater. Sci.*, 32 (1997) 3243-3248.
- [47] G.L. Eesley, A. Elmoursi, N. Patel, *J. Mater. Res.*, 18 (2003) 855-860.
- [48] M. Gui, S.B. Kang, K. Euh, *Scripta Mater.*, 52 (2005) 51-56.
- [49] D.P.H. Hasselman, L.F. Johnson, *J. Compos. Mater.*, 21 (1987) 508-515.
- [50] K. Tanaka, K. Ishizaki, S. Yumoto, T. Egashira, M. Uda, *J. Mater. Sci.*, 22 (1987) 2192-2198.
- [51] J. Lennard-Jones, *Transactions of the Faraday Society*, 28 (1932) 333-359.
- [52] M. Boćkowski, M. Wroblewski, B. Łuczniak, I. Grzegory, *Materials Science in Semiconductor Processing*, 4 (2001) 543-548.
- [53] S.-H. Kim, J.-H. Noh, J.-P. Ahn, J.-C. Lee, H. Kwon, J. Lee, H.R. Yang, K.-B. Lee, *Metallurgical and Materials Transactions A*, 46 (2015) 496-504.
- [54] R. Wagner, W. Ellis, *Appl. Phys. Lett.*, 4 (1964) 89-90.
- [55] C. Liu, Z. Hu, Q. Wu, X. Wang, Y. Chen, H. Sang, J. Zhu, S. Deng, N. Xu, *Journal of the American Chemical Society*, 127 (2005) 1318-1322.
- [56] M. Radwan, M. Bahgat, *J. Mater. Proc. Technol.*, 181 (2007) 99-105.
- [57] H. Moon, S.K. Cho, R.L. Garrell, *J. Appl. Phys.*, 92 (2002) 4080-4087.

- [58] J. Lee, H. Moon, J. Fowler, T. Schoellhammer, C.-J. Kim, *Sensors and Actuators A: Physical*, 95 (2002) 259-268.
- [59] H.A. Wriedt, *Bull. Alloys Phase Diagrams.*, 7 (1986) 329-333.
- [60] R.J. Stevens, A.N. Smith, P.M. Norris, *Journal of Heat Transfer*, 127 (2005) 315-322.
- [61] T. Huber, H.-P. Degischer, G. Lefranc, T. Schmitt, *Compos. Sci. Technol.*, 66 (2006) 2206-2217.
- [62] J.F. Elliott, M. Gleiser, V. Ramakrishna, (1963).
- [63] M. Nicholas, D. Mortimer, L. Jones, R. Crispin, *J. Mater. Sci.*, 25 (1990) 2679-2689.
- [64] M. Naka, M. Kubo, I. Okamoto, *Journal of materials science letters*, 6 (1987) 965-966.
- [65] J. Li, H. Hausner, *Materials Letters*, 14 (1992) 329-332.
- [66] S.-r. Wang, Y.-z. Wang, Y. Wang, H.-r. Geng, Q. Chi, *J. Mater. Sci.*, 42 (2007) 7812-7818.
- [67] N. Claussen, P. Beyer, R. Janssen, M. May, T. Selchert, J. Yang, T. Ohji, S. Kanzaki, A. Yamakawa, *Adv. Eng. Mater.*, 4 (2002) 117-119.
- [68] L. Peng, K. Han, J. Cao, K. Noda, *Journal of materials science letters*, 22 (2003) 279-282.
- [69] L. Bowen, R.J. Weston, T. Carruthers, R. Brook, *J. Mater. Sci.*, 13 (1978) 341-350.
- [70] D.R. Clarke, *Journal of the American Ceramic Society*, 75 (1992) 739-758.
- [71] M. Pech-Canul, R. Katz, M. Makhoulouf, *J. Mater. Proc. Technol.*, 108 (2000) 68-77.
- [72] E. Saiz, S. Foppiano, W. MoberlyChan, A. Tomsia, *Composites Part A: applied science and manufacturing*, 30 (1999) 399-403.
- [73] Q. Zhang, G. Wu, L. Jiang, G. Chen, *Materials Chemistry and Physics*, 82 (2003) 780-785.
- [74] M. Balog, P. Yu, M. Qian, M. Behulova, P. Svec, R. Cicka, *Mater. Sci. Eng. A*, 562 (2013) 190-195.
- [75] W. Werdecker, F. Aldinger, *Components, Hybrids, and Manufacturing Technology*, *IEEE Transactions on*, 7 (1984) 399-404.
- [76] M. Fukuhara, K. Fukazawa, A. Fukawa, *Wear*, 102 (1985) 195-210.

- [77] C. Suryanarayana, A. Inoue, Bulk metallic glasses, CRC Press, 2010.
- [78] A. Inoue, *Acta Mater.*, 48 (2000) 279-306.
- [79] D.C. Hofmann, J.-Y. Suh, A. Wiest, G. Duan, M.-L. Lind, M.D. Demetriou, W.L. Johnson, *Nature*, 451 (2008) 1085-1089.
- [80] Y. Wu, Y. Xiao, G. Chen, C.T. Liu, Z. Lu, *Advanced Materials*, 22 (2010) 2770-2773.
- [81] T. Liu, P. Shen, F. Qiu, T. Zhang, Q. Jiang, *Adv. Eng. Mater.*, 11 (2009) 392-398.
- [82] T. Liu, P. Shen, F. Qiu, Z. Yin, Q. Lin, Q. Jiang, T. Zhang, *Scripta Mater.*, 60 (2009) 84-87.
- [83] M. Hasegawa, D. Nagata, T. Wada, A. Inoue, *Acta Mater.*, 54 (2006) 3221-3226.
- [84] H. Kato, T. Hirano, A. Matsuo, Y. Kawamura, A. Inoue, *Scripta Mater.*, 43 (2000) 503-507.
- [85] Y.-K. Xu, H. Ma, J. Xu, E. Ma, *Acta Mater.*, 53 (2005) 1857-1866.
- [86] H. Choi-Yim, R. Busch, U. Köster, W. Johnson, *Acta Mater.*, 47 (1999) 2455-2462.
- [87] H. Choi-Yim, R. Conner, F. Szuecs, W. Johnson, *Acta Mater.*, 50 (2002) 2737-2745.
- [88] H. Lou, X. Wang, F. Xu, S. Ding, Q. Cao, K. Hono, J. Jiang, *Appl. Phys. Lett.*, 99 (2011) 051910.
- [89] H. Kato, A. Inoue, *Materials Transactions, JIM*, 38 (1997) 793-800.
- [90] S.C. Tjong, Z. Ma, *Mater. Sci. Eng. R*, 29 (2000) 49-113.
- [91] N. Alexandre, M. Desmaison-Brut, F. Valin, M. Boncoeur, *J. Mater. Sci.*, 28 (1993) 2385-2390.
- [92] E. Park, H. Chang, J. Lee, D. Kim, *J. Mater. Res.*, 22 (2007) 3440-3447.
- [93] H. Suzuki, J. Saida, T. Shobu, J. Katsuyama, H. Kato, M. Imafuku, S. Sato, *Scripta Mater.*, 66 (2012) 801-804.

요약(국문초록)

제조 환경 및 공정 조건에 따라 물리적 특성이 상이하게 변화하는 금속-세라믹 복합재료의 개발 및 산업현장 또는 극한환경으로의 적용을 위해, 합금기지 조성과 강화상의 적절한 조합을 통한 복합재료의 설계, 결함 제거 및 수율 향상을 위한 제조공정의 최적화 그리고 원료비용 및 공정비용을 낮추기 위한 신 공정 개발에 대한 연구가 활발하게 이루어지고 있다. 금속-세라믹 복합소재의 대표적 제조방법 중 하나인 액상공정은 금속/세라믹 분말을 혼합하여 소결하는 분말야금법과 비교했을 때 상대적으로 공정이 간단하고 원료비용이 저렴하다는 장점이 있으나, 용탕과 세라믹 입자간의 큰 반응성에 의해 공정 도중에 재료의 특성을 저하시키는 계면결합물이 쉽게 형성되는 것으로 알려져 있다. 이러한 액상공정의 단점을 해결하기 위해 재료의 제조 과정에서 용탕 내부에 세라믹 강화상이 자발적으로 형성되는 자발합성 공정의 설계 및 최적화와 관련된 연구가 최근 각광을 받고 있다. 이러한 자발합성을 통해 형성된 강화상은 용탕과의 젖음성이 우수하며 취성의 계면결합물을 형성하지 않아 응고 이후에도 강한 계면결합을 이루는 장점이 있다. 하지만 열역학적으로 안정한 강화상의 형성은 반응속도의 향상을 위해 높은 온도 조건에서 공정이 이루어져야 하며 긴 공정시간을 유지하는 것이 요구되므로 경제적인 측면에서 바람직하지 못하다는 단점이 있다. 따라서 세라믹 강화상의 자발적인 형성 조건을 최적화 하기 위한 자발합성 공정의 변수 제어 또는 새로운 자발합성 공정기술을 개발하기 위한 노력이 요구되고 있다.

본 연구에서는, 아크플라즈마를 이용하여 초고온으로 금속을 용해하는 기존 아크용해법으로 강화상의 자발합성을 위해 가스, 분말 또는 잉곳 형태의 원료 소재를 금속 기지에 혼합하여 용해함으로써 새로운 개념의 금속-세라믹

복합재료를 제조하는 신 공정기술의 개발 및 제조된 복합소재의 특성 분석에 대한 연구를 수행하였다. 아크용해를 통해 끓는점에 가까운 고온으로 용탕을 가열함으로써 세라믹 강화상의 합성반응을 일으키고, 촉진시키며, 강화상에 대한 용탕의 젖음성을 향상시킴에 따라 단시간 내에 제조된 복합소재가 용탕의 응고 이후에도 금속기지와 강화상 간에 강한 계면 결합을 갖게 되는 것으로 확인되었다. 본 연구에서는 아크용해를 통해 촉진된 자발합성 반응으로부터 새로운 금속-세라믹 복합재료의 개발 가능성과, 복합재료의 형성 메커니즘 및 실제 응용처로의 적용 가능성에 대해서 고찰하였다.

아르곤과 질소 기체로 이루어진 분위기 하에서 알루미늄을 아크용해한 결과 용탕의 질화가 매우 빠르게 촉진되어 단 시간 내에 알루미늄-질화알루미늄 복합재료를 제조할 수 있었다. 이러한 질화반응은 아크플라즈마에 의한 질소 기체의 분해, 알루미늄 용탕으로의 즉각적인 질소 기체의 고용 및 고용된 질소 원자의 빠른 확산과 더불어 질화알루미늄과 알루미늄 용탕간에 향상된 젖음성에 기인하는 것으로 밝혀졌다. 아크용해법을 통해 촉진된 알루미늄의 질화반응은 3분의 반응시간 동안 최대 40 vol.%의 질화알루미늄 형성을 야기하는데, 이러한 결과는 지금까지 알루미늄 용탕과 질소 기체의 자발합성 반응으로부터 제조된 알루미늄기 복합재료 중 가장 많은 질화알루미늄을 포함하는 것으로 확인되었다.

분말형태의 세라믹 소재와 접촉된 상태의 알루미늄을 아크용해법을 통해 용해한 결과, 아크플라즈마에 의해 이루어진 초고온의 용탕으로부터 용탕과 원료 분말간의 치환반응이 발생하고, 기존의 용해법을 이용한 반응에 대비했을 때 치환반응이 보다 촉진되는 현상을 확인하였다. 아크용해법으로 용해된 알루미늄 용탕은 질화규소 분말로 이루어진 응집체에 침투됨과 동시에 질화규소와 치환반응을 하게 되면서 열역학적으로 안정한 질화알루미늄이 형성하였고, 이를 통해 최종적으로 질화규소가 질화알루미늄으로 치환된 알루미늄-질화알루미늄 복합재료를 제조할 수 있었다. 질화알루미늄으로의 치환반응은 기지 내 강화상의

부피분율 증가를 유발하였는데, 이러한 결과는 향후 아크용해법을 통해 고분율의 질화세라믹을 갖는 복합재료를 제조하는 공정을 설계하는데 도움이 될 것으로 기대된다. 아크용해법을 이용한 용탕-세라믹 치환 반응은 순수 금속 기지뿐만 아니라 다성분계 합금, 특히 벌크 비정질 합금 기지에 대해서도 적용 가능한 것으로 확인되었다. 알루미늄-질화알루미늄 복합재료를 지르코늄기 비정질 모합금과 혼합하여 아크용해한 결과 질화알루미늄과 지르코늄의 치환반응으로부터 형성된 질화지르코늄 입자로 강화된 비정질기지 복합재료를 제조할 수 있었다. 이 입자 강화 비정질 기지 복합재료는 단일 비정질 합금과 대비하여 향상된 압축연신을 보였으며 이는 질화지르코늄 입자로 인한 다수의 전단 띠는 형성되고, 국부적인 영역에서의 단일 전단 띠 형성은 억제되기 때문인 것으로 밝혀졌다. 자발합성 공정을 통한 비정질 합금기지 복합재료의 제조는 비정질 합금의 단점으로 여겨지던 취성과괴 거동을 지연시켜 구조용 소재로서의 적용 가능성을 확장시키는 것으로 확인되었다.

본 연구에서 아크용해법을 통해 새롭게 제조된 금속-세라믹 복합재료는 열역학적으로 안정한 강화상의 자발적인 형성과 기지와의 강한 결합을 통해 우수한 기계적 특성 또는 열 특성을 나타내는 것으로 확인되었다. 이러한 결과는 아크플라즈마를 통해 촉진된 공정으로부터 기체와 액체, 또는 고체의 자발합성 반응을 유발함으로써 단시간 내에 우수한 특성의 금속-세라믹 복합재료를 제조할 수 있는 새로운 가능성을 제시하는 것으로 사료된다.

표제어: 복합재료, 아크 용해, 자발합성 공정, 질화 반응, 치환 반응

학 번: 2010-20624